UNIVERSIDADE FEDERAL DE MINAS GERAIS
SCHOOL OF ENGINEERING
POSTGRADUATE PROGRAM IN STRUCTURAL ENGINEERING

Lucas de Siqueira Paes Teixeira

COMPARATIVE STUDY OF STRATEGIES FOR CREEP SIMULATION IN THE CALCULATION OF SECOND-ORDER EFFECTS IN REINFORCED CONCRETE COLUMNS

Belo Horizonte/MG
2025

Lucas de Siqueira Paes Teixeira

COMPARATIVE STUDY OF STRATEGIES FOR CREEP SIMULATION IN THE CALCULATION OF SECOND-ORDER EFFECTS IN REINFORCED CONCRETE COLUMNS

Thesis submitted to the Postgraduate Program in Structural Engineering at the School of Engineering of the Universidade Federal de Minas Gerais (Federal University of Minas Gerais), in a partial fulfillment of the requirements for the degree of "Master in Structural Engineering".

Advisor: Prof. Dr. Leandro Lopes da Silva

Co-advisor: Prof. Dr. Juliano dos Santos Becho

Belo Horizonte/MG
2025

Teixeira, Lucas de Siqueira Paes.
T266c Comparative study of strategies for creep simulation in the calculation of second-order effects in reinforced concrete columns [recurso eletrônico] Lucas de Siqueira Paes Teixeira. - 2025.
1 recurso online (163 f. : il., color.) : pdf.

Orientador: Leandro Lopes da Silva.
Coorientador: Juliano dos Santos Becho.

Dissertação (mestrado) - Universidade Federal de Minas Gerais, Escola de Engenharia.

Inclui bibliografia.

1. Engenharia de estruturas - Teses. 2. Concreto armado - Teses 3. Colunas de concreto - Teses. 4. Método computacional - Teses. I. Silva, Leandro Lopes da. II. Becho, Juliano dos Santos. III. Universidade Federal de Minas Gerais. Escola de Engenharia. IV. Título.

CDU: 624(043)

Ficha catalográfica elaborada pelo bibliotecário Reginaldo César Vital dos Santos CRB/6 2165
Biblioteca Prof. Mário Werneck, Escola de Engenharia da UFMG

UNIVERSIDADE FEDERAL DE MINAS GERAIS

PROGRAMA DE PÓS-GRADUAÇÃO EM ENGENHARIA DE ESTRUTURAS

PROPEEs

UFMG

ATA DA DEFESA DE DISSERTAÇÃO DE MESTRADO EM ENGENHARIA DE ESTRUTURAS Nº: 413 DO ALUNO LUCAS DE SIQUEIRA PAES TEIXEIRA

Às **14:00** horas do dia **23** do mês de **maio** de **2025**, reuniu-se em ambiente híbrido, na Escola de Engenharia da Universidade Federal de Minas Gerais - UFMG, a Comissão Examinadora indicada pelo Colegiado do Programa em **25 de abril de 2025**, para julgar a defesa da Dissertação de Mestrado intitulada **"Estudo Comparativo de Diferentes Estratégias para Simulação da Fluência no Cálculo dos Efeitos de Segunda Ordem em Pilares de Concreto Armado"**, cuja aprovação é um dos requisitos para a obtenção do Grau de MESTRE EM ENGENHARIA DE ESTRUTURAS na área de ESTRUTURAS.

Abrindo a sessão, o Presidente da Comissão, **Prof. Dr. Leandro Lopes da Silva** , após dar a conhecer aos presentes o teor das Normas Regulamentares passou a palavra ao candidato para apresentação de seu trabalho. Seguiu-se a arguição pelos examinadores, com a respectiva defesa do candidato. Logo após, a Comissão se reuniu, sem a presença do candidato e do público, para julgamento e expedição do resultado final. Foram atribuídas as seguintes indicações:

(X) Aprovado
( ) Reprovado

O resultado final foi comunicado publicamente ao aluno pelo Presidente da Comissão.

Nada mais havendo a tratar, o Presidente encerrou a reunião e lavrou a presente ata, que será assinada por todos os membros participantes da Comissão Examinadora e pelo aluno.

Comissão Examinadora:

Prof. Dr. Leandro Lopes da Silva - DEES - UFMG (Orientador)
Prof. Dr. Juliano dos Santos Becho - DEES - UFMG
Prof. Dr. Marcelo Greco - DEES - UFMG
Prof. Dr. Roberto Caldas de Andrade Pinto - UFSC

A aprovação do aluno na Defesa da Dissertação de Mestrado não significa que o mesmo tenha cumprido todos os requisitos necessários para obtenção do DIPLOMA de Mestre em Engenharia de Estruturas.

Para ciência do aluno:

1. Atesto que as alterações solicitadas pela Comissão Examinadora serão cumpridas no prazo determinado pela banca de **ATÉ 60 dias** corridos.

2. Atesto estar ciente que a versão corrigida da dissertação deverá ser entregue ao Repositório Institucional

da UFMG, conforme orientações disponíveis em: https://repositorio.ufmg.br/custom/instructions.jsp

Ciente: **Lucas de Siqueira Paes Teixeira**
Aluno

Belo Horizonte, 23 de maio de 2025

Este documento não terá validade sem a assinatura do Coordenador do Programa de Pós-Graduação.
Após a Homologação da Defesa pelo Colegiado do Programa, este documento será assinado pela Coordenação e disponibilizado ao aluno.

Documento assinado eletronicamente por **Leandro Lopes da Silva**, **Professor do Magistério Superior**, em 23/05/2025, às 16:12, conforme horário oficial de Brasília, com fundamento no art. 5º do Decreto nº 10.543, de 13 de novembro de 2020.

Documento assinado eletronicamente por **Juliano dos Santos Becho**, **Professor do Magistério Superior**, em 23/05/2025, às 16:14, conforme horário oficial de Brasília, com fundamento no art. 5º do Decreto nº 10.543, de 13 de novembro de 2020.

Documento assinado eletronicamente por **Marcelo Greco**, **Professor do Magistério Superior**, em 23/05/2025, às 16:14, conforme horário oficial de Brasília, com fundamento no art. 5º do Decreto nº 10.543, de 13 de novembro de 2020.

Documento assinado eletronicamente por **Roberto Caldas de Andrade Pinto**, **Usuário Externo**, em 26/05/2025, às 08:45, conforme horário oficial de Brasília, com fundamento no art. 5º do Decreto nº 10.543, de 13 de novembro de 2020.

Documento assinado eletronicamente por **Felicio Bruzzi Barros**, **Subcoordenador(a)**, em 26/05/2025, às 10:18, conforme horário oficial de Brasília, com fundamento no art. 5º do Decreto nº 10.543, de 13 de novembro de 2020.

A autenticidade deste documento pode ser conferida no site https://sei.ufmg.br/sei/controlador_externo.php?acao=documento_conferir&id_orgao_acesso_externo=0, informando o código verificador **4213574** e o código CRC **26854E06**.

Referência: Processo nº 23072.230153/2025-06 SEI nº 4213574

ACKNOWLEDGMENTS

To my mother, for her unconditional love, affection, guidance, motivation, unwavering support, and for always believing in me.

To my girlfriend, for her care, encouragement, and for sharing these days with me.

To my advisor, Prof. Dr. Leandro Lopes da Silva, for his guidance, patience, availability, and invaluable insights. His expertise and encouragement were fundamental in shaping this research.

To my co-advisor, Prof. Dr. Juliano dos Santos Becho, for his patience and for providing the foundation for my understanding of the creep phenomenon.

To my therapist, Victor Polignano, for his guidance, balance, an invaluable support throughout this journey.

To my colleagues and friends in the Program, who shared this journey with me. To the DEES-Conectados group, for the moments of fun that made this path lighter.

To my friends outside the Program, whom I know I can always count on.

To the professors and staff of DEES and PROPEEs, for their excellence in academic and administrative services.

To the Fundação de Amparo à Pesquisa do Estado de Minas Gerais (FAPEMIG) for its financial support.

"And in the end, the love you take
is equal to the love you make."
(Lennon & McCartney)

RESUMO

TEIXEIRA, L. S. P. **Estudo comparativo de diferentes estratégias para simulação da fluência no cálculo dos efeitos de segunda ordem em pilares de concreto armado**. 2025. Dissertação (Mestrado). Programa de Pós-Graduação em Engenharia de Estruturas, Universidade Federal de Minas Gerais, Minas Gerais, 165 p., 2025.

Este estudo analisa diferentes estratégias para a simulação da fluência no cálculo dos efeitos de segunda ordem em pilares de concreto armado, visando comparar diferentes métodos computacionais e avaliar seu desempenho na previsão de momentos ao longo do tempo. Diversas abordagens foram avaliadas, desde metodologias simplificadas até mais avançadas. O *Método do Pilar-Padrão com Rigidez Aproximada e Excentricidade Adicional* mostrou-se aplicável para cálculos simplificados, embora conservador. O *Método do Pilar-Padrão acoplado a diagramas momento-normal-curvatura*, incorporando os efeitos da fluência via deslocamento da curva tensão-deformação, mostrou-se uma alternativa intermediária eficiente, mas apresentou inconsistências em casos específicos. O *Método Semi-Geral acoplado a diagramas momento-normal-curvatura*, apesar de utilizar a mesma consideração para a fluência, revelou-se ineficiente e inviável para aplicações de projeto, por combinar resultados excessivamente conservadores com maior custo computacional. O *Método Geral acoplado a diagramas momento-normal-curvatura*, considerando os efeitos da fluência via deslocamento da curva tensão-deformação, representou a não-linearidade física e geométrica com alta precisão, mas exigiu implementação computacional. Uma variação desse método, incorporando o modelo reológico de Kelvin-Voigt, apresentou resultados promissores, porém necessita de melhor calibração dos parâmetros. Por fim, o *Método Geral acoplado a diagramas momento-normal-curvatura*, baseado na nova proposição de diagrama tensão-deformação para análise não linear introduzida na NBR 6118 (2023), resultou em valores de momentos significativamente menores, exigindo investigação adicional. Os resultados confirmam que maiores índices de esbeltez levam a efeitos da fluência mais pronunciados, especialmente quando os momentos tracionam a mesma face. Além disso, foram identificadas discrepâncias entre a NBR 6118 (2023) e normas internacionais, destacando a necessidade de ajustes na norma brasileira. Pesquisas futuras devem aprimorar os modelos numéricos e validá-los por meio de ensaios experimentais para aumentar sua confiabilidade em aplicações práticas.

Palavras-chave: fluência; efeitos de segunda ordem; pilares de concreto armado; análise não-linear; métodos computacionais.

ABSTRACT

TEIXEIRA, L. S. P. **Comparative study of strategies for creep simulation of second-order effects in reinforced concrete columns**. 2025. Master's Thesis - Postgraduate Program in Structural Engineering, Federal University of Minas Gerais, Minas Gerais, 165 p., 2025.

This study analyzes different strategies for creep simulation in the calculation of second-order effects in reinforced concrete columns, aiming to compare computational methods and assess their performance in predicting long-term moments. Several approaches were evaluated, ranging from simplified to advanced methodologies. The *Standard Column Method with Approximate Stiffness and Additional Eccentricity* proved applicable for quick calculation, though conservative. The *Standard Column Method coupled with moment-axial force-curvature diagrams*, incorporating creep effects via the extended stress-strain curve, emerged as an efficient intermediate alternative, but showed inconsistencies in specific cases. The *Semi-General Method coupled with moment-axial force-curvature diagrams*, despite using the same creep consideration, proved inefficient and impractical for design applications, as it combines overly conservative results with higher computational cost. The *General Method coupled with moment-axial force-curvature diagrams*, considering creep effects through the extended stress-strain curve, fully accounted for physical and geometric nonlinearities with high precision but requires computational implementation. A variation of this method, incorporating the Kelvin-Voigt rheological model, showed promising results but requires further parameter calibration. Finally, the *General Method coupled with moment-axial force-curvature diagrams*, based on the new stress-strain diagram for nonlinear analysis introduced by NBR 6118 (2023), produced significantly lower moment values, requiring further investigation. The results confirm that higher slenderness ratios lead to more pronounced creep effects, particularly when moments induce tension on the same face. Additionally, discrepancies between NBR 6118 (2023) and updated international standards highlight the need for adjustments in the Brazilian code. Further research should refine numerical models and validate them against experimental results to enhance their reliability in practical applications.

Keywords: creep; second-order effects; reinforced concrete columns; nonlinear analysis; computational Methods.

LIST OF FIGURES

LIST OF TABLES

LIST OF SYMBOLS

Lowercase Latin Letters

a_{2u}	Distance from the most compressed edge of the section
b_w	Width of the concrete cross-section
d	Distance from the most compressed edge to the centroid of the most tensioned reinforcement layer
d'	Distance from the centroid of the reinforcement layer to the nearest edge
e_1	First-order eccentricity
e_2	Second-order eccentricity
e_a	Eccentricity due to local imperfections
f_{cd}	Design compressive strength of concrete
f_{ck}	Characteristic compressive strength of concrete
f_{cm}	Mean compressive strength of concrete
f_{yd}	Design yield strength of reinforcement
f_{yk}	Characteristic yield strength of reinforcement
h	Height of the column's cross-section
h_{fic}	Fictitious thickness
h/r	Dimensionless curvature
ℓ	Length between the axes of the structural elements to which the element is supported
ℓ_0	Length between the inner faces of the structural elements that provide support to the column
ℓ_e	Effective length of the column
n_{si}	Ratio between the area of a single reinforcement bar and the total reinforcement area
t	Fictitious age

t_0	Fictitious age at load application
u	Perimeter
x	Neutral axis depth
y	Distance of a generic fiber from the centroid of the section
y_0	Distance from the neutral axis to the centroid of the section
$1/r$	Curvature

Uppercase Latin Letters

A_c	Cross-sectional area
E	Modulus of elasticity
E_{ci}	Initial tangent modulus of elasticity of concrete
E_{cm}	Mean modulus of elasticity of concrete
E_{cs}	Secant modulus of elasticity of concrete
E_s	Modulus of elasticity of steel
I	Cross-sectional moment of inertia
M	Moment
$M_{1d,\min}$	Minimum moment
M_{cc}	Resulting bending moment in the compressed concrete section
M_d	First-order design moment
M_R	Resisting bending moment
M_{Sg}	First-order moment due to the quasi-permanent load combination
N	Axial force
N_d	Design axial force
N_R	Resisting axial force
N_e	Euler critical load
R_{cc}	Resulting axial force in the compressed concrete section
R_{si}	Resulting axial force in the reinforcement

T_i	Average daily ambient temperature
U	Ambient relative humidity
$(EI)_{\text{sec}}$	Secant stiffness

Greek Letters

α	Coefficient dependent on the hardening rate of the cement
α_b	Factor dependent on boundary conditions and the shape of the first-order moment diagram
α_E	Parameter dependent on the nature of the aggregate
$\beta_d(t)$	Coefficient related to reversible delayed strain as a function of time after loading
$\beta_f(t)$	Coefficient related to irreversible delayed strain as a function of concrete age
β_x	Dimensionless neutral axis depth
β_{xi}	Lower limit for the dimensionless neutral axis depth
β_{xs}	Upper limit for the dimensionless neutral axis depth
β_y	Dimensionless position of the generic fiber
γ_c	Partial safety factor for concrete strength
γ_s	Partial safety factor for reinforcing steel
γ_f	Partial safety factor for actions
γ_{f1}	Component of γ_f, accounting for the variability of actions
γ_{f2}	Component of γ_f, considering the simultaneity of action effects
γ_{f3}	Component of γ_f, accounting for deviations from construction processes and design approximations
κ	Dimensionless stiffness
λ	Slenderness ratio
λ_1	Limiting slenderness ratio
μ_R	Dimensionless resisting bending moment

ν	Dimensionless axial force
ν_R	Dimensionless resisting axial force
ω	Mechanical reinforcement ratio
σ_c	Compressive stress in concrete
σ_s	Stress in the passive reinforcement steel
ε_c	Compressive immediate strain in concrete
$\varepsilon_{c,total}$	Total strain in concrete, sum of immediate and creep strain
ε_{c1}	Compressive strain in concrete at peak stress
ε_{c2}	Specific compressive strain at the onset of the plastic plateau
ε_{cc}	Total creep strain
ε_{cca}	Component of creep strain related to rapid strain
ε_{ccf}	Component of creep strain related to irreversible delayed strain
ε_{ccd}	Component of creep strain related to reversible delayed strain
ε_{cu}	Ultimate compressive strain in concrete
ε_s	Strain in passive reinforcement steel
ε_{su}	Reinforcement steel strain at failure
ε_{KV}	Creep strain in the most compressed edge of concrete calculated by the Kelvin-Voigt rheological model
ε_{yd}	Design yield strain of reinforcement steel
ε_{2u}	Specific strain at a concrete fiber located at a distance a_{2u} from the most compressed edge of the section
φ	Creep coefficient
φ_a	Rapid creep coefficient
φ_f	Irreversible delayed creep coefficient
$\varphi_{f\infty}$	Final value of the irreversible delayed creep coefficient
φ_d	Reversible delayed creep coefficient

$\varphi_{d\infty}$	Final value of the reversible delayed creep coefficient
φ_{ef}	Effective creep coefficient
φ_{KV}	Creep coefficient calculated by the Kelvin-Voigt rheological model
φ_{1c}	Coefficient dependent on ambient relative humidity and concrete consistency
φ_{2c}	Coefficient dependent on the fictitious thickness of the element
η	Viscosity coefficient
η_c	Factor accounting for the brittleness of concrete
$\Delta t_{\mathrm{ef,i}}$	Period during which the average daily ambient temperature can be assumed constant

TABLE OF CONTENTS

1 INTRODUCTION

The design of reinforced concrete structures begins with integrating architectural considerations and structural conception. Following this, the conceived structure undergoes *Structural Analysis*, a critical phase involving the idealization of the structure's behavior. This process includes the evaluation of stresses, strains, and displacements within the structure, aiming to determine the internal forces and reactions, as well as the resulting deformations (MARTHA, 2017). Structural analysis serves as a foundation for designing safe and functional components that meet the demands of their intended use.

Traditionally, simplified calculations and manual methods employ *Linear Structural Analysis*, which assumes an undeformed configuration and linear material behavior governed by Hooke's Law. This approach neglects material degradation and real equilibrium effects in the deformed configuration. While practical for approximations, this linear approach does not capture the full complexity of structural behavior.

In contrast, *Nonlinear Structural Analysis* encompasses *Physical and Geometrical Nonlinearities*, enabling a more realistic representation of structural behavior. Historically, the computational effort for nonlinear analyses posed significant challenges. However, advances in computing power, structural modeling, and the widespread availability of engineering software have made such analyses increasingly feasible. Kimura (2018) observes that nearly all modern reinforced concrete building designs account for some form of nonlinearity through simplified or refined approaches.

Physical Nonlinearity refers to the non-linear material behavior of structural components. For reinforced concrete, material properties evolve under applied loads, leading to a nonlinear response. This behavior is primarily attributed to the heterogeneity and cracking of concrete. On the other hand, *Geometrical Nonlinearity* arises from deformations in the geometry of structural elements under load. This is particularly relevant in *Second-Order Analysis*, where the structure is analyzed in its deformed state, capturing the *Second-Order Effects*.

According to Kimura (2018), considering physical and geometrical nonlinearities significantly influences the calculation of displacements and internal forces in a structure. The NBR 6118 (2023) standard mandates the consideration of physical nonlinearity in reinforced concrete structures, both in global analysis and in the analysis of column-type elements. Analyzing elements such as reinforced concrete columns becomes particularly complex in this context. Due to their predominantly vertical structure, these components are susceptible to instability phenomena, which result in significant geometrical nonlinearity in addition to physical

nonlinearity (CASAGRANDE, 2016). The significance of considering these nonlinearities is magnified in modern structures characterized by increased heights. Moreover, time-dependent deformations such as *Shrinkage* and *Creep* become more pronounced.

Shrinkage is defined as the phenomenon of deformations in concrete caused by the loss of chemically unbound water during its production process. When water migrates out of a porous, non-rigid body, contraction occurs. In concrete, this type of water movement can be observed from its fresh state to more advanced ages (NEVILLE, 2016).

Creep, defined as the progressive deformation of concrete under sustained load, is influenced by environmental conditions, material properties, and structural dimensions (SOUZA, 2012). While creep imparts ductility to concrete, it also introduces challenges such as excessive deflections, stability issues, and stress redistribution, especially in tall columns (BALLIM; FANOURAKIS, 2003).

Despite the extensive literature on creep mechanics, practical methodologies for its incorporation in structural design remain underexplored. Simplified methods, such as the *Approximate Method of Additional Eccentricity (e_{cc})*, dominate practical applications due to their relative simplicity. More refined approaches include using an extended stress-strain curve or rheological models (e.g., Kelvin-Voigt). These approaches focus on incorporating creep effects into the design process.

In parallel, the calculation of second-order effects typically relies on simplified methodologies, such as the *Standard Column Method*, which identifies the most stressed section of the column and, through simplifications, establishes expressions for calculating second-order effects. Conversely, the *Semi-General Method* and *General Method* provide a more rigorous representation of geometrical and physical nonlinearities.

Nevertheless, combining methods for creep simulation with second-order analysis significantly increases computational complexity and modeling challenges, underscoring the need for more integrated and efficient design solutions.

This dissertation aims to conduct a comparative study of various strategies for simulating creep in the calculation of second-order effects in reinforced concrete columns. By examining methods ranging from simplified approaches to advanced mathematical models, this research seeks to address gaps in the current practice, providing insights into their applicability and limitations. The methodologies evaluated include:

- *Standard Column Method with Approximate Stiffness κ and Additional Eccentricity (e_{cc})*;
- *Standard Column Method coupled with M, N, $1/r$ diagrams*, considering creep effects

through the extended stress-strain curve;
- *Semi-General Method coupled with M, N,* $1/r$ *diagrams*, considering creep effects through the extended stress-strain curve;
- *General Method coupled with M, N,* $1/r$ *diagrams*, considering creep effects through the extended stress-strain curve;
- *General Method coupled with M, N,* $1/r$ *diagrams*, considering creep effects through the extended stress-strain curve based on the Kelvin-Voigt rheological model;
- *General Method coupled with M, N,* $1/r$ *diagrams*, based on the new stress-strain diagram for nonlinear analysis introduced in NBR 6118 (2023) and considering creep effects through the extended stress-strain curve.

1.1 JUSTIFICATION

The accurate design of reinforced concrete structures is a cornerstone of modern engineering, where safety, functionality, and cost-effectiveness are critical. Among the challenges in structural analysis, creep behavior in slender columns has attracted increasing attention due to its significant impact on structural performance over time. The time-dependent nature of creep alters internal force distributions and amplifies second-order effects, particularly in tall and slender columns where geometric and material nonlinearities are pronounced.

According to Casagrande (2016), and as confirmed by this study, the extensive literature on creep primarily addresses the fundamental mechanisms and their influence on concrete from a material perspective. However, studies on practical methodologies applicable to structural design remain scarce. This gap highlights the need for research that bridges the divide between theoretical studies and actionable design tools.

While many simplified approaches exist for structural analysis, they often fail to capture the complexities of creep behavior. Current design practices predominantly rely on methods such as the *Approximate Method of Additional Eccentricity* and *Standard Column Method*, which, despite their simplicity, involve assumptions that may limit their accuracy. Alternatively, more advanced approaches, like the *General Method*, or methods incorporating rheological models (e.g., Kelvin-Voigt), offer a more precise understanding but demand more significant computational resources and expertise.

A comprehensive comparative study of these methodologies is essential to address critical gaps in design practices:

1. The need to balance computational simplicity with the accuracy required for increasingly slender and complex structural elements.
2. The lack of guidelines for effectively integrating advanced creep simulation methods into

routine design.

3. The implications of inaccurately modeled creep behavior on the structure's safety, serviceability, and long-term performance.

The study's significance extends to both academic and professional domains. Academically, it advances the understanding of time-dependent behaviors in reinforced concrete columns, particularly the effects of creep. Professionally, it provides insights that could refine current codes of practice, such as the NBR 6118 (2023), and enhance the design of more efficient and sustainable structures.

Thus, this research contributes to bridging the gap between simplified and advanced design methodologies, fostering the development of practical solutions that align with the demands of modern structural engineering.

1.2 OBJECTIVES

This work conducts a comparative study of strategies for simulating creep in the calculation of second-order effects in reinforced concrete columns, aiming to compare computational methods and assess their accuracy in predicting long-term moments.

To support and achieve the proposed general objective, the following specific objectives will be pursued:

- Conduct a review of normative strategies and those described in the literature for simulating creep in reinforced concrete columns;
- Develop algorithms for implementing the different methods identified for simulating creep in the calculation of second-order effects in reinforced concrete columns;
- Propose models and simulations to serve as subjects of study;
- Establish metrics and compare results obtained through the different methods and structural models evaluated;
- Assess the applicability of simplified parameters proposed in standards and literature, discussing their limitations and their impact on creep simulation;
- If necessary, propose practical solutions to achieve more reliable results in the creep analysis in reinforced concrete columns.

1.3 DISSERTATION STRUCTURE

Chapter 2 explores the various types of deformation that affect concrete, their classification, and their significance in structural performance. Additionally, it defines the creep behavior, its causes, and its effects. Chapter 3 examines the verification and design of reinforced concrete

columns, focusing on the calculation of second-order effects. It presents the stress-strain diagrams of materials and the methods used to compute second-order effects. Chapter 4 discusses different strategies for creep simulation found in the literature. Chapter 5 describes the methodology, detailing the numerical formulation and implementations performed. Chapter 6 presents the results of the numerical examples analyzed and compares the outcomes obtained. Finally, Chapter 7 provides the conclusions and suggestions for future research.

2 CONCRETE DEFORMATIONS

Every stress applied to a material results in a corresponding deformation, although deformations may occur even without external stresses due to environmental conditions. Deformations, whether immediate or time-dependent, play a critical role in the performance and durability of concrete structures.

Like many other structural materials, concrete exhibits elastic behavior under certain conditions. A material is considered perfectly elastic when the strain occurs and disappears immediately with the application and removal of stress. However, perfect elasticity does not necessarily imply a linear stress-strain relationship (NEVILLE, 2016). For concrete, this relationship is typically nonlinear, especially under high-stress levels.

When subjected to sustained loads, concrete undergoes creep, in which strains increase gradually over time. Furthermore, regardless of external forces, concrete experiences shrinkage, a volumetric contraction caused by drying, or other chemical factors. According to Neville (2016), the magnitudes of shrinkage and creep are often comparable to the elastic strains observed under typical stress levels. Therefore, all these types of deformations must be considered in structural analysis to ensure accurate and reliable design.

This chapter explores the various types of deformations affecting concrete, their classification, and their significance in structural performance. Additionally, it defines shrinkage and the creep behavior, its causes, and its effects.

2.1 TYPES OF DEFORMATIONS

Like any material, concrete exhibits three fundamental deformation types under applied loads: elastic, viscous, and plastic. These deformation types can occur independently or in combinations, such as elastoplastic or viscoelastic behavior, and the combinations can be complicated further by factors such as aging, thixotropy, or strain hardening (NEVILLE; DILGER; BROOKS, 1983).

Elastic deformation represents an immediate and reversible response, which vanishes upon unloading. For a linear elastic behavior, the stress-strain relationship is described by Hooke's Law

$$\sigma = E\varepsilon. \tag{2.1}$$

Viscous deformation, characteristic of ideal fluids, is defined by a strain rate directly proportional to the applied stress. This deformation is irreversible and evolves over time (NEVILLE; DILGER; BROOKS, 1983).

Plastic deformation results from permanent changes in the internal structure of a solid material. Unlike elastic deformation, it does not reverse upon unloading, and no proportionality exists between the applied stress and the resulting strain or strain rate (NEVILLE; DILGER; BROOKS, 1983).

Another type of deformation described in the literature is *delayed elasticity*. In this case, the deformation develops at a decreasing rate and is entirely reversible because the energy responsible for this behavior is stored within the material (NEVILLE; DILGER; BROOKS, 1983).

Regarding the behavior of concrete subjected to sustained loads within the typical range of working stresses, Hansen (1958 apud NEVILLE; DILGER; BROOKS, 1983, p. 14) categorizes concrete deformations as shown in Table 2.1.

Table 2.1 – Types of Deformation.

Deformation	**Instantaneous**	**Time-dependent**
Recoverable	Elastic	Delayed elastic
Irrecoverable	Plastic	Viscous

Adapted from Neville, Dilger and Brooks (1983).

In this context, creep is a time-dependent and partially reversible phenomenon, often described as a combination of elastic and viscous deformation (a more detailed discussion on this topic can be found in Section 2.3).

In addition to deformations resulting from external loads, concrete undergoes drying-induced contraction, which leads to shrinkage. Thus, the deformations in concrete can be categorized as shrinkage, thermal deformation, instantaneous deformation, and creep.

2.2 SHRINKAGE

Shrinkage is defined as the phenomenon of concrete deformation caused by the loss of chemically unbound water during its production process. Contraction occurs when water moves out of a porous body that is not entirely rigid. In concrete, this water movement is observed from the fresh state to advanced ages (NEVILLE, 2016).

Plastic shrinkage occurs when water evaporates from the surface of concrete while still in a plastic state. The intensity of plastic shrinkage depends on the amount of water lost, which, in

turn, is influenced by factors such as temperature, ambient relative humidity, and wind speed (NEVILLE, 2016).

Autogenous shrinkage, on the other hand, takes place after the setting process. This type of shrinkage results from water being withdrawn from the capillary pores due to the hydration of unhydrated cement within the concrete. This internal contraction of the cementitious system occurs within the concrete mass. According to Neville (2016), the contraction of the cement paste is restrained by the rigid skeleton of already-hydrated cement paste and by aggregate particles, resulting in shrinkage of a considerably smaller magnitude. Thus, as noted by the author, there is no need to differentiate it from drying shrinkage in concrete.

Drying shrinkage occurs when water exits concrete exposed to unsaturated air. A portion of this water loss is irreversible and must be distinguished from the reversible movement of water caused by alternating exposure to dry and wet environments. The volume change in concrete during drying is not equivalent to the volume of water removed. The loss of free water occurs initially and causes little to no shrinkage. As drying continues, adsorbed water is removed, and the volume change in the unrestricted hydrated cement paste is approximately equal to removing a single molecular layer of water from the surface of all gel particles (NEVILLE, 2016). This type of shrinkage is one of the primary causes of cracking, which can significantly impact the durability of concrete (KALINTZIS, 2000 apud KATAOKA, 2010, p. 28).

Factors influencing shrinkage include the water-cement ratio and the content and properties of the aggregate. Regarding the shrinkage of hydrated cement paste, it increases with a higher water-cement ratio. This happens because a higher ratio results in more evaporable water in the paste and facilitates faster water migration toward the element's surface. However, the most significant influence comes from the aggregate, which restrains the extent of shrinkage that can occur (NEVILLE, 2016). Additionally, chemical admixtures can increase or decrease shrinkage, depending on their specific properties.

2.3 CREEP

Creep is defined as the phenomenon of increasing deformations in concrete over time when subjected to and induced by constant sustained stress.

In its most general form, the strain-time curve for a material undergoing creep follows the pattern illustrated in Figure 2.1. This diagram was initially proposed by Thurston (1895 apud BECHO, 2020, p. 13).

At time zero, the strain is predominantly elastic, although it may include a non-elastic component. Subsequently, creep progresses through three distinct stages. During the *primary creep*

Figure 2.1 – General form of the strain-time curve for a material subjected to creep.

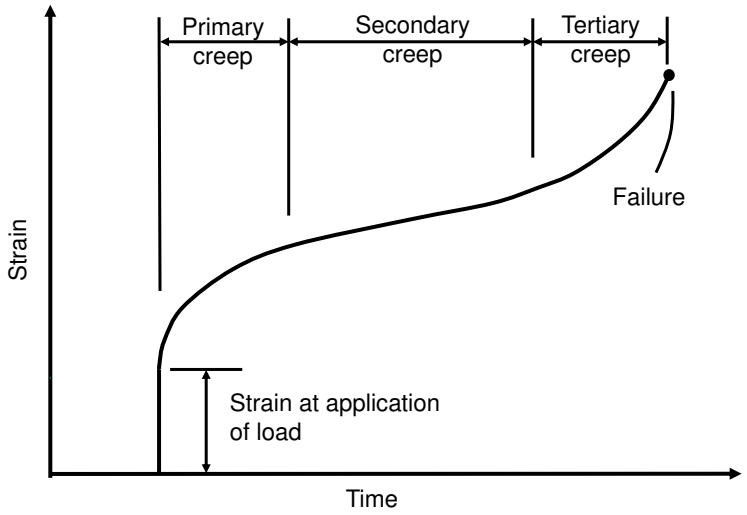

Adapted from Neville, Dilger and Brooks (1983).

stage, the creep rate decreases over time. For materials with a minimum creep rate, the *secondary creep stage* corresponds to the steady-state creep, characterized by a constant creep rate (NEVILLE; DILGER; BROOKS, 1983). The *tertiary creep stage* – which may or may not occur depending on the type of material, the level of applied stress, and the temperature – is defined by a progressively increasing creep rate (BECHO, 2020).

Under normal stress levels typical of concrete structures, primary creep cannot be distinguished from secondary creep, and tertiary creep does not occur (NEVILLE; DILGER; BROOKS, 1983). The strain-time curve for concrete under these conditions is depicted in Figure 2.2.

The curve shown in Figure 2.3 represents the creep behavior of a concrete element under sustained loading in conditions of 100% relative humidity. Under these conditions, there is no moisture exchange with the ambient (hygral equilibrium), and creep is referred to as *basic creep* (NEVILLE; DILGER; BROOKS, 1983).

Similar to shrinkage, creep is influenced by water loss from the concrete; however, in this case, the movement of water is induced by the applied constant stress. When an element loses moisture while under load, creep and shrinkage are assumed to act simultaneously. In this context, creep is determined as the difference between the total time-dependent strain and the shrinkage of a similar unloaded element maintained under the same environmental conditions over the same period. It is important to note that creep and shrinkage are not independent phenomena; therefore, the superposition principle cannot be applied. Creep resulting from the

Figure 2.2 – General form of the strain-time curve for concrete subjected to normal levels of sustained stress.

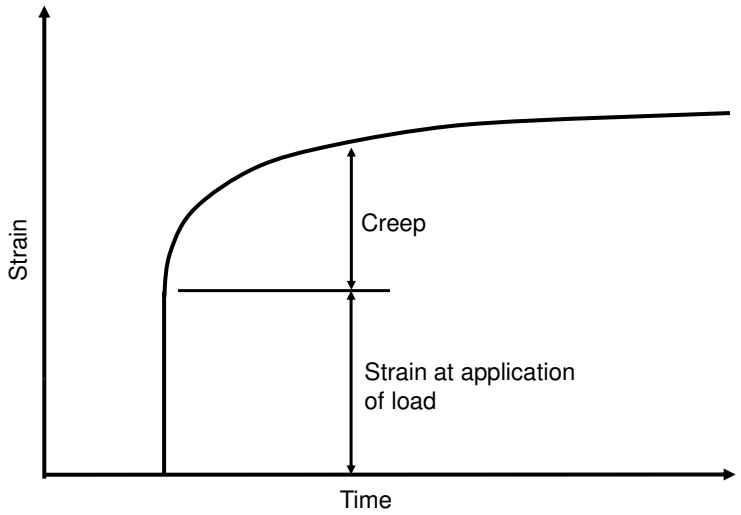

Adapted from Neville, Dilger and Brooks (1983).

Figure 2.3 – Creep behavior of a concrete element loaded under hygroscopic equilibrium with the environment.

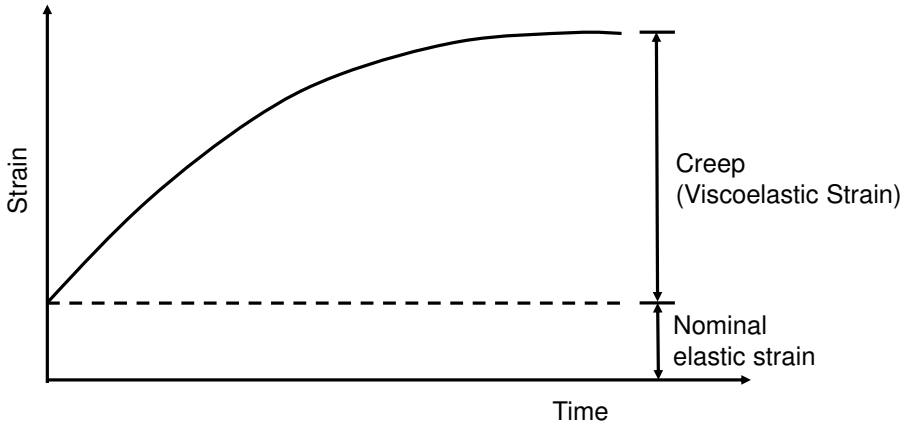

Adapted from Oliveira (2011).

exposure of concrete structures to drying is referred to as *drying creep* (OLIVEIRA, 2011). Figure 2.4 graphically illustrates the different types of strain discussed.

When the sustained load is removed, the strain decreases immediately by an amount equal to the elastic deformation at the same age, typically smaller than the elastic strain experienced during loading. This *instantaneous recovery* is followed by a gradual reduction in strain, known as *creep recovery*, as illustrated in Figure 2.5. It is important to note that creep recovery is incomplete, and creep is not a fully reversible phenomenon. As a result, any period of sustained

Figure 2.4 – Deformation of a loaded concrete element exposed to drying.

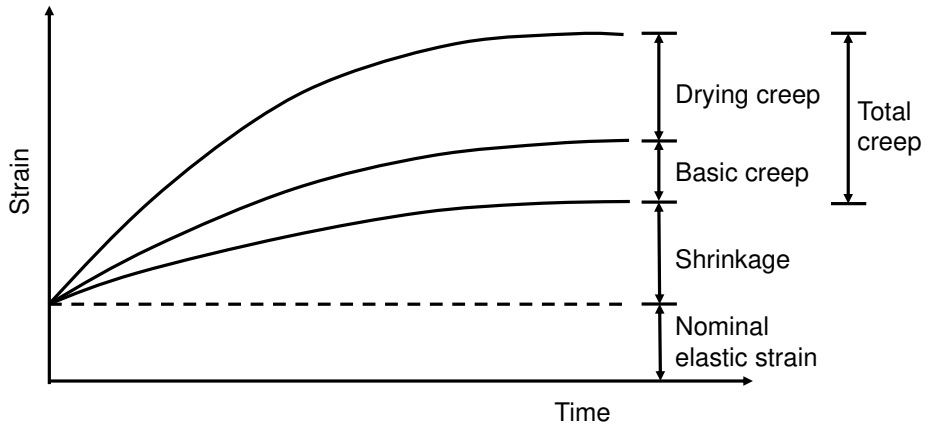

Adapted from Oliveira (2011).

load, even as short as a single day, leads to a residual strain (NEVILLE, 2016).

Figure 2.5 – Instantaneous and creep recovery.

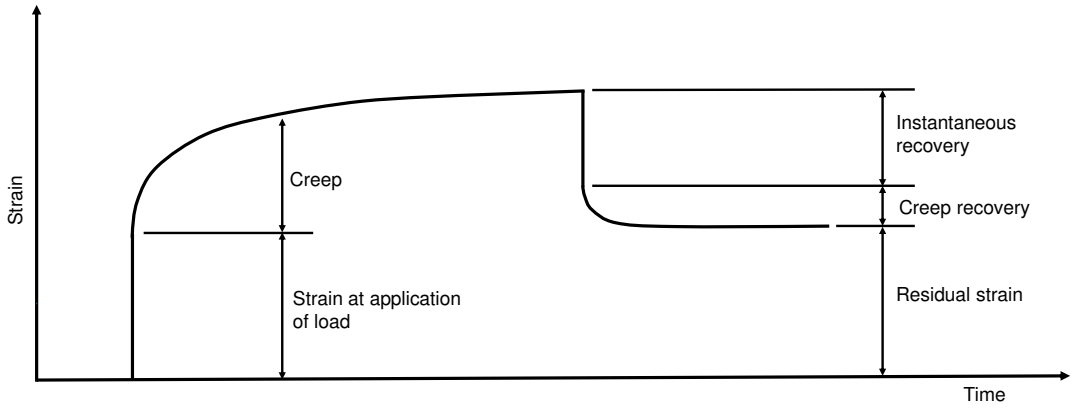

Adapted from Neville, Dilger and Brooks (1983).

Analyzing the curve in Figure 2.5, creep consists of a partially reversible viscoelastic deformation and an irreversible plastic deformation (NEVILLE, 2016).

In viscoelastic behavior, the solid material exhibits an immediate elastic response under load and an additional time-dependent elastic response, which is slow and damped (with a decreasing creep rate) (BECHO, 2020).

Viscoelastic behavior can be either linear or nonlinear with respect to stress. In linear behavior, the material's response depends only on time (BECHO, 2020). For concrete, however, the response depends on both time and the stress level, which is classified as nonlinear behavior.

2.3.1 Mechanisms of Creep

According to Neville (2016), the mechanisms underlying creep in concrete remain controversial and uncertain. The author states that creep occurs in the hydrated cement paste and is associated with the internal movement of adsorbed or intercrystalline water, referred to as internal percolation. However, variations in creep behavior at high temperatures suggest that, under such conditions, water ceases to influence the process, and the gel itself becomes subject to creep deformation.

Neville (2016) further explains that because creep occurs in mass concrete, external percolation of water is not essential for the progression of basic creep, although it may play a role in drying creep. Internal water percolation from adsorbed layers to voids within the material is still possible. Even under immersion in water, capillary voids remain unfilled due to hydrostatic pressure, allowing internal percolation to occur under various storage conditions. An indirect indication of the role of these voids is the relationship between creep and the strength of the hydrated cement paste. This suggests that creep may be a function of the relative amount of voids, particularly gel pores, which appear to control strength and creep. In this case, voids might be connected to the internal percolation process. The water-cement ratio and the degree of hydration inherently influence the volume of voids (NEVILLE, 2016).

The strain-time curve reveals a decreasing slope over time, indicating a potential change in the creep mechanism. Neville (2016) hypothesizes that after several years under sustained load, the thickness of adsorbed water layers may become so reduced that no further reduction occurs under the same stress level. Nevertheless, creep has been observed to persist even after 30 years. This long-term behavior suggests that the slow component of creep may arise from causes other than percolation. However, deformation requires evaporable water, pointing to mechanisms such as viscous flow or slippage between gel particles. These mechanisms are consistent with the temperature dependence of creep and also explain its largely irreversible nature.

Rüsch (1981 apud KATAOKA, 2010, p. 29) supports the idea that creep in concrete should be attributed to water migration induced by external loads. This includes the movement of adsorbed water within the gel structure and the effect of capillary stresses. Under load, the stress is distributed through both the solid skeleton and the water present in pores.

In addition, Mehta and Monteiro (2008) state that, although other factors also contribute to creep in concrete, the loss of physically adsorbed water under sustained pressure appears to be the most significant cause, highlighting the critical role of water in the creep process.

Neville (2016) also states that, in general, the role of microcracking in creep is minimal and is likely limited to concrete loaded at very early ages or under high stress-strength ratios

exceeding 0.6. Conversely, Mehta and Monteiro (2008) emphasize that the nonlinear stress-strain relationship in concrete, particularly under stress levels exceeding 30 to 40% of its ultimate stress, demonstrates the influence of microcracks in the interfacial transition zone between the aggregate and the cement paste to the creep phenomenon. Additionally, they highlight that the increased creep deformation observed when concrete is simultaneously exposed to drying conditions is caused by additional microcracking in the interfacial transition zone due to drying shrinkage.

Finally, Mehta and Monteiro (2008) also discuss the role of delayed elastic response in creep. According to the authors, since the cement paste and aggregate are bonded, the stress in the cement paste gradually decreases as the load is progressively transferred to the aggregate. With this transfer load, the aggregate undergoes elastic deformation, further contributing to the overall creep behavior. However, according to Neville (2016), the role of aggregates is primarily to restrict deformation, while the hydrated cement paste undergoes creep.

2.3.2 Factors Influencing Creep

In practice, creep in concrete is influenced by various factors that interact simultaneously. According to Mehta and Monteiro (2008), the interrelationships among these factors are highly complex and not easily understood. However, specific influences are more evident and will be discussed individually in the following sections.

2.3.2.1 Influence of Aggregates

Neville (2016) emphasizes that the role of aggregates in concrete is primarily to restrict deformation, as common aggregates do not undergo creep under the stresses present in concrete. Thus, creep is a function of the volumetric content of cement paste in the concrete, although this relationship is not linear. Figure 2.6 illustrates the relationship between concrete creep and aggregate content, where g represents the volumetric aggregate content and c denotes the creep of concrete.

The grading, maximum size, and shape of aggregate have been identified as factors influencing creep. However, their primary influence lies in their direct or indirect effect on the aggregate content (NEVILLE, 1964 apud NEVILLE, 2016, p. 471).

Specific physical properties of aggregates also impact concrete creep, with the modulus of elasticity playing a particularly significant role. Higher modulus provides greater restraint to the potential creep of the hydrated cement paste. Aggregate porosity also influences creep, possibly because highly porous aggregates typically have a lower modulus of elasticity or because porosity directly affects moisture movement within the concrete (NEVILLE, 2016).

Figure 2.6 – Relation between creep c after 28 days under load and aggregate content g for wet-stored specimens loaded at the age of 14 days to a stress-strength ratio of 0.50.

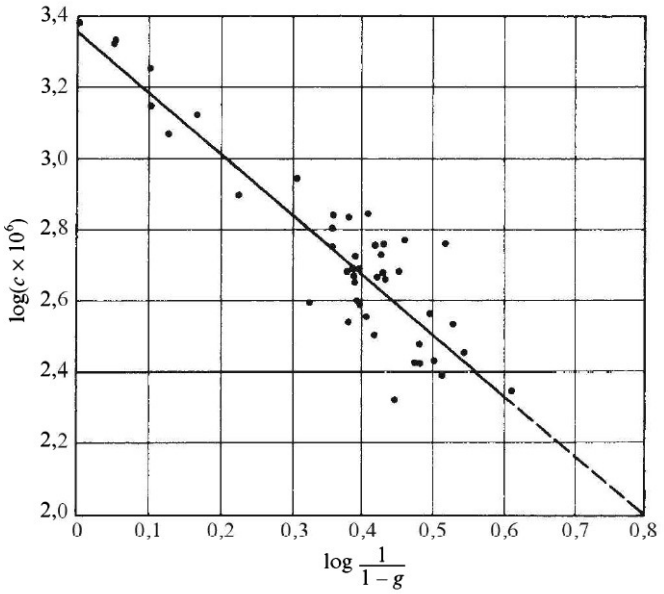

Source: Neville (1964 apud NEVILLE, 2016, p. 471).

The graph in Figure 2.7 shows the influence of different aggregate types on creep magnitude. After 20 years of storage at 50% relative humidity, concrete made with sandstone exhibited creep twice as high as that of concrete made with limestone.

Figure 2.7 – Creep of concretes of fixer proportions but made with different aggregates, loaded at the age of 28 days, and stored in air at 21 °C and relative humidity of 50%.

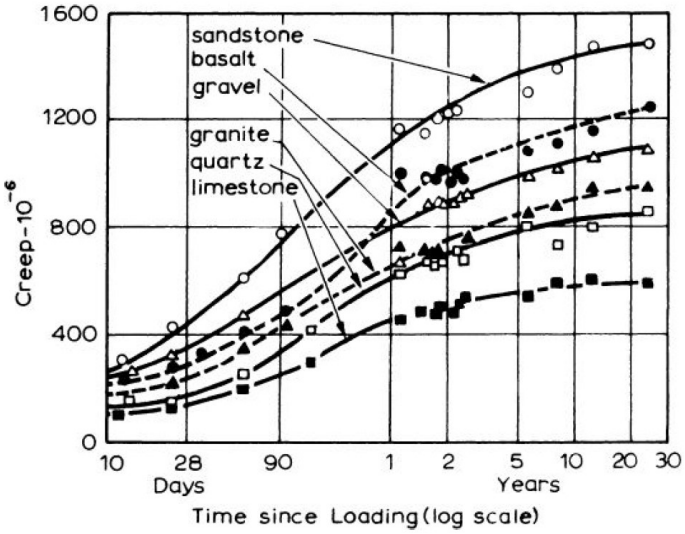

Source: Troxell, Raphael and Davis (1958 apud NEVILLE, 2011).

An even more significant variation in deformation was reported by Rüsch, Kordina and Hilsdorf

(1963 apud NEVILLE, 2016, p.473). After 18 months under sustained loading at 65% relative humidity, the maximum creep was five times greater than the minimum value. The aggregates, ranked in ascending order of creep, were basalt; quartz; gravel, marble and granite; and sandstone.

According to Neville (2016), there is no fundamental difference in creep behavior between normal-weight and lightweight aggregates. The higher creep observed in concretes made with lightweight aggregates is primarily due to these aggregates' lower modulus of elasticity. Generally, structural quality lightweight aggregate concrete's creep is comparable to concrete made with conventional aggregates. Furthermore, since lightweight aggregate concrete typically exhibits more elastic deformation than regular concrete, the ratio of creep to elastic deformation is smaller (NEVILLE, 1970 apud NEVILLE, 2016, p. 473).

2.3.2.2 Influence of Stress and Strength

As discussed by Neville (1960 apud NEVILLE, 2016, p. 473), creep is directly proportional to the applied stress within the range of stresses typically encountered in service structures. This proportionality is assumed in most creep models. Similarly, creep recovery is also proportional to the applied stress (YUE; TAERWE, 1992 apud NEVILLE, 2016, p. 473).

Concrete strength plays a significant role in influencing creep behavior. Within a broad range, creep is inversely proportional to the strength of the concrete at the time of the application of the load (NEVILLE, 1959a apud NEVILLE, 2016, p. 473). As illustrated in Figure 2.8, creep can be expressed as a linear function of the stress-strength ratio. In the analysis of Neville (2016), while acknowledging the importance of the water-cement ratio, the author emphasizes that for the same stress-strength ratio, creep is mainly independent of the water-cement ratio. Additionally, he disregards age as an isolated factor, highlighting instead its impact on increasing the strength of concrete over time.

2.3.2.3 Influence of Properties of Cement

According to Neville (2016), the type of cement influences creep primarily by affecting the strength of concrete when the load is applied. Therefore, any comparison of creep in concrete produced with different types of cement must account for how the cement type impacts the concrete's strength at the moment of loading. Based on this principle, concretes made with various types of Portland cement or high-alumina cement exhibit similar creep behavior (NEVILLE; KENINGTON, 1960 apud NEVILLE, 2016, p.475 and NEVILLE, 1958 apud NEVILLE, 2016, p.475), although the rate of strength development plays a role, as described below.

The fineness of cement influences early-age strength development and, consequently, impacts

Figure 2.8 – Creep of mortar specimens cured and stored continuously at different humidities.

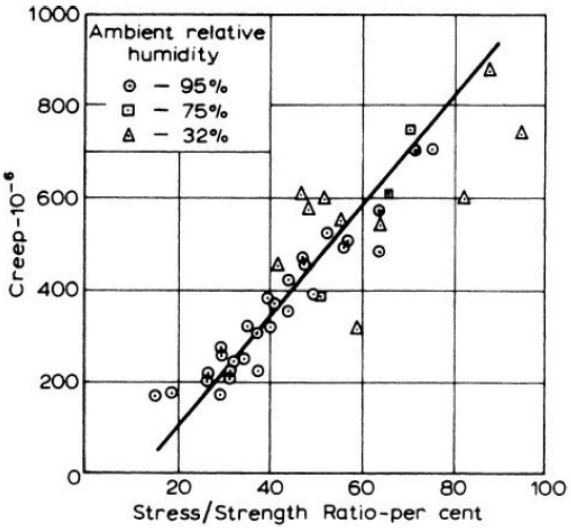

Source: Neville (1959b apud NEVILLE, 2011).

creep. However, fineness itself does not appear to be a direct factor in creep (NEVILLE, 2016).

The change in concrete strength under sustained load is crucial to evaluating the statement that the type of cement does not significantly influence creep. For the same stress-strength ratio at the time of loading, creep is smaller when there is a more significant relative increase in strength after the load is applied (NEVILLE; STAUNTON; BONN, 1966 apud NEVILLE, 2016, p. 475). According to the authors, for constant applied stress at an early loading age, creep increases in the following order: rapid-hardening cement, ordinary Portland cement, and low-heat cement.

Similarly, Mehta and Monteiro (2008), argue that when a specific aggregate and mix design are used, the type of cement can influence concrete strength at the moment of loading, affecting creep. They note that when concrete is loaded at early ages, mixes made with ordinary Portland cement typically show higher creep than those containing high-early-strength cement.

It is important to emphasize that the rate of strength gain significantly affects creep. Different cementitious materials, with varying hydration rates and strength development characteristics while the concrete is under load, produce distinct impacts on creep behavior (NEVILLE, 2016).

Finally, concrete made with expansive cement exhibits more creep than that produced with Portland cement alone (RUSSELL, 1978 apud NEVILLE, 2016, p. 476).

2.3.2.4 Influence of Ambient Relative Humidity

As noted by Neville (2016), the relative humidity of the air is among the most significant external factors affecting creep. Generally, lower relative humidity results in higher creep for a given concrete. This relationship is illustrated in Figure 2.9, which shows the impact of relative humidity on creep for specimens cured at 100% and subsequently exposed to different conditions. Under these conditions, significant variations in shrinkage are observed among the specimens during the early stages following the application of sustained loads. The corresponding creep rates also differ during this period but tend to converge at later ages.

Figure 2.9 – Creep of concrete cured in fog for 28 days, then loaded and stored at different relative humidities.

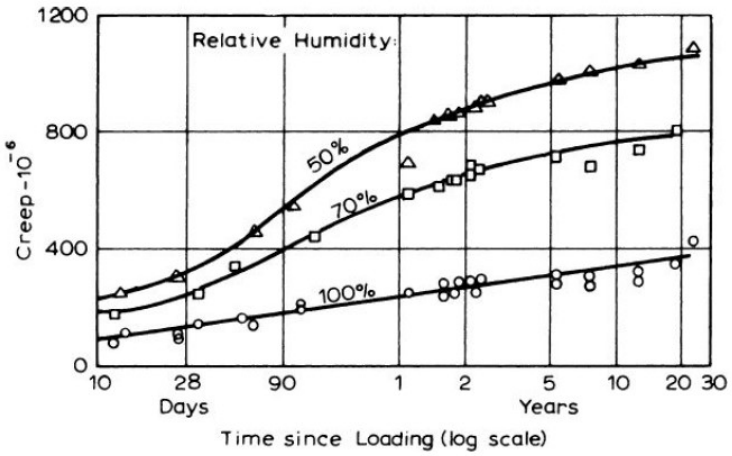

Source: Troxell, Raphael and Davis (1958 apud NEVILLE, 2011).

Drying under load enhances the creep of concrete, resulting in what is referred to as additional drying creep. The effect of relative humidity is significantly reduced or absent in specimens before being subjected to loading (NEVILLE, 1959b apud NEVILLE, 2016, p. 478). Therefore, it is not the relative humidity itself that directly influences creep but rather the drying process, which leads to drying creep.

It is also worth noting that concretes with higher shrinkage tend to exhibit higher creep (L'HERMITE, 1960 apud NEVILLE, 2016, p. 478). This correlation does not imply that the two phenomena share the exact cause but rather that they may be linked to similar characteristics of the hydrated cement paste structure.

2.3.2.5 Influence of the Geometry of the Concrete Element

According to Mehta and Monteiro (2008), the resistance to water transport from the interior of the concrete to the atmosphere controls the rate of water loss, as the distance traveled by the expelled water during creep plays a critical role. Similarly, Neville (2016) states that

creep decreases as the size of the concrete element increases since drying conditions are more pronounced at the surface than within the element's interior.

To simplify the representation of size and shape parameters, it is helpful to define a single quantity expressed as the *fictitious thickness* h_{fic}, which is calculated as the cross-sectional area divided by half the perimeter exposed to the atmosphere

$$h_{\text{fic}} = 2A_c/u. \tag{2.2}$$

In general, creep is reduced as the fictitious thickness increases. This relationship is evident from the curves shown in Figure 2.10, where it can also be observed that the shape of the element has a relatively minor influence on creep behavior.

Figure 2.10 – Relation between ratio of creep to elastic strain and volume-surface ratio.

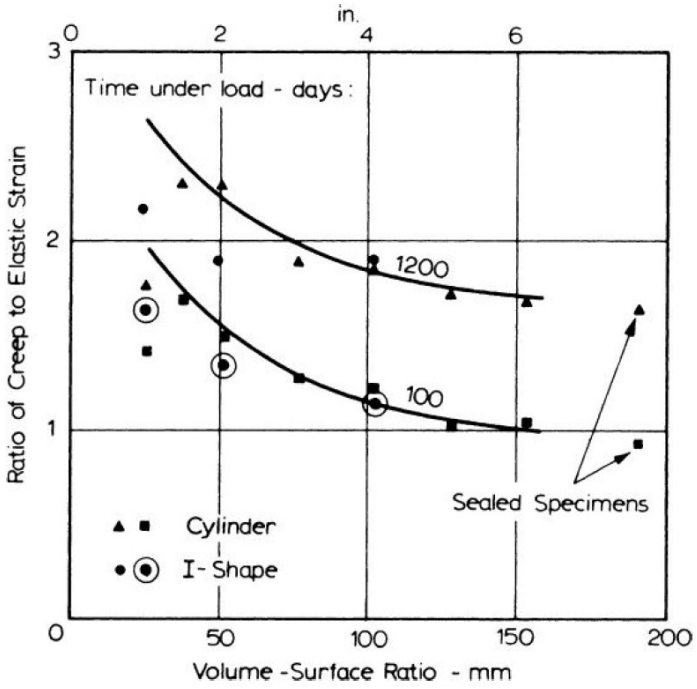

Source: Hansen and Mattock (1966 apud NEVILLE, 2011).

2.3.2.6 Other Influences

According to Mehta and Monteiro (2008), the *curing conditions* of a concrete element can significantly impact creep deformations, making them considerably different in practice compared to laboratory tests conducted under constant humidity. Drying cycles can intensify microcracking in the interfacial transition zone between the aggregate and the cement paste, thereby increasing creep. For the same reason, it is often observed that fluctuations in ambient

humidity between two limits result in more creep than under constant humidity within the same range.

Mehta and Monteiro (2008) also point out that *temperature* can have two contrasting effects on creep. Suppose a concrete element is exposed to elevated temperatures as part of the curing process before loading. In that case, its strength will increase, reducing creep deformations compared to similar concrete stored at lower temperatures. Conversely, exposure to high temperatures during the loading period can increase creep.

2.3.3 Effects of Creep

Creep influences strains, displacements, and stress distribution, but these effects vary depending on the structure being analyzed (NEVILLE, 1957 apud NEVILLE, 2016, p. 492).

Creep in plain concrete does not inherently impact its strength. However, under extremely high-stress levels, creep can accelerate the attainment of the ultimate strain that leads to failure. This phenomenon occurs only when the sustained load exceeds 85 to 90% of the static ultimate load applied rapidly (NEVILLE, 1959a apud NEVILLE, 2016, p. 492).

According to Ballim and Fanourakis (2003), creep in concrete exhibits both advantageous and disadvantageous aspects. It is beneficial because it imparts some ductility to the material and relieves stress from shrinkage-induced strain, thermal variations, or foundation movements. In all concrete structures, creep alleviates internal stresses caused by non-uniform shrinkage, which helps to minimize cracking (NEVILLE, 2016).

On the other hand, creep often leads to excessive deflections in service conditions, potentially resulting in structural instability, cracking, significant loss of straightness in tall columns, and loss of prestress (BALLIM; FANOURAKIS, 2003).

In reinforced concrete columns, creep causes a load transfer from the concrete to the reinforcement, which can lead to the yielding of the reinforcement even under low stress levels. In eccentrically loaded columns, creep increases displacements, potentially leading to the ultimate limit state of instability. Furthermore, creep and shrinkage can cause differential shortening between columns (CARREIRA; BURG, 2000 apud OLIVEIRA, 2011, p. 30).

3 VERIFICATION AND DESIGN OF COLUMNS

According to NBR 6118 (2023), *Columns* are linear structural elements with a straight axis, typically oriented vertically, where compressive axial forces predominate. These elements play a crucial structural role as they transfer loads from beams and slabs to the foundations. Consequently, columns are generally subjected to combined axial forces (compression) and bending moments. Bending is classified as uniaxial when the moment acts along a single principal axis of the cross-section or biaxial if the moment has components along both principal axes. As stated by Casagrande (2016), the design of columns is a complex task due to their susceptibility to instability, cumulative second-order effects, and creep.

This chapter explores the verification and design of reinforced concrete columns, focusing on calculating second-order effects. It begins by presenting the stress-strain diagrams of concrete and steel, which provide the foundation for understanding the nonlinear behavior of these columns. Following this, the concept of second-order effects is introduced, and the slenderness ratio and the limiting slenderness ratio are discussed, as well as how these parameters are used to classify columns. Finally, the methods for calculating second-order effects are detailed, from simplified to advanced approaches.

3.1 MECHANICAL PROPERTIES OF REINFORCED CONCRETE

Understanding the mechanical properties of the materials is essential for analyzing and designing reinforced concrete structures. These properties describe the material's behavior under various loading conditions and are critical for predicting the performance of structural elements. This session focuses on the stress-strain relationships of concrete and steel, laying the groundwork for understanding material behavior under applied loads and supporting subsequent analyses and design methodologies.

3.1.1 Stress-Strain Diagram of Concrete

The stress-strain diagram of concrete illustrates its behavior under loading. In this work, the diagram for compression is emphasized, as the tensile contribution of concrete is typically neglected. This analysis focuses on the material's immediate response to applied loads, excluding time-dependent effects such as creep and shrinkage. The stress-strain relationship of concrete is nonlinear and varies with the material's strength class.

The idealized stress-strain diagram illustrated in Figure 3.1 can be used for analyses in the ultimate limit state.

Figure 3.1 – Idealized Stress-Strain Diagram.

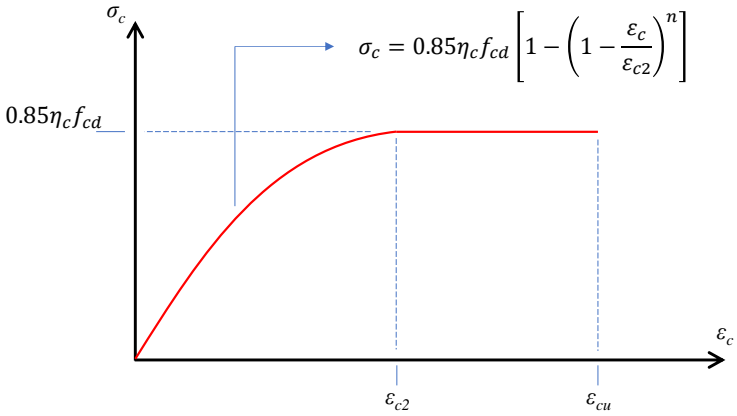

Adapted from NBR 6118 (2023).

Therefore, according to the figure, the following expression describes the stress-strain relationship

$$\begin{aligned} \sigma_c &= 0.85\eta_c f_{cd}\left[1-\left(1-\frac{\varepsilon_c}{\varepsilon_{c2}}\right)^n\right] \quad \text{for} \quad 0 \le \varepsilon_c \le \varepsilon_{c2}, \\ \sigma_c &= 0.85\eta_c f_{cd} \qquad\qquad\qquad\qquad\quad \text{for} \quad \varepsilon_{c2} \le \varepsilon_c \le \varepsilon_{cu}, \end{aligned} \tag{3.1}$$

where

σ_c is the compressive stress in concrete;

η_c is a factor accounting for the brittleness of concrete, whose value is defined by

$$\begin{aligned} \eta_c &= 1.0 \qquad\qquad\quad \text{for} \quad f_{ck} \le 40\,\text{MPa}, \\ \eta_c &= \left(\frac{40}{f_{ck}}\right)^{1/3} \quad \text{for} \quad f_{ck} > 40\,\text{MPa}; \end{aligned} \tag{3.2}$$

f_{ck} is the characteristic compressive strength of concrete;

f_{cd} is the design compressive strength of concrete, calculated by

$$f_{cd} = \frac{f_{ck}}{\gamma_c}, \tag{3.3}$$

when the verification is performed at 28 days or later. The partial safety factor for concrete strength, γ_c, typically has a value of 1.4 for normal combinations;

ε_c is the compressive strain in the concrete;

ε_{c2} is the specific compressive strain in the concrete at the onset of the plastic plateau, whose value is defined by

$$\begin{aligned} \varepsilon_{c2} &= 2.0‰ && \text{for} \quad f_{ck} \leq 50\,\text{MPa}, \\ \varepsilon_{c2} &= 2.0‰ + 0.085‰ \cdot (f_{ck} - 50)^{0.53} && \text{for} \quad f_{ck} > 50\,\text{MPa}; \end{aligned} \tag{3.4}$$

ε_{cu} is the ultimate compressive strain in the concrete, whose value is defined by

$$\begin{aligned} \varepsilon_{cu} &= 3.5‰ && \text{for} \quad f_{ck} \leq 50\,\text{MPa}, \\ \varepsilon_{cu} &= 2.6‰ + 35‰ \cdot [(90 - f_{ck})/100]^4 && \text{for} \quad f_{ck} > 50\,\text{MPa}; \end{aligned} \tag{3.5}$$

n is calculated by

$$\begin{aligned} n &= 2 && \text{for} \quad f_{ck} \leq 50\,\text{MPa}, \\ n &= 1.4 + 23.4[(90 - f_{ck})/100]^4 && \text{for} \quad f_{ck} > 50\,\text{MPa}; \end{aligned} \tag{3.6}$$

In nonlinear structural analysis, the 2023 version of NBR 6118 introduced the option of using a stress-strain diagram for short-term uniaxial compression, as represented in Figure 3.2. This diagram was already included in earlier versions of the Eurocode.

Figure 3.2 – Stress-Strain Diagram for nonlinear analysis.

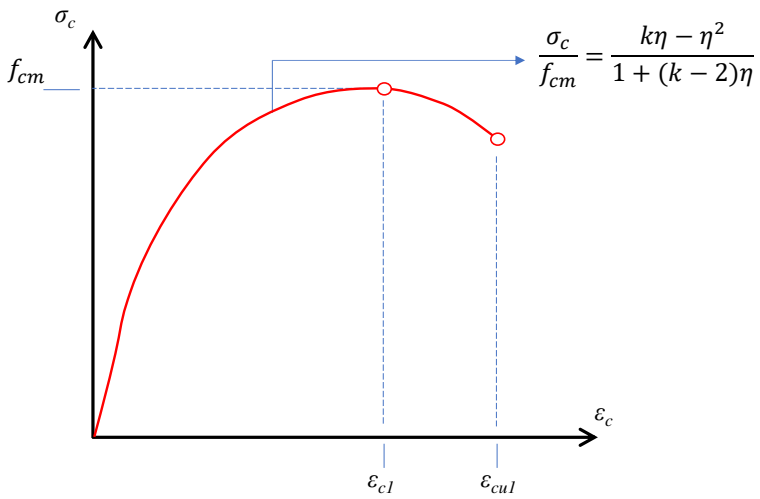

Adapted from NBR 6118 (2023).

Therefore, according to the figure, the following stress-strain relationship for nonlinear analysis may be used

$$\frac{\sigma_c}{f_{cm}} = \frac{k\eta - \eta^2}{1 + (k-2)\eta} \tag{3.7}$$

where

f_{cm} is the mean value of compressive strength of concrete, calculated by

$$f_{cm} = f_{ck} + 8 \quad \text{(MPa)}; \tag{3.8}$$

k is calculated by

$$k = \frac{1.05 E_{cm} |\varepsilon_{c1}|}{f_{cm}} \tag{3.9}$$

where

E_{cm} is the mean value of modulus of elasticity of concrete, calculated by

$$E_{cm} = 22 \cdot 10^3 \left(\frac{f_{cm}}{10} \right)^{0,3} \quad \text{(MPa)}; \tag{3.10}$$

ε_{c1} is the compressive strain in concrete at the peak stress, calculated by

$$\varepsilon_{c1} = \frac{0.7 {f_{cm}}^{0.31}}{1000} \leq 2.8‰; \tag{3.11}$$

η is calculated by

$$\eta = \frac{\varepsilon_c}{\varepsilon_{c1}}. \tag{3.12}$$

Expression (3.7) is valid for $0 < |\varepsilon_c| < |\varepsilon_{cu1}|$. ε_{cu1} is the nominal ultimate strain for this stress-strain diagram. Its value is defined by

$$\begin{aligned} \varepsilon_{cu1} &= \varepsilon_{cu} = 3.5‰ && \text{for} \quad f_{ck} \leq 50\,\text{MPa}, \\ \varepsilon_{cu1} &= \frac{2.8 + 27[(98 - f_{cm})/100]^4}{1000} && \text{for} \quad f_{ck} > 50\,\text{MPa}. \end{aligned} \tag{3.13}$$

3.1.2 Stress-Strain Diagram of Steel

According to NBR 6118 (2023), for calculations in the serviceability and ultimate limit states, the simplified diagram shown in Figure 3.3 can be used for steels with or without a yield plateau. In this diagram, the curve is linear until the yield stress is reached, beyond which a well-defined yield plateau is formed. This bilinear diagram has been considered to simulate the behavior of steel under axial stresses, both in tension and compression.

Therefore, according to the figure, the following stress-strain relationship may be used

$$\begin{aligned} \sigma_s &= E_s \varepsilon_s && \text{for} \quad 0 \leq \varepsilon_s \leq \varepsilon_{yd}, \\ \sigma_s &= f_{yd} && \text{for} \quad \varepsilon_{yd} \leq \varepsilon_s \leq \varepsilon_{su}, \end{aligned} \tag{3.14}$$

where

Figure 3.3 – Stress-Strain Diagram for passive reinforcement steel.

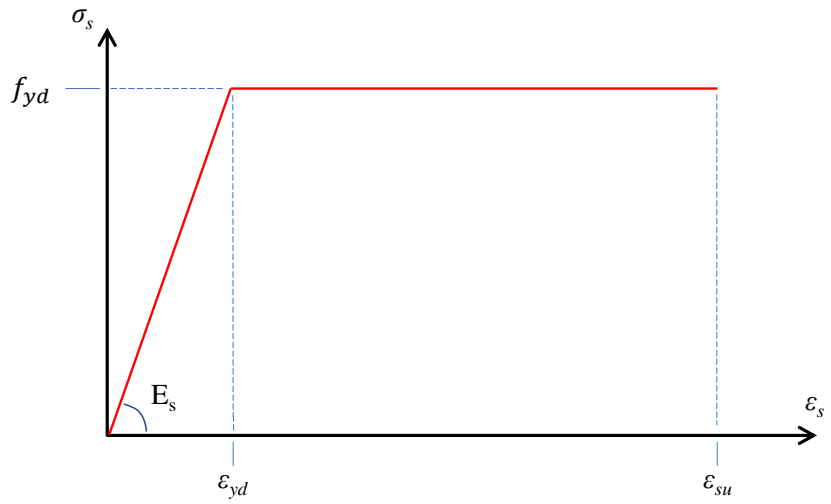

Adapted from NBR 6118 (2023).

σ_s is the stress in the passive reinforcement steel;
E_s is the modulus of elasticity of steel, assumed to be equal to 210 GPa;
ε_s is the strain in the passive reinforcement steel;
f_{yd} is the design yield strength of reinforcement, calculated by

$$f_{yd} = \frac{f_{yk}}{\gamma_s} \tag{3.15}$$

where

f_{yk} is the characteristic yield strength of reinforcement;
γ_s is the partial safety factor for reinforcing steel, which typically has a value of 1.15 for normal combinations;

ε_{yd} is the design yield strain of reinforcement steel, calculated by

$$\varepsilon_{yd} = \frac{f_{yd}}{E_s}; \tag{3.16}$$

ε_{su} is the reinforcement steel strain at failure.

3.2 SECOND-ORDER EFFECTS IN REINFORCED CONCRETE COLUMNS

NBR 6118 (2023) define *Second-Order Effects* as those effects that are superimposed on the results of a first-order analysis - where the structure is analyzed in its initial geometric configuration - when equilibrium analysis is performed considering the deformed configuration of the structure. According to the Brazilian standard, second-order effects, which must be determined considering the nonlinear behavior of materials (physical nonlinearity), can be

disregarded whenever they do not result in an increase exceeding 10% in the reactions and relevant internal forces within the structure.

A key parameter influencing the magnitude of second-order effects is the column slenderness, typically quantified by the slenderness ratio. Below, the definition of this geometric property is provided, along with a discussion of the approaches recommended by NBR 6118 (2023) for determining local second-order effects.

3.2.1 Slenderness Ratio

The slenderness ratio, denoted as λ, represents the relationship between the dimensions of the cross-section and the height of the element while accounting for the boundary conditions of the column (CASAGRANDE, 2016). This parameter is calculated using the expression

$$\lambda = \frac{\ell_e}{i} \tag{3.17}$$

where

ℓ_e is the effective length of the column. For columns assumed to be supported at both ends, the effective length is taken as the smaller of the two values (Figure 3.4)

$$\ell_e \leq \begin{cases} \ell_0 + h \\ \ell \end{cases} \tag{3.18}$$

here

ℓ_0 represents the distance between the inner faces of the structural elements, assumed to be horizontal, that provide support to the column;

h denotes the height of the column's cross-section in the direction being analyzed, as measured within the structural plane under consideration;

ℓ is the distance between the axes of the structural elements to which the element is supported;

For columns that are fixed at the base and free at the top, the effective length ℓ_e is equal to 2ℓ;

i is the radius of gyration, determined by the equation

$$i = \sqrt{\frac{I}{A}} \tag{3.19}$$

where I is the moment of inertia and A is the cross-sectional area.

Figure 3.4 – Effective length of a column.

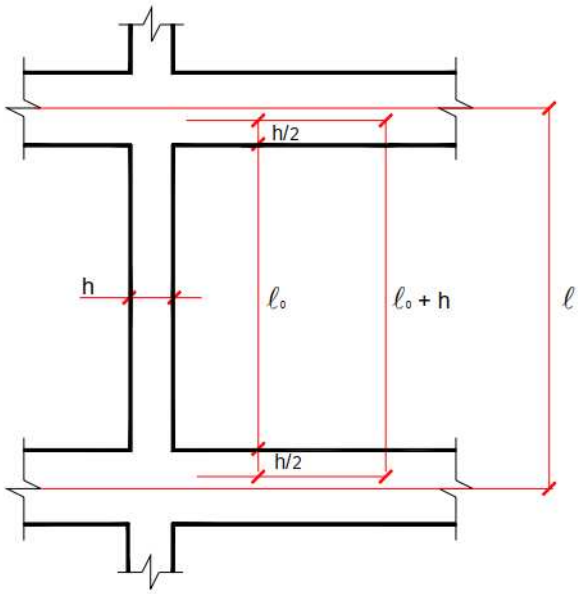

Source: Scadelai (2004).

3.2.2 Limiting Slenderness Ratio

NBR 6118 (2023) defines a limiting slenderness ratio, λ_1, below which the consideration of local second-order effects can be disregarded. This simplification is based on the premise that such effects can be neglected when their magnitude is less than 10% of the first-order response.

According to NBR 6118 (2023), the value of λ_1 depends on several factors, with the most significant being:

- the relative first-order eccentricity e_1/h at the columns end where the absolute value of the first-order moment is largest;
- the boundary conditions at the end of the isolated columns segment;
- the shape of the first-order moment diagram.

The limiting slenderness ratio, λ_1, can be calculated using the following equation

$$35 \leq \lambda_1 = \frac{25 + 12.5(e_1/h)}{\alpha_b} \leq 90 \tag{3.20}$$

where α_b depends on the boundary conditions at the column ends and the shape of the first-order moment diagram.

For columns with pinned supports at both ends and no significant transverse loads

$$\alpha_b = 0.6 + 0.4\frac{M_B}{M_A} \geq 0.4 \tag{3.21}$$

here, M_A and M_B are the first-order moments at the column ends. For non-sway structures, these moments are obtained from a first-order analysis, while for sway structures, they correspond to the total moments (first-order + global second-order). The value of M_A should be taken as the largest absolute moment, and M_B is positive if it generates tension on the same face as M_A; otherwise, it is negative.

For columns with significant transverse loads along their height, columns with moments smaller than the minimum moment, or cantilever columns

$$\alpha_b = 1.0. \tag{3.22}$$

The minimum moment, which accounts for local imperfections in the column, should be calculated according to NBR 6118 (2023):

$$M_{1d,\min} = N_d(0.015 + 0.03h) \tag{3.23}$$

where N_d is the design axial force h is the total height of the cross-section in the considered direction, expressed in meters.

3.2.3 Classification of Columns According to the Slenderness Ratio

According to NBR 6118 (2023), the applicability of the recommended methods for calculating second-order effects depends on the slenderness ratio of the column. While the classification presented below is not explicitly included in the standard, it is frequently found in the literature. It is a practical framework for categorizing columns based on their slenderness ratio. This classification guides the selection of the appropriate calculation method in compliance with normative requirements.

- **Short columns**: $\lambda < \lambda_1$: Local second-order effects can be neglected;
- **Moderately slender columns**: $\lambda_1 < \lambda \leq 90$: Local second-order effects can be analyzed using approximate methods based on the Standard Column approach;
- **Slender columns**: $90 < \lambda \leq 140$: Local second-order effects can be analyzed using the Standard Column method combined with $M, N, 1/r$; the consideration of creep is mandatory;

- **Very slender columns**: $140 < \lambda \leq 200$: Second-order effects must be analyzed using the General Method. The consideration of creep is mandatory.

NBR 6118 (2023) does not allow columns with slenderness ratios greater than 200, except in lightly compressed columns, where the axial force is less than $0,10 f_{cd} A_c$. For columns with a slenderness ratio exceeding 140, local second-order effects must be amplified by an additional factor, which is determined as

$$\gamma_{n1} = 1 + \frac{\lambda - 140}{140} \geq 1. \tag{3.24}$$

3.3 CALCULATION OF SECOND-ORDER EFFECTS IN COLUMNS

This section focuses on the mathematical approaches and methods used to calculate second-order effects in reinforced concrete columns. Building on the theoretical concepts previously discussed, the presented methodologies range from simplified techniques to more advanced methods, highlighting their assumption, procedures, and applications.

3.3.1 Approximate Method of the Standard Column

As highlighted by Carvalho and Pinheiro (2009), approximate methods based on the Standard Column aim to identify the most critical section of the columns and, through simplifications, derive expressions for calculating second-order effects. This method applies to columns with a constant cross-section, including uniform reinforcement along their entire length (FUSCO, 1981).

According to Fusco (1981), the *Standard Column* is a cantilever column with an effective length of $\ell_e = 2\ell$, as illustrated in Figure 3.5. The method assumes a curvature distribution that produces a deflection a at the free end of the column, given by

$$a = \frac{{\ell_e}^2}{10} \left(\frac{1}{r} \right) \tag{3.25}$$

where $1/r$ is the curvature at the section of maximum deflection.

In the standard column model, the maximum deflection is linearly related to the curvature of the column, as shown in Eq. (3.25). The curvature is approximated as the second derivative of the elastic curve equation, which is assumed to follow a sinusoidal function (CARVALHO; PINHEIRO, 2009). Accordingly, the elastic curve of the column's axis is expressed as

Figure 3.5 – Standard Column.

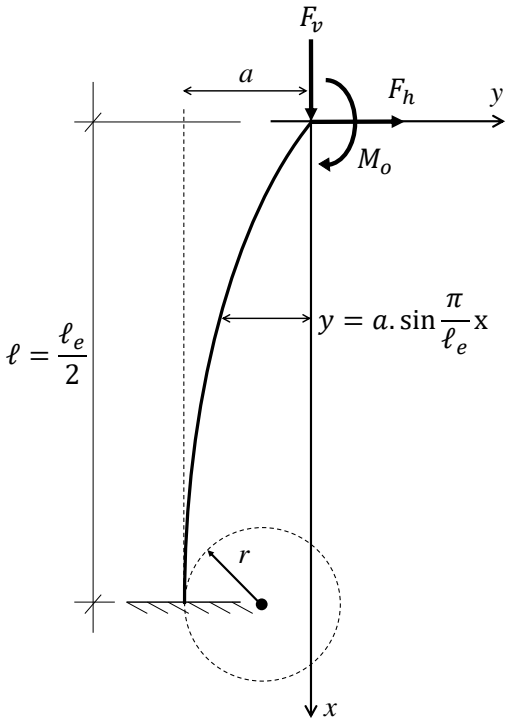

Adapted from Fusco (1981).

$$y(x) = -a\sin\left(\frac{\pi}{\ell_e}x\right). \tag{3.26}$$

Assuming small displacements, the curvature $(1/r)$ can be represented as the second derivative of the elastic curve

$$\frac{1}{r} = \frac{d^2y}{dx^2} = a\left(\frac{\pi}{\ell_e}\right)^2 \sin\left(\frac{\pi}{\ell_e}x\right). \tag{3.27}$$

By evaluating the curvature at $x = \ell_e/2$, which corresponds to the base section, and approximating $\pi^2 \cong 10$, Eq. (3.25) is obtained. In this method, the second-order eccentricity (e_2) is assumed to be equal to the deflection a

$$e_2 = \frac{{\ell_e}^2}{10}\left(\frac{1}{r}\right). \tag{3.28}$$

3.3.1.1 Standard Column Method with Approximate Curvature

According to NBR 6118 (2023), this method applies exclusively to columns with $\lambda \leq 90$, having a constant cross-section and the same symmetrically distributed reinforcement along their entire length.

In this approach, geometric nonlinearity is handled approximately by assuming a sinusoidal deformation of the column, as outlined earlier in this section. Physical nonlinearity is accounted for using an approximate expression for the curvature at the critical cross-section (NBR 6118, 2023).

The maximum total internal moment in the column, $M_{d,tot}$, is determined at an intermediate section and can be expressed as the sum of the first-order and second-order moments

$$M_{d,tot} = M_1 + M_2 = \alpha_b M_{1d,A} + N_d e_2 \geq M_{1d,A} \tag{3.29}$$

where $M_{1d,A}$ is the design value of the first-order moment, M_A.

By substituting e_2 from Eq. (3.28) into Eq. (3.29), the following equation is obtained

$$M_{d,tot} = \alpha_b M_{1d,A} + N_d \frac{{l_e}^2}{10}\left(\frac{1}{r}\right) \geq M_{1d,A}. \tag{3.30}$$

The equation that defines the curvature for combined axial load and bending can be written as

$$\frac{1}{r} = \frac{(\varepsilon_c + \varepsilon_s)}{(\nu + 0.5)h} \tag{3.31}$$

where h represents the height of the cross-section in the analyzed direction, and ν is the dimensionless axial force, defined as

$$\nu = \frac{N_d}{A_c f_{cd}}. \tag{3.32}$$

In this approximate method, it is conservatively assumed that the curvature should take the highest possible value. Consequently, the concrete and steel strains are considered equal to their ultimate limit state values (CARVALHO; PINHEIRO, 2009).

For concretes with $f_{ck} \leq 50\,\text{MPa}$, the maximum strain value is

$$\varepsilon_c = \varepsilon_{cu} = 3.5‰. \tag{3.33}$$

For CA-50 steels with a yield strength of $f_{yk} = 500\,\text{MPa}$ and $\gamma_s = 1.15$, the yield strain is calculated according to Eq. (3.16)

$$\varepsilon_s = \varepsilon_{yd} = \frac{f_{yd}}{E_s} = \frac{500/1.15}{210000} = 2.07‰. \tag{3.34}$$

The expression for critical curvature adopted in NBR 6118 (2023) is obtained by substituting Eqs. (3.33) and (3.34) into Eq. (3.31)

$$\frac{1}{r} = \frac{0.005}{h(\nu + 0.5)} \leq \frac{0.005}{h}. \tag{3.35}$$

3.3.1.2 Standard Column Method with Approximate Stiffness κ

Similar to the Standard Column Method with Approximate Curvature, this approach is restricted to columns with $\lambda \leq 90$, featuring a constant rectangular cross-section and symmetrical reinforcement uniformly distributed along the axis (NBR 6118, 2023).

In this method, geometric nonlinearity is approximated by assuming a sinusoidal deformation of the column, while physical nonlinearity is addressed through an approximate expression for stiffness (NBR 6118, 2023).

The maximum total internal moment, $M_{d,tot}$, is calculated as a function of the dimensionless stiffness κ using the equation

$$M_{d,tot} = \frac{\alpha_b M_{1d,A}}{1 - \dfrac{\lambda^2}{120\kappa/\nu}} \geq M_{1d,A}. \tag{3.36}$$

The dimensionless stiffness κ is approximated by

$$\kappa_{\text{aprox}} = 32\left(1 + 5\frac{M_{d,tot}}{hN_d}\right)\nu. \tag{3.37}$$

It is important to note that Eqs. (3.36) and (3.37) are interdependent, requiring an iterative solution process. According to NBR 6118 (2023), convergence is typically achieved after two or

three iterations. Nevertheless, the standard provides a direct formulation specifically applicable to rectangular sections, expressed as

$$aM_{d,tot}^2 + bM_{d,tot} + c = 0 \tag{3.38}$$

where

$$\begin{cases} a = 5h, \\ b = h^2 N_d - \dfrac{N_d l_e^2}{320} - 5h\alpha_b M_{1d,A}, \\ c = -N_d h^2 \alpha_b M_{1d,A}. \end{cases} \tag{3.39}$$

The final moment, $M_{Sd,tot}$ is obtained by solving the quadratic equation (3.38), taking the positive root

$$M_{Sd,tot} = \frac{-b + \sqrt{b^2 - 4ac}}{2a}. \tag{3.40}$$

3.3.1.3 Standard Column Method Coupled with $M, N, 1/r$ Diagrams

This method can be applied to columns with $\lambda \leq 140$. Physical nonlinearity is considered more rigorously compared to the previously discussed approaches, but still approximately, by determining the curvature of the critical section using specific $M, N, 1/r$ diagrams. Geometrical nonlinearity is also treated approximately, assuming a sinusoidal column deformation.

The methodology is similar to the Standard Column Method with Approximate Stiffness (Subsection 3.3.1.2), but replaces κ_{aprox} with κ_{sec} (secant stiffness), which is calculated as

$$\kappa_{\text{sec}} = \frac{(EI)_{\text{sec}}}{A_c h^2 f_{cd}} \tag{3.41}$$

where $(EI)_{\text{sec}}$ represents the slope of the secant line in the $M, N, 1/r$ diagram (Figure 3.6). The construction of this diagram is discussed further. Once κ_{sec} is determined, it is substituted into κ in Eq. (3.36) to calculate the maximum total internal moment in the column, $M_{d,tot}$.

It is important to note that applying this method requires detailed information about the reinforcement layout, which is necessary for constructing the $M, N, 1/r$ diagram.

3.3.1.3.1 $M,N,1/r$ Diagrams

According to NBR 6118 (2023), the effect of physical nonlinearity can be accounted for by constructing a material relationship known as the moment-axial force-curvature ($M,N,1/r$) diagram. This relationship represents the response of the reinforced concrete cross-section under the combined action of a constant axial force and a progressively increasing bending moment, considering the actual strains of both concrete and steel (CASAGRANDE, 2016). This relationship allows for evaluating the nonlinear behavior of reinforced concrete cross-sections, incorporating the physical nonlinearity of both steel and concrete (RIBEIRO, 2011). Therefore, the construction of this relationship must be performed for each cross-section, with the reinforcement layout known, and for the specific value of the applied axial force.

The standard also recommends the use of a *safety formulation*, where the material diagram $M,N,1/r$ is built using forces that have been pre-factored by γ_f/γ_{f3}, where γ_f is the partial safety factor for actions, given by $\gamma_f = \gamma_{f1} \cdot \gamma_{f2} \cdot \gamma_{f3}$, and which has a value of 1,4 for normal combinations of permanent and variable actions. The results of the analysis should then be further amplified by the remaining portion of the safety factor, γ_{f3}, the component of the partial safety factor γ_f, which accounts for deviations arising from construction processes and approximations made in the design with respect to load effects, equal to 1,1. Additionally, the deformability of the elements should be determined based on idealized stress-strain diagrams for concrete and steel, with the peak stress of the concrete taken as $1,10 f_{cd}$. The graphical representation of the moment-curvature relationship is illustrated in Figure 3.6.

Figure 3.6 – Moment-curvature relationship.

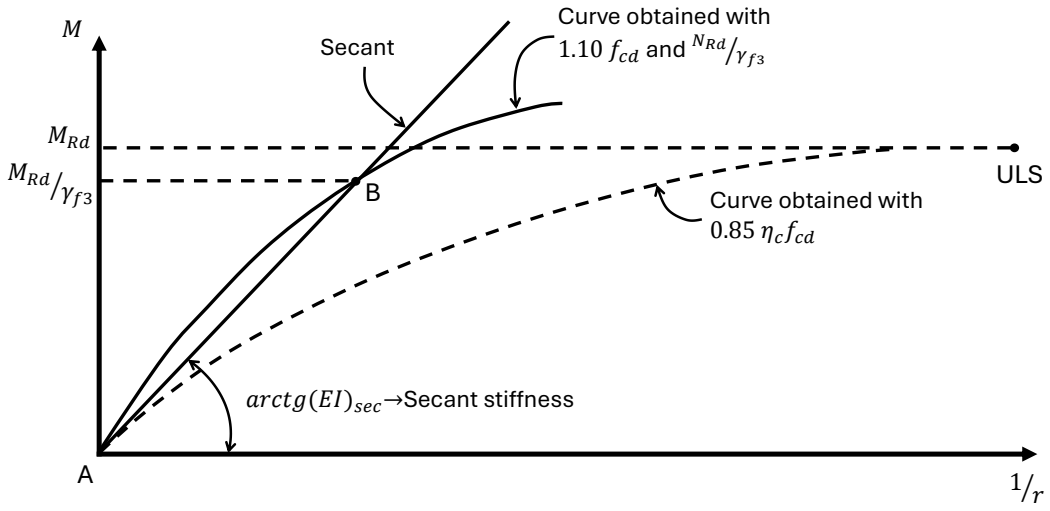

Adapted from NBR 6118 (2023).

For application within the Standard Column Method coupled with $M, N, 1/r$ diagrams, the curve AB can be linearized for safety purposes as a straight line, representing the secant stiffness, $(EI)_{\text{sec}}$.

The dashed curve, which is constructed using the design values of the strengths of both concrete and steel, is used to determine the design bending resistance M_{Rd} corresponding to the design axial resistance N_{Rd} (at the maximum point), allowing the identification of point B. On the other hand, the solid line is used to calculate deformations.

As noted by Casagrande (2016), constructing the moment-axial force-curvature diagram, which is necessary for the application of the Standard Column Method coupled with $M, N, 1/r$ diagrams as well as the General Method discussed later, is a labor-intensive and complex process that involves iterative calculations and successive approximations. Although these calculations are too extensive to be performed manually, they can be automated using specialized software.

3.3.2 General Method

The *General Method* involves a second-order analysis through an appropriate discretization of the column. This method considers physical nonlinearity by successively evaluating the actual $M, N, 1/r$ relationship for each section, while geometric nonlinearity is considered in a non-approximate manner by progressively increasing the initial applied moments during each iteration of the displacement calculations. While this method is mandatory for columns with $\lambda \geq 140$, it can also be applied to columns of any slenderness ratio when higher accuracy is desired.

In applying the General Method, the column is first discretized by dividing its length into smaller elements. This approach allows for considering varying characteristics along the column, such as changes in cross-section or reinforcement layout. The response of each segment is calculated individually, taking into account their interactions, with the accuracy of the results depending on the number of divisions used.

According to Borges (1999), the principle of this method is to determine, for each segment under load, a stable deformed position that corresponds to an equilibrium state between internal forces and external actions. This is achieved while maintaining compatibility among curvatures, strains, and the neutral axis position and satisfying the materials' constitutive equations.

As highlighted by Ribeiro (2011), the General Method provides greater accuracy in the results, both in terms of the physical and geometric nonlinear behavior of structural elements. However, accounting for nonlinear behavior requires iterative methods, often based on incremental loading, progressive eccentricity increases, or variations in deflection.

Casagrande (2016) emphasizes that the precision and comprehensiveness of the General Method are accompanied by significant complexity. The author notes that historically, this method was restricted to academic environments or applied in cases of extreme necessity. However, its adoption has increased, driven by advancements in computational processing capabilities.

4 CREEP SIMULATION

Creep is the phenomenon of increasing deformations in concrete over time when subjected to sustained loads, as discussed in Section 2.3.

The following sections present a variety of strategies for incorporating creep effects, as found in the literature. In particular, these strategies can be applied in conjunction with the methods for calculating second-order effects in reinforced concrete columns, as described in Section 3.3.

It is important to note that NBR 6118 (2023) mandates the consideration of creep in the analysis of second-order effects in columns with slenderness ratios $\lambda > 90$. On the other hand, EN 1992-1-1 (2004) allows creep effects to be disregarded only when the following three conditions are met:

- $\varphi(\infty, t_0) \leq 2$,
- $\lambda \leq 75$,
- $e_1 \geq h$,

where φ is the *creep coefficient*, as defined in the following section.

4.1 CREEP COEFFICIENT φ

The strategies outlined in NBR 6118 (2023) for considering creep effects are simplified approaches relying on the *creep coefficient* $\varphi(t_\infty, t_0)$, which is independent of the applied stress. However, more advanced methods go beyond using the creep coefficient and incorporate full creep compliance functions to better capture time-dependent effects. The creep coefficient's primary advantage is its simplicity, as it describes creep effects using a single parameter (WESTERBERG, 2008).

4.1.1 Creep Coefficient φ according to NBR 6118 (2023)

For elements subjected to stresses below 0.5 f_c and in cases where high precision is not necessary, $\varphi(t_\infty, t_0)$ can be approximately obtained through linear interpolation using Table 4.1. This table, provided by NBR 6118 (2023), presents creep coefficient values as a function of average ambient humidity and the fictitious thickness of the element h_{fic}, calculated using Eq. 2.2. The table values apply to concrete at temperatures ranging from 10 °C to 20 °C, but the standard allows their use for temperatures between 0 °C and 40 °C. These values apply to concrete produced with ordinary Portland cement.

Table 4.1 – Upper characteristic values of the creep coefficient $\varphi(t_\infty, t_0)$.

Average Ambient Humidity (%)			40		55		75		90	
Fictitious Thickness (cm) $2A_c/u$			20	60	20	60	20	60	20	60
$\varphi(t_\infty, t_0)$ Concrete Classes C20 to C45	t_0 **days**	5	4.6	3.8	3.9	3.3	2.8	2.4	2.0	1.9
		30	3.4	3.0	2.9	2.6	2.2	2.0	1.6	1.5
		60	2.9	2.7	2.5	2.3	1.9	1.8	1.4	1.4
$\varphi(t_\infty, t_0)$ Concrete Classes C50 to C90		5	2.7	2.4	2.4	2.1	1.9	1.8	1.6	1.5
		30	2.0	1.8	1.7	1.6	1.4	1.3	1.1	1.1
		60	1.7	1.6	1.5	1.4	1.2	1.2	1.0	1.0

Adapted from NBR 6118 (2023).

For conditions differing from those outlined above, specific creep coefficient values $\varphi(t_\infty, t_0)$ must be determined according to the calculation procedures described in Annex A of NBR 6118 (2023).

This calculation procedure was also employed in a comparative study that evaluates the values presented in Table 4.1, given that NBR 6118 (2023) does not explicitly specify the origin of these values. The results of this study are provided in Appendix A.

In the detailed procedure presented in the Annex of the Brazilian standard, the creep strain ε_{cc} comprises two components: rapid and delayed. The rapid strain, ε_{cca}, is irreversible and occurs within 24 hours after load application. Conversely, the delayed strain consists of two parts: the irreversible delayed strain, ε_{ccf}, and the reversible delayed strain, ε_{ccd} (NBR 6118, 2023). Thus, the creep strain ε_{cc} can be expressed as the sum of the three components

$$\varepsilon_{cc} = \varepsilon_{cca} + \varepsilon_{ccf} + \varepsilon_{ccd}. \tag{4.1}$$

The total creep strain, ε_{cc}, can also be calculated by multiplying the immediate strain ε_c by the creep coefficient φ

$$\varepsilon_{cc} = \varphi \varepsilon_c. \tag{4.2}$$

Thus, the total strain in concrete, expressed as the sum of the immediate strain and the creep strain, can be written solely in terms of the immediate strain and the creep coefficient

$$\varepsilon_{c,total} = \varepsilon_c + \varepsilon_{cc} = (1+\varphi)\varepsilon_c. \tag{4.3}$$

Similarly, the creep coefficient φ can be expressed as the sum of its rapid, irreversible delayed, and reversible delayed components

$$\varphi = \varphi_a + \varphi_f + \varphi_d. \tag{4.4}$$

For calculating the individual components of φ, under service-levels stresses, NBR 6118 (2023) adopts the following assumptions:

a) Creep strain ε_{cc} varies linearly with applied stress;
b) When stress increments are applied at different times, the corresponding creep effects are additive;
c) Rapid deformation results in constant strain over time, and φ_a depends on the ratio of concrete strength at loading to its final strength;
d) The reversible delayed strain coefficient φ_d depends solely on load duration; it's independent of concrete age at loading;
e) The irreversible delayed strain coefficient φ_f depends on ambient relative humidity U, concrete consistency at placement, fictitious thickness h_{fic}, and the concrete's fictitious age at load application (t_0) and at the time considered (t);
f) Irreversible delayed strain curves for varying loading ages can be derived from one another by parallel shifts along the strain axis.

According to NBR 6118 (2023), the creep coefficient $\varphi(t,t_0)$ is defined as

$$\varphi(t,t_0) = \varphi_a + \varphi_{f\infty}[\beta_f(t) - \beta_f(t_0)] + \varphi_{d\infty}\beta_d \tag{4.5}$$

where

- t or t_0 is the fictitious age of the concrete at the time of interest, expressed in days, calculated by

$$t = \alpha \sum_i \frac{T_i + 10}{30} \Delta t_{\text{ef,i}} \tag{4.6}$$

where

α is a coefficient dependent on the hardening rate of the cement. In the absence of experimental data, NBR 6118 (2023) allows the use of the following values: 1

for slow-hardening Portland cement (CP III and CP IV), 2 for normal-hardening Portland cement (CP I and CP II), and 3 for rapid-hardening Portland cement (CP V-ARI),

T_i is the average daily ambient temperature, expressed in degrees Celsius (°C),

$\Delta t_{\text{ef, i}}$ is the period, expressed in days, during which the average daily ambient temperature, T_i, can be assumed constant;

- φ_a is the rapid creep coefficient determined by the expression

$$\begin{aligned} \varphi_a &= 0.8\left[1-\frac{f_c(t_0)}{f_c(t_\infty)}\right] \quad \text{for} \quad 20\,\text{MPa} \leq f_{ck} \leq 45\,\text{MPa}, \\ \varphi_a &= 1.4\left[1-\frac{f_c(t_0)}{f_c(t_\infty)}\right] \quad \text{for} \quad 50\,\text{MPa} \leq f_{ck} \leq 90\,\text{MPa}, \end{aligned} \tag{4.7}$$

where $\frac{f_c(t_0)}{f_c(t_\infty)}$ is the function representing the strength growth of the concrete over time;

- $\varphi_{f\infty}$ is the final value of the irreversible delayed creep coefficient calculated by

$$\begin{aligned} \varphi_{f\infty} &= \varphi_{1c}\varphi_{2c} \quad \text{for} \quad 20\,\text{MPa} \leq f_{ck} \leq 45\,\text{MPa}, \\ \varphi_{f\infty} &= 0.45\varphi_{1c}\varphi_{2c} \quad \text{for} \quad 50\,\text{MPa} \leq f_{ck} \leq 90\,\text{MPa}, \end{aligned} \tag{4.8}$$

where

φ_{1c} is the coefficient dependent on the ambient relative humidity U, expressed as a percentage (%), and the consistency of the concrete, as shown in Table 4.2,

φ_{2c} is the coefficient dependent on the fictitious thickness h_{fic} of the element

$$\varphi_{2c} = \frac{42+h}{20+h} \tag{4.9}$$

Table 4.2 – Typical numerical values for determining creep.

Environment	**Humidity U (%)**	**Creep φ_{1c}** [1]			γ [2]
		Slump (cm)			
		0 - 4	5 - 9	10 - 15	
In water	–	0.6	0.8	1.0	30.0
In a very humid environment directly above water	90	1.0	1.3	1.6	5.0
Outdoors, in general	70	1.5	2.0	2.5	1.5
In a dry environment	40	2.3	3.0	3.8	1.0

[1] $\varphi_{1c} = 4.45 - 0.035U$ for slump between 5 to 9 cm and $U \leq 90\%$

[2] $\gamma = 1 + \exp(-7.8 + 0.1U)$ for $U \leq 90\%$

Adapted from NBR 6118 (2023).

where h is the weighted fictitious thickness

$$h = \gamma h_{\text{fic}}, \tag{4.10}$$

expressed in centimeters, with γ defined in Table 4.2;

- $\beta_f(t)$ or $\beta_f(t_0)$ is the coefficient related to irreversible delayed strain as a function of concrete age, obtained from the expression

$$\beta_f(t) = \frac{t^2 + At + B}{t^2 + Ct + D} \tag{4.11}$$

where

$$\begin{aligned} A &= 42h^3 - 350h^2 + 588h + 113, \\ B &= 768h^3 - 3060h^2 + 3234h - 23, \\ C &= -200h^3 - 13h^2 + 1090h + 183, \\ D &= 7579h^3 - 31916h^2 + 35343h + 1931, \end{aligned} \tag{4.12}$$

where h is the weighted fictitious thickness, calculated using Eq. (4.10), expressed in meters. For values of h outside the range ($0.05 \leq h \leq 1.6$), the extreme values are adopted;

- $\varphi_{d\infty}$ is the final value of the reversible delayed creep coefficient, which is considered equal to 0.4;
- $\beta_d(t)$ is the coefficient related to reversible delayed strain as a function of the elapsed time ($t - t_0$) after loading, calculated as

$$\beta_d(t) = \frac{t - t_0 + 20}{t - t_0 + 70}. \tag{4.13}$$

Equation (4.5), already present in the CEB-FIP Model Code 1978 (CEB-FIP, 1978 apud MOLA; PELLEGRINI, 2012), has been widely used in creep modeling for concrete structures. However, it may no longer fully reflect the advancements in understanding the material's viscoelastic behavior. The study by Mola and Pellegrini (2012) explores the evolution of creep models, emphasizing the refinements introduced in the fib Model Code 2010 (FIB, 2012 apud MOLA; PELLEGRINI, 2012) compared to its predecessors. The Brazilian standard, however, still relies on the methodology of CEB-FIP Model Code 1978 (CEB-FIP, 1978 apud MOLA; PELLEGRINI, 2012), which presents significant limitations, such as the assumption of an instantaneous creep deformation immediately after loading. According to Mola and Pellegrini (2012), while this simplification facilitated the use of separate aging and non-aging formulation, it neglected nonlinear aspects of creep and it does not explicitly differentiate between basic creep and drying creep.

The work of Mola and Pellegrini (2012) demonstrates that more recent models, such as the present in the fib Model Code 2010 (FIB, 2012 apud MOLA; PELLEGRINI, 2012),

address these inconsistencies by adopting a more refined formulation that distinguishes creep components and better accounts for environmental variables and concrete strength evolution. Their results indicate that using older models can lead to discrepancies in structural analysis, particularly in elements where creep plays a crucial role, highlighting the need for Brazilian standards to incorporate more advanced formulations.

In addition, many other methodologies for calculating the creep coefficient can be found in the literature.

4.1.2 Effective Creep Coefficient φ_{ef}

Typically, the creep coefficient is considered under the deformations caused by the total applied load on the structure. However, since applied loads generally include short- and long-term components, only long-term components influence all aspects of creep. To address this, the creep coefficient φ is reduced to account for the proportion of long-term bending moments in a given load combination (WESTERBERG, 2008). This reduction results in an effective creep coefficient φ_{ef}, as proposed by EN 1992-1-1 (2004),

$$\varphi_{ef} = \varphi \frac{M_{Sg}}{M_d} \tag{4.14}$$

where M_{Sg} is the first-order moment due to the quasi-permanent load combination (SLS), and M_d is the first-order design moment (ULS).

4.2 APPROXIMATE METHOD OF ADDITIONAL ECCENTRICITY e_{cc}

In the simulation of local second-order effects in columns, NBR 6118 (2023) allows for an approximate consideration of creep effects through the additional eccentricity e_{cc}, which is computed as

$$e_{cc} = \left(\frac{M_{sg}}{N_{sg}} + e_a \right) \left(2.718^{\frac{\varphi N_{sg}}{N_e - N_{sg}}} - 1 \right) \tag{4.15}$$

where

- N_e is the Euler critical load, calculated as

$$N_e = \frac{10 E_{ci} I_c}{{\ell_e}^2}; \tag{4.16}$$

- e_a represents the eccentricity due to local imperfections, as defined in NBR 6118 (2023);

- M_{sg} e N_{sg} are the applied bending moment and axial force, respectively, due to the quasi-permanent load combination;
- φ is the creep coefficient;
- E_{ci} is the initial tangent modulus of elasticity of concrete, calculated, when tests are not performed, using equations

$$\begin{aligned} E_{ci} &= \alpha_E \cdot 5600\sqrt{f_{ck}} && \text{for} \quad f_{ck} \leq 50\,\text{MPa}, \\ E_{ci} &= 21.5 \cdot 10^3 \alpha_E \left(\frac{f_{ck}}{10} + 1.25\right)^{1/3} && \text{for} \quad f_{ck} > 50\,\text{MPa}, \end{aligned} \tag{4.17}$$

  where α_E is a parameter dependent on the nature of the aggregate, whose value is defined as
  - $\alpha_E = 1.2$ for basalt and diabase;
  - $\alpha_E = 1.0$ for granite and gneiss;
  - $\alpha_E = 0.9$ for limestone;
  - $\alpha_E = 0.7$ for sandstone;
- I_c is the moment of inertia of the concrete section;
- ℓ_e is the effective length of the column, as defined in Eq. (3.18).

The additional eccentricity e_{cc} should be incorporated into the total eccentricity as an immediate effect that adds to the first-order eccentricity e_1. This eccentricity will be used with approximate methods based on the standard column model to calculate second-order effects.

4.3 EXTENDED STRESS-STRAIN CURVE METHOD

The *Extended Stress-Strain Curve Method* is considered a more rigorous approach than the *Approximate Method of Additional Eccentricity*, although it remains a simplified method. Quast (1978 apud CASAGRANDE, 2016) was the first to propose this method. In Brazil, Fusco (1981) is recognized as one of the key figures in disseminating this approach.

The method is based on the assumption that the creep strain ε_{cc} is obtained by multiplying the immediate strain of concrete ε_c by the creep coefficient φ, as given by Eq. (4.3)

$$\varepsilon_{c,total} = \varepsilon_c + \varepsilon_{cc} = (1+\varphi)\varepsilon_c. \tag{4.3}$$

As a result, the stress-strain curve shifts parallel to the ε_c axis by a factor of φ, as illustrated in Figure 4.1.

This method is included in EN 1992-1-1 (2004), although it is not currently adopted in the Brazilian standard. The Eurocode allows adopting this strategy within the General Method in

Figure 4.1 – Extended stress-strain curve due to the consideration of creep effects.

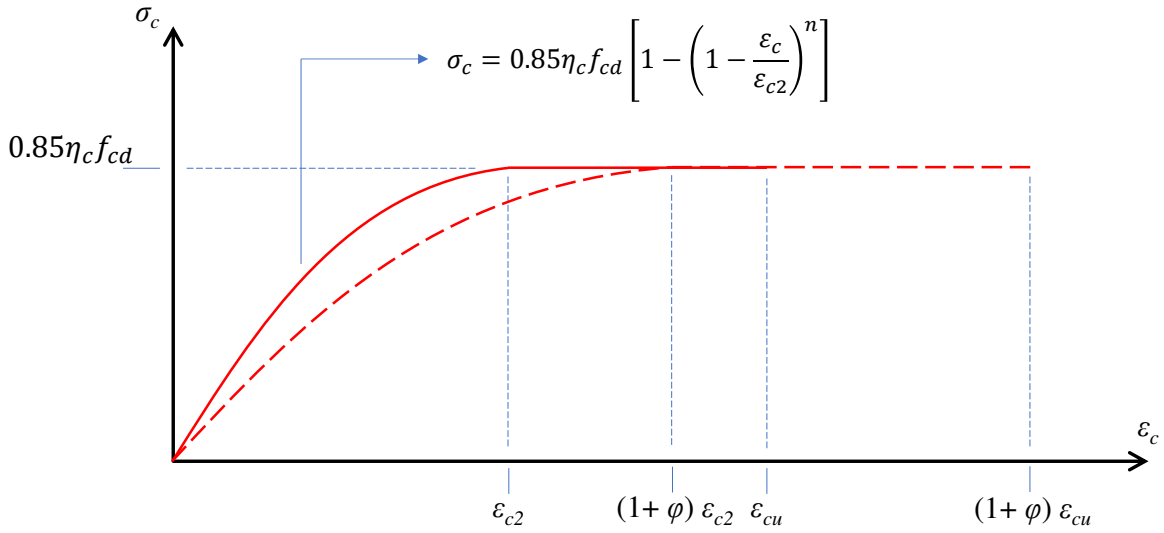

the absence of a more refined model, employing the effective creep coefficient φ_{ef} and utilizing the stress-strain diagram for nonlinear analysis, as illustrated in Figure 3.2. International studies, such as Westerberg (2008), follow the same approach. However, Brazilian studies, typically based on Fusco (1981), apply the same strategy differently, implementing it on the idealized stress-strain diagram (Figure 3.1) and introducing the shift based on the creep coefficient φ (exactly as illustrated in Figure 4.1).

Westerberg (2008) highlights certain limitations of this approach, as neither the extended stress-strain curve nor the creep coefficient accurately represents the fundamental behavior of creep for the following reasons:

1. The creep coefficient is defined for stresses within the elastic range. When used to shift the stress-strain curve, it is applied to the entire curve, even beyond the peak stress, which lacks physical significance.
2. Concrete stress evolves over time due to creep, as deflections increase and stress re-distributes from concrete to reinforcement. This redistribution varies across the cross-section, leading to localized stress increases or reductions.
3. The primary advantage of using the creep coefficient is its main limitation: Westerberg (2008) question whether it is genuinely possible to describe a complex phenomenon – affected by varying load levels and combinations – using a single parameter.

The author argues that, given these limitations, the accuracy of the extended stress-strain curve approach is debatable, although such a curve does not necessarily require a strict physical interpretation. Westerberg (2008) concludes that, despite its simplifications, this method is an effective and sufficiently accurate approach for practical engineering applications.

4.3.1 Standard Column Method Coupled with $M,N,1/r$ Diagrams Incorporating Creep

For more comprehensive models that characterize column behavior, creep simulation strategies are integrated with methods used for second-order effect calculations.

Thus, when applying the *Standard Column Method Coupled with $M,N,1/r$ diagrams*, creep can be incorporated through the extended stress-strain diagram, which is used to construct the $M,N,1/r$ diagrams. By applying the concepts introduced in the preamble of this subsection, it is possible to derive the $M,N,1/r$ diagram with creep effects incorporated

$$\left(\frac{1}{r}\right)_{total} = \frac{\varepsilon_s + \varepsilon_{c,total}}{d} \therefore \left(\frac{1}{r}\right)_{total} = \frac{\varepsilon_s + (1+\varphi)\varepsilon_c}{d}. \tag{4.18}$$

Once the $M,N,1/r$ diagram incorporating creep is obtained, the Standard Column Method can be applied, as presented in Subsection 3.3.1.3, leading to the secant stiffness κ_{sec} according to Eq. (3.41).

4.3.2 General Method Coupled with $M,N,1/r$ Diagrams Incorporating Creep

The $M,N,1/r$ diagram incorporating creep can also be used with the general method for second-order effects calculations. However, instead of employing a secant stiffness, as presented in the previous subsection, this approach considers the current material state, including creep effects, in an incremental iterative process.

4.4 MATHEMATICAL MODELS WITH ANALYTICAL INCORPORATION OF THE TIME VARIABLE

Mathematical models incorporating the time variable analytically aim to provide a more realistic representation of the viscoelastic behavior of materials, including concrete. In general, creep phenomena can be described by expressions of the form

$$\varepsilon(t,\sigma,T) = \sigma J(t,\sigma,T) \tag{4.19}$$

where σ is the applied stress, $\varepsilon(t,\sigma,T)$ is the creep strain as a function of time, stress, and temperature, and $J(t,\sigma,T)$ is the specific creep function or creep compliance function.

The predominant approaches in the literature for modeling creep include empirical formulations, primarily represented by Findley's Power Law, integral, and differential formulations.

Findley's Power Law is widely used and has demonstrated satisfactory accuracy in predicting the creep behavior of polymeric materials and polymer matrix composites (Sá, 2007 apud BECHO, 2020). Other empirical equations can also be found in the literature, such as Norton's Equation and Nadai's Equation; however, they are not directly relevant to the scope of this study and will not be explored in detail.

According to Becho (2020), the integral formulation is the most widely used in the literature to represent viscoelastic behavior. In this approach, strain is expressed in terms of applied stresses through a time-integral relation

$$\varepsilon(t) = J_0\sigma + \int_0^t J_t(t-\tau)\frac{d\sigma(\tau)}{d\tau}d\tau \tag{4.20}$$

where

- σ is the applied stress,
- τ is an auxiliary time variable,
- t represents the elapsed time after loading,
- J_0 is the time-independent creep function,
- $J_t(t)$ is the time-dependent creep function.

In this approach, accurately determining the viscoelastic behavior requires defining appropriate creep functions and material parameters that reflect experimentally observed viscoelastic behavior. In such cases, exponential functions or functions derived from rheological models based on the Prony series are typically used (BECHO, 2020).

An alternative widely used approach to describe viscoelastic behavior is the differential formulation, given by

$$\sigma + R_1\frac{d\sigma}{dt} + \cdots + R_n\frac{d^n\sigma}{dt^n} = Q_0\varepsilon + Q_1\frac{d\varepsilon}{dt} + \cdots + Q_n\frac{d^n\varepsilon}{dt^n} \tag{4.21}$$

where the parameters R_n and Q_n are material properties that depend on time, temperature, and stress levels. These parameters can also be determined from rheological models, which characterize time-dependent material behavior. These rheological models provide a physical interpretation of the mathematical formalism described by differential equations, such as (4.21). According to Becho (2020), rheological relationships – transient equations that relate stress and strain – differ from constitutive relationships in that they explicitly account for time-dependent effects, which are crucial for the numerical description of viscoelastic materials.

Becho (2020) further states that rheological models representing mechanical behavior consist of elastic elements (springs), viscous elements (dashpots), plastic elements (solid friction), or combinations of two or more elements. These elements can be either linear or nonlinear and can be combined to ensure the resulting physical behavior accurately represents the material's mechanical response.

As presented in Chapter 2, creep can be described as a viscoelastic behavior. Materials with that kind of behavior exhibit both instantaneous elastic deformation and delayed elastic deformation (viscoelastic strain) over time, as illustrated in Figure 2.3 in Section 2.3, where the viscoelastic strain represents the creep component.

4.4.1 Rheological Models for Viscoelastic Behavior

The rheological behavior of viscoelastic materials is commonly represented by mechanical models consisting of elastic and viscous elements, where the constitutive equation follows the general form of Eq. (4.21) (ARGYRIS; DOLTSINIS; SILVA, 1991). These elements can be represented as shown in Figure 4.2, where the relationships between stress and strain in a one-dimensional form can be expressed as

$$\begin{aligned} \sigma^e &= E\varepsilon && \text{for elastic elements,} \\ \sigma^v &= \eta\frac{\partial\varepsilon}{\partial t} = \eta\dot{\varepsilon} && \text{for viscous elements,} \end{aligned} \tag{4.22}$$

where E and η are the elastic modulus and viscosity coefficient, respectively.

Figure 4.2 – Representation of elastic and viscous elements.

(a) Elastic element. (b) Viscous element.

Adapted from Argyris, Doltsinis and Silva (1991).

These equations can also be extended to tensorial form, as demonstrated in Becho (2020), to account for three-dimensional effects and coupling phenomena.

Finally, these elements can be combined in different ways to represent viscoelastic material behavior. In such combinations, elements connected in series experience the same stress while their deformation adds up. On the other side, elements arranged in parallel share the same deformation, with the total stress being distributed among them.

The simplest and most commonly used models in the literature for describing viscoelastic behavior in solid materials include the Kelvin-Voigt Model, the Boltzmann Model, and the Zener Model. All of these models are derived from the generalized Maxwell and Kelvin-Voigt models (BECHO, 2020).

4.4.1.1 Maxwell Rheological Model

The Maxwell element consists of a series combination of an elastic element (spring) and a viscous element (dashpot) (Figure 4.3a). The generalized Maxwell model consists of a parallel assembly of multiple Maxwell elements, along with an additional spring to account for residual stress $\sigma = G(\varepsilon)$ (Figure 4.3b) (ARGYRIS; DOLTSINIS; SILVA, 1991).

Figure 4.3 – Maxwell models.

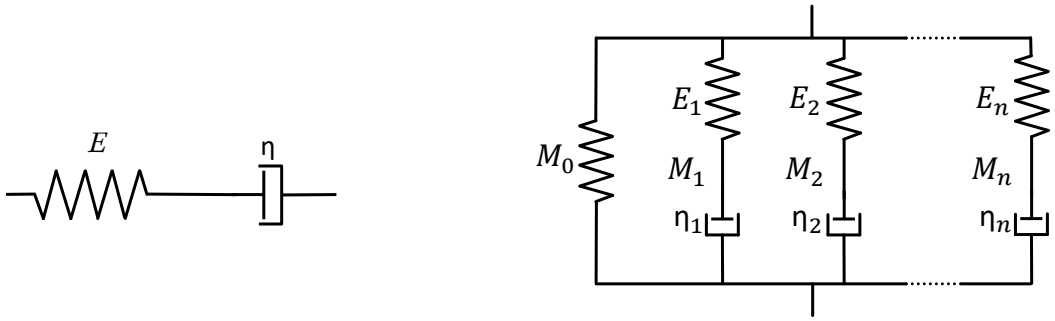

(a) Maxwell element. (b) Generalized Maxwell Model.

Adapted from Argyris, Doltsinis and Silva (1991).

The constitutive equation of the Maxwell Model is expressed by the differential equation

$$\dot{\varepsilon} = \frac{\sigma}{\eta} + \frac{\dot{\sigma}}{E}. \tag{4.23}$$

This equation indicates that the strain rate depends on the applied stress and its rate of change.

When a constant stress σ_0 is applied to the Maxwell Model, the differential equation simplifies to

$$\varepsilon(t) = \frac{\sigma_0}{E} + \frac{\sigma_0}{\eta}t. \tag{4.24}$$

In this model, the material undergoes an immediate elastic deformation given by σ_0/E. The strain increases linearly over time at a rate of σ_0/η, meaning there is no asymptotic deformation

limit. As a result, the Maxwell Model does not accurately represent the long-term creep behavior of concrete, as the strain grows indefinitely over time, as illustrated in Figure 4.4.

Figure 4.4 – Creep strain-time curve based on the Maxwell model.

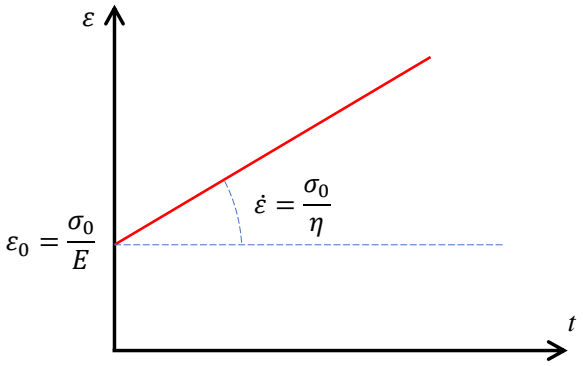

4.4.1.2 Kelvin-Voigt Rheological Model

In contrast, a parallel combination of an elastic and a viscous element consists of a Kelvin-Voigt solid (Figure 4.5a). The generalized Kelvin-Voigt model is composed of a series combination of multiple Kelvin-Voigt solids, along with an additional spring that provides time-independent elasticity $\varepsilon_e = \varepsilon_e(\sigma)$ (Figure 4.5b) (ARGYRIS; DOLTSINIS; SILVA, 1991).

Figure 4.5 – Kelvin-Voigt models.

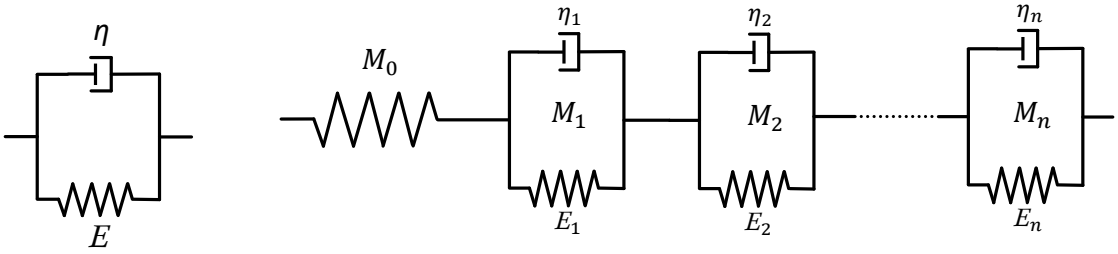

(a) Kelvin-Voigt solid. (b) Generalized Kelvin-Voigt Model.

Adapted from Argyris, Doltsinis and Silva (1991).

The constitutive equation of the Kelvin-Voigt model is described by the differential equation

$$\sigma = E\varepsilon + \eta\dot{\varepsilon}. \tag{4.25}$$

When a constant stress σ_0 is applied to the Kelvin-Voigt model, solving the differential equation leads to the expression governing the creep behavior of the model

$$\varepsilon(t) = \frac{\sigma_0}{E}\left(1 - e^{\frac{-E}{\eta}t}\right). \tag{4.26}$$

Differentiating Eq. (4.26) with respect to time yields the strain rate for the Kelvin-Voigt model

$$\dot{\varepsilon}(t) = \frac{\sigma_0}{\eta} e^{\frac{-E}{\eta}t}. \tag{4.27}$$

Thus, in this model, the material does not exhibit an immediate elastic deformation upon stress application. Over time, the strain increases asymptotically, as illustrated in Figure 4.6, approaching σ_0/E as t tends to infinity. This model accurately represents the creep behavior of concrete, as it describes a damped elastic response (viscoelastic behavior).

Figure 4.6 – Creep strain-time curve based on the Kelvin-Voigt model.

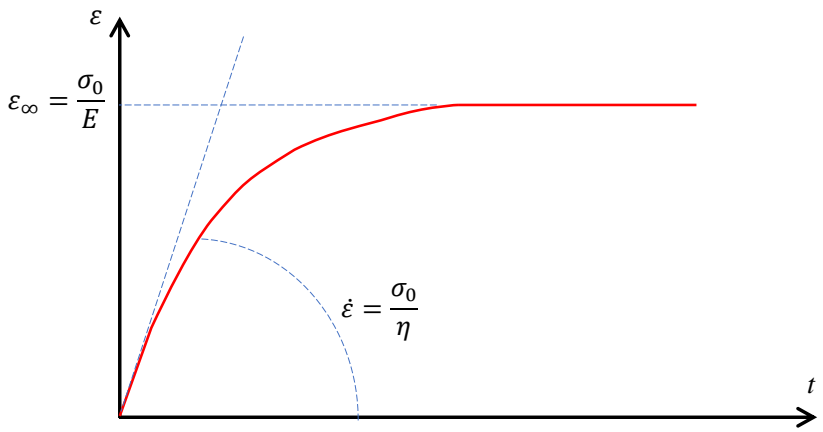

Adapted from Becho (2020).

4.4.1.3 Boltzmann Rheological Model

The Boltzmann rheological model can be represented as the series combination of a spring and a Kelvin-Voigt solid, as depicted in Figure 4.7. It describes an instantaneous elastic response followed by a damped elastic behavior (viscoelastic response) (BECHO, 2020). This model can be seen as a particular case of the generalized Kelvin-Voigt model, consisting of a single Kelvin-Voigt solid connected in series with a spring.

The constitutive equation of the Boltzmann Model is expressed by the differential equation

$$\sigma = \frac{E_1 E_2}{E_1 + E_2}\varepsilon + \frac{\eta E_1}{E_1 + E_2}\dot{\varepsilon} - \frac{\eta}{E_1 + E_2}\dot{\sigma}. \tag{4.28}$$

When a constant stress σ_0 is applied to the Boltzmann model, solving the differential equation leads to the expression governing the creep behavior of the model

Figure 4.7 – Boltzmann rheological model.

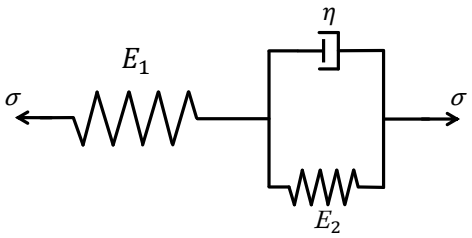

Adapted from Becho (2020).

$$\varepsilon(t) = \left(\frac{\sigma_0}{E_1} - \frac{E_1 + E_2}{E_2 E_1}\sigma_0\right) e^{\frac{-E_2}{\eta}t} + \frac{E_1 + E_2}{E_2 E_1}\sigma_0. \tag{4.29}$$

Differentiating Eq. (4.29) with respect to time yields the strain rate for the Boltzmann model

$$\dot{\varepsilon}(t) = \frac{\sigma_0}{\eta} e^{\frac{-E_2}{\eta}t} = \frac{E_1}{\eta}\varepsilon_0 e^{\frac{-E_2}{\eta}t}. \tag{4.30}$$

Thus, the material undergoes an immediate elastic deformation equal to σ_0/E_1 in this model. Over time, the deformation increases asymptotically, as illustrated in Figure 4.8, approaching $\sigma_0(E_1+E_2)/E_2E_1$ as t becomes sufficiently large.

Figure 4.8 – Creep strain-time curve based on the Boltzmann model.

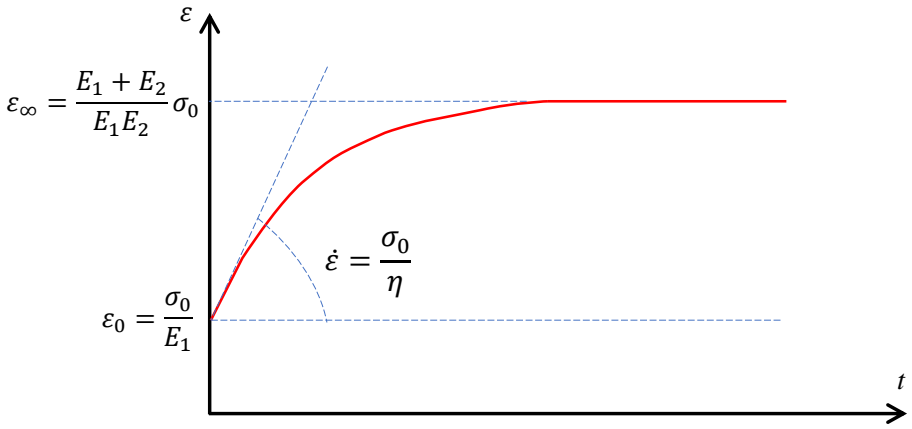

Adapted from Becho (2020).

This model can describe the entire strain-time behavior of concrete, including the instantaneous elastic strain upon load application and the viscoelastic strain due to creep.

4.4.1.4 Zener Rheological Model

Finally, the Zener rheological model can be represented as a parallel combination of a spring and a Maxwell element, as illustrated in Figure 4.9. Similar to the Boltzmann model, this model can describe an instantaneous elastic response followed by a damped elastic behavior (viscoelastic response) (BECHO, 2020). It can also be regarded as a particular case of the generalized Maxwell model, consisting of a single Maxwell element in parallel with a spring.

Figure 4.9 – Zener rheological model.

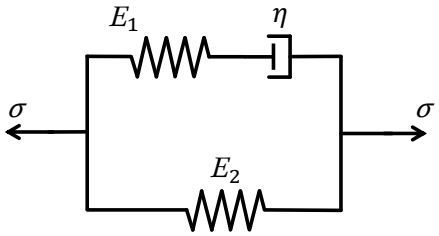

Adapted from Becho (2020).

The constitutive equation of the Zener model is expressed by the following differential equation

$$\sigma = E_2\varepsilon + \frac{\eta(E_1+E_2)}{E_1}\dot{\varepsilon} - \frac{\eta}{E_1}\dot{\sigma}. \tag{4.31}$$

When a constant stress σ_0 is applied to the Zener model, solving the differential equation leads to the expression governing the creep behavior of the model

$$\varepsilon(t) = \left(\frac{\sigma_0}{E_1+E_2} - \frac{\sigma_0}{E_2}\right) e^{\frac{-E_1E_2}{\eta(E_1+E_2)}t} + \frac{\sigma_0}{E_2}. \tag{4.32}$$

Differentiating Eq. (4.32) with respect to time yields the strain rate for the Zener model

$$\dot{\varepsilon}(t) = \frac{{E_1}^2\sigma_0}{\eta(E_1+E_2)^2} e^{\frac{-E_1E_2}{\eta(E_1+E_2)}t} = \frac{{E_1}^2}{\eta(E_1+E_2)}\varepsilon_0 e^{\frac{-E_1E_2}{\eta(E_1+E_2)}t}. \tag{4.33}$$

Thus, the material undergoes an immediate elastic deformation equal to $\sigma_0/(E_1+E_2)$ in this model. Over time, the strain increases asymptotically, as shown in Figure 4.10, approaching σ_0/E_2 as t becomes sufficiently large. Similarly to the Boltzmann model, this model can describe the entire strain-time behavior of concrete, including the instantaneous elastic strain upon load application and the viscoelastic strain due to creep.

Figure 4.10 – Creep strain-time curve based on the Zener model.

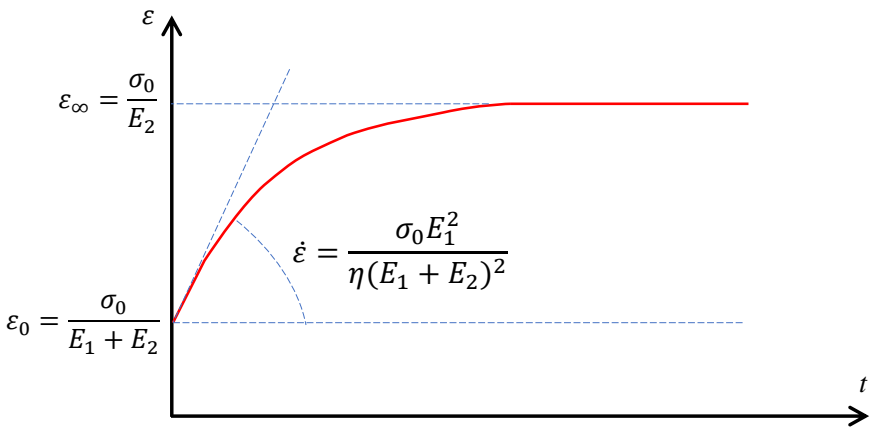

Adapted from Becho (2020).

4.4.2 Application of Rheological Models to Creep Simulation in Concrete

In this study, the elastic response of concrete was modeled using the idealized equation provided by NBR 6118 (2023), as expressed in Eq. (3.1), to ensure a nonlinear instantaneous response. To account for creep effects, the delayed response over time was incorporated using the Kelvin-Voigt model, represented by Eq. (4.26). This model was chosen because it accurately describes the creep behavior of concrete while excluding the instantaneous elastic response, which is already accounted for separately.

Similar to the Extended Stress-Strain Curve Method (Subsection 4.3), these rheological models for creep simulation can also be integrated into strategies for modeling local second-order effects in columns, as described in Subsection 3.3.

5 METHODOLOGY

Assessing second-order effects in reinforced concrete columns requires a robust computational methodology capable of incorporating material nonlinearities and time-dependent deformations. This study employs a numerical approach to simulate the structural behavior of columns subjected to axial force and bending moment, considering different strategies for creep modeling and second-order analysis.

To achieve this, a computational implementation was developed to apply established calculation methods in a systematic and automated manner, enabling the feasibility of using incremental iterative processes. The methodology is structured to ensure that both immediate and long-term responses of the structure are captured. Implementing iterative numerical procedures allows for a comparative evaluation of different modeling strategies, providing insights into their influence on design accuracy.

This chapter details the numerical formulation, implementation procedures, and methodologies adopted for second-order analysis and creep simulation.

5.1 CONSTRUCTION OF $M, N, 1/r$ DIAGRAMS

The construction of $M, N, 1/r$ diagrams represents a fundamental stage in applying the methodologies proposed in this study. These diagrams provide a numerical representation of the nonlinear behavior of reinforced concrete cross-sections subjected to a combined axial force (N) and bending moment (M), allowing material nonlinearity to be considered in the second-order analysis.

By capturing the moment-curvature relationship, the diagrams serve as input data for the subsequent methods used to evaluate second-order effects. This approach ensures that the physical nonlinearity of materials – particularly the nonlinear stress-strain relationship of concrete and steel – is incorporated into the structural response, enhancing the accuracy of the analysis.

The methodology presented here is based on the approach developed by Paula (1988). However, several modifications have been introduced to update the formulation in accordance with more recent versions of NBR 6118, including the 2023 revision. These updates ensure the numerical model remains aligned with the latest normative recommendations.

The developed algorithm determines the ultimate bending moment capacity of a given re-

inforced concrete section as a function of the curvature induced by bar deformations in the analyzed section for a fixed axial force value (PAULA, 1988).

5.1.1 Study of the Neutral Axis-Curvature Relationship

To begin the analysis, the plane cross-section hypothesis is assumed to be valid. This assumption states that plane cross-sections, initially flat before loading, remain plane until failure, leading to a linear strain distribution across the section. As a result, strains at any given point are directly proportional to their distance from the neutral axis.

Considering the validity of this hypothesis, the maximum permissible curvature of a reinforced concrete cross-section in its deformed configuration (as illustrated in Figure 5.1) can be expressed as

$$\frac{1}{r} = \frac{-\varepsilon_{cu} + \varepsilon_{su}}{d}, \tag{5.1}$$

which, in its dimensionless form, is given by

$$\frac{h}{r} = \frac{-\varepsilon_{cu} + \varepsilon_{su}}{d/h} \tag{5.2}$$

where d represents the distance from the most compressed edge to the centroid of the most tensioned reinforcement layer. This distance can be written in terms of the cross-section height h and the distance from the centroid of the reinforcement to the nearest edge d' as

$$d = h - d', \tag{5.3}$$

which, in its dimensionless form, is

$$\frac{d}{h} = 1 - \frac{d'}{h}. \tag{5.4}$$

Defining the dimensionless parameter

$$\delta = \frac{d'}{h} \tag{5.5}$$

and substituting it into Eq. (5.6), the curvature expression becomes

$$\frac{h}{r} = \frac{-\varepsilon_{cu} + \varepsilon_{su}}{1 - \delta}. \tag{5.6}$$

Figure 5.1 – Maximum allowable strains in a reinforced concrete section.

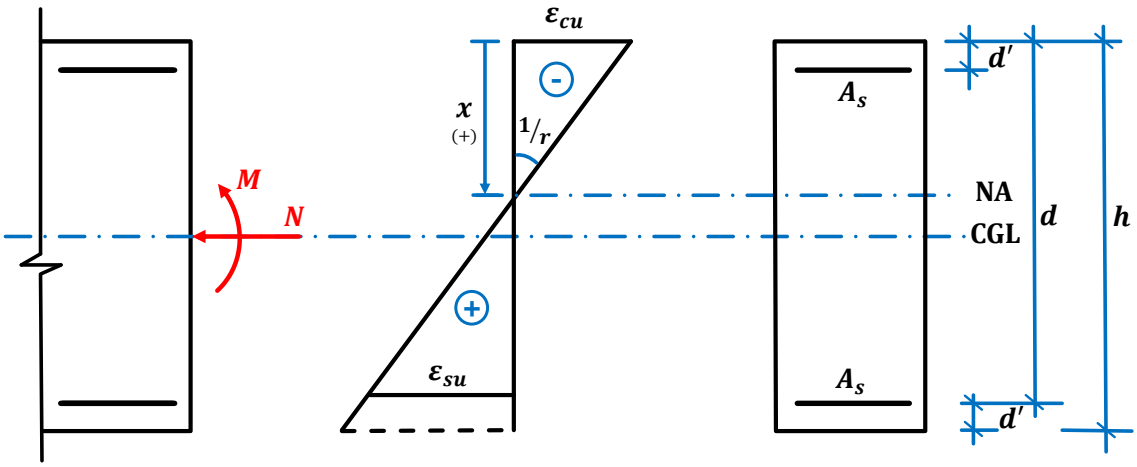

Adapted from Paula (1988).

In these equations, the value of the ultimate compressive strain of concrete ε_{cu} is considered negative (compression), while the value of the ultimate strain of steel ε_{su} is positive (tension).

To define a generic strain distribution for a cross-section, it is necessary – besides assuming a linear strain distribution – to adopt a curvature value that does not exceed the maximum limit established in Eq. (5.1). In this formulation, the neutral axis depth is represented by the dimensionless coefficient β_x, defined as

$$\beta_x = \frac{x}{h} \tag{5.7}$$

where β_x is assumed to vary within the range $]-\infty, +\infty[$, and x represents the neutral axis depth, measured as the distance from the most compressed fiber of the section to the neutral axis, as oriented in Figure 5.1.

5.1.2 Strain Compatibility

Figure 5.2 illustrates the strain distribution in a reinforced concrete cross-section, along with the coordinate system considered in this study.

Based on the strain compatibility condition, the following relationship holds:

Figure 5.2 – Generic strain diagram of a reinforced concrete section.

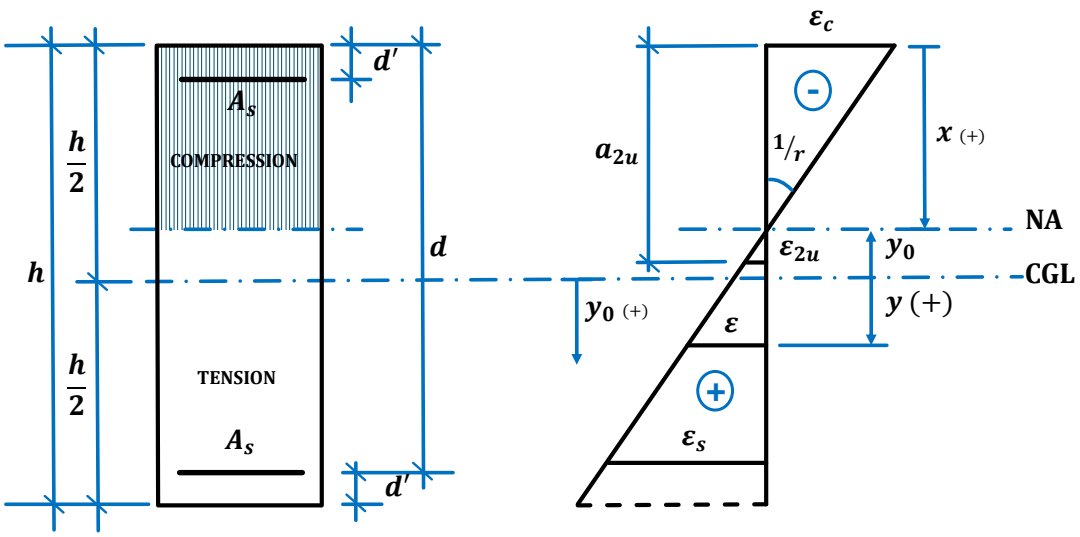

Adapted from Paula (1988).

$$\frac{-\varepsilon_c}{x} = \frac{\varepsilon}{y - y_0} = \frac{\varepsilon_s}{h - d' - x} = \frac{\varepsilon_{2u}}{a_{2u} - x} \tag{5.8}$$

where

- ε_c represents the specific strain at the most compressed edge of the concrete section;
- ε_s represents the specific strain in the tensioned reinforcement;
- ε represents the specific strain in a generic fiber located at a distance y from the section's centroid;
- y is the distance of a generic fiber from the centroid of the section;
- y_0 is the distance from the neutral axis to the centroid of the section; note that if the neutral axis is located above the centroid, y_0 assumes a negative value;
- ε_{2u} represents the specific strain at a concrete fiber located at a distance $a_{2u} = \frac{\varepsilon_{cu} - \varepsilon_{c2}}{\varepsilon_{cu}} h$ from the most compressed edge of the section.

The strain compatibility equation (5.8) allows expressing the strain ε at a generic fiber in terms of different reference strains:

1. In terms of the concrete strain

$$\varepsilon = -\frac{(y - y_0)}{x} \varepsilon_c; \tag{5.9}$$

2. In terms of the reinforcement strain

$$\varepsilon = \frac{(y - y_0)}{h - d' - x}\varepsilon_s; \tag{5.10}$$

3. In terms of the strain at the fiber located at a_{2u} from the most compressed edge

$$\varepsilon = \frac{(y - y_0)}{a_{2u} - x}\varepsilon_{2u}. \tag{5.11}$$

Additionally, by assuming small displacements, where $\tan(1/r) \cong 1/r$, the strains ε_{c2}, ε_s and ε_{2u} can be expressed as functions of the cross-section curvature $1/r$

$$\varepsilon_c = -x\frac{1}{r}, \tag{5.12}$$

$$\varepsilon_s = \frac{1}{r}(h - d' - x), \tag{5.13}$$

$$\varepsilon_{2u} = \frac{1}{r}(a_{2u} - x). \tag{5.14}$$

By substituting any of the expressions (5.12), (5.13), or (5.14) into (5.9), (5.10) or (5.11), respectively, the strain in a generic fiber ε can be expressed as a function of the curvature $1/r$

$$\varepsilon = \frac{1}{r}(y - y_0). \tag{5.15}$$

Considering Figure 5.2, the position of the centroidal axis relative to the neutral axis can be expressed as

$$y_0 = x - \frac{h}{2}. \tag{5.16}$$

By substituting Eq. (5.16) into Eq. (5.15) and using the dimensionless parameter β_x (Eq. (5.7)) as well as the dimensionless position of the generic fiber

$$\beta_y = \frac{y}{h}, \tag{5.17}$$

we obtain

$$\varepsilon = \frac{h}{r}\left(\beta_y + \frac{1}{2} - \beta_x\right). \tag{5.18}$$

Defining

$$\beta_0 = \beta_y + \frac{1}{2} \tag{5.19}$$

and substituting into Eq. (5.18), the final expression for the strain at a generic fiber is

$$\varepsilon = \frac{h}{r}\left(\beta_0 - \beta_x\right). \tag{5.20}$$

This equation allows strain computation at any fiber within the cross-section for a given curvature and neutral axis position.

5.1.3 Study of the Variation Range of the Parameter β_x

As previously discussed in Subsection 5.1.1, the variation range of the neutral axis depth parameter β_x theoretically extends from $-\infty$ to ∞. However, this range must be restricted to prevent the ultimate strain limits from being exceeded. This is achieved by defining admissible boundary values for β_x, as detailed in the following analysis.

Three distinct ranges are defined for β_x:

a) $\beta_x \leq 0$;
b) $0 < \beta_x \leq 1$;
c) $\beta_x > 1$.

Each of these cases is analyzed for a given cross-section curvature $1/r$.

a) Case $\beta_x \leq 0$ - Fully Tensioned Section
The entire section is in tension for $\beta_x \leq 0$. The lower limit of β_x is determined by the ultimate strain of the steel ε_{su}, as illustrated in Figure 5.3.
The position of the fiber that defines the strain limit condition for this case (the fiber of the most tensioned reinforcement) can be expressed in dimensionless form as

$$\beta_y = \frac{y}{h} = \frac{h/2 - d'}{h} = \frac{1}{2} - \delta. \tag{5.21}$$

By substituting this expression into Eq. (5.19), we obtain

Figure 5.3 – Strain distribution in a fully tensioned section.

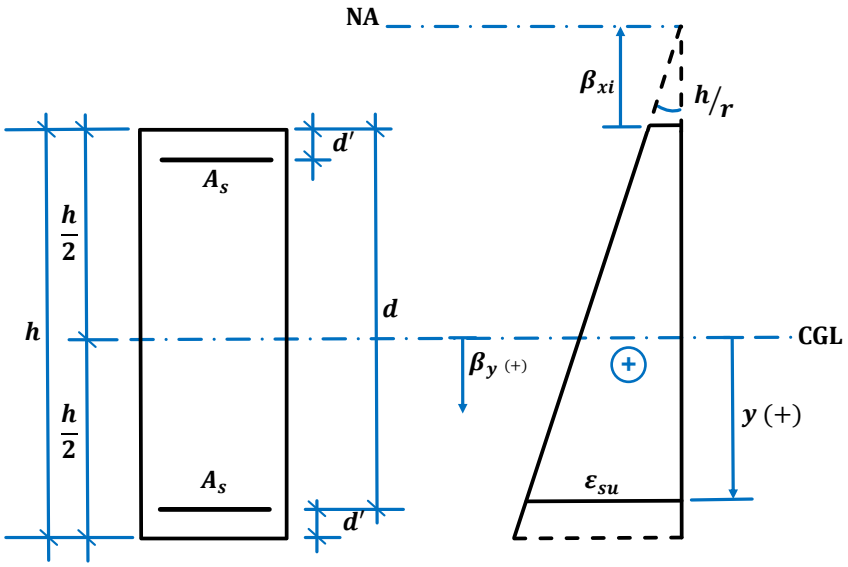

Adapted from Paula (1988).

$$\beta_0 = 1 - \delta. \tag{5.22}$$

To ensure that the ultimate strain limit of the steel is not exceeded, the expression defining the strain of a generic fiber within the section, given by Eq. (5.20), must satisfy the inequality

$$\varepsilon = \frac{h}{r}(\beta_0 - \beta_x) \leq \varepsilon_{su}. \tag{5.23}$$

Substituting Eq. (5.22) into Eq. (5.23), the lower limit of the variation range for β_x, denoted as β_{xi}, is obtained as

$$\beta_{xi} = 1 - \delta - \frac{\varepsilon_{su}}{h/r}. \tag{5.24}$$

b) Case $0 < \beta_x \leq 1$ - Partially Compressed Section

For $0 < \beta_x \leq 1$, an upper limit for β_x is defined based on the ultimate compressive strain in the concrete fiber located at the most compressed edge, given by $\varepsilon_c = \varepsilon_{cu}$, as illustrated in Figure 5.4. Since the section is partially compressed, this condition ensures that the strain distribution remains within the permissible deformation limits.

The position of the fiber that defines the strain limit condition, $\varepsilon_c = \varepsilon_{cu}$, is given by the dimensionless parameter

$$\beta_y = -\frac{1}{2}. \tag{5.25}$$

Substituting this expression into Eq. (5.19) results in

Figure 5.4 – Strain distribution in a partially compressed section.

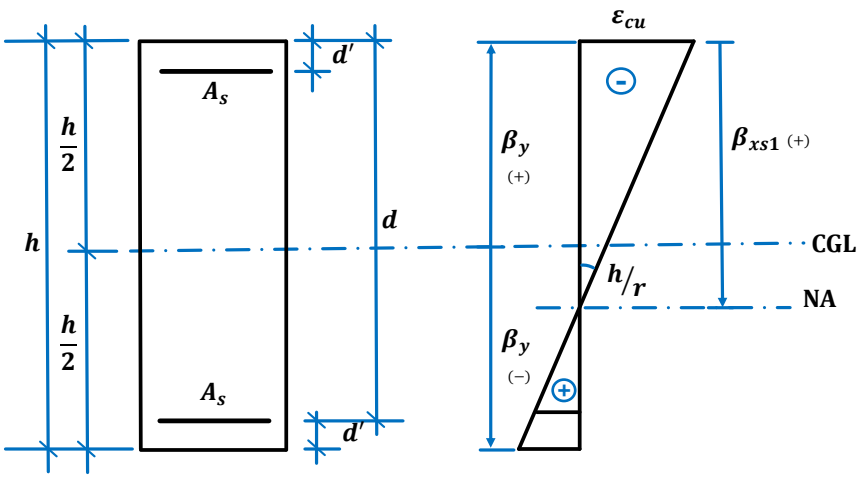

Adapted from Paula (1988).

$$\beta_0 = 0. \tag{5.26}$$

To ensure that the ultimate compressive strain limit in the most compressed concrete fiber does not exceed $\varepsilon_c = \varepsilon_{cu}$, the strain expression must satisfy the inequality

$$\varepsilon = \frac{h}{r}(\beta_0 - \beta_x) \geq \varepsilon_{cu}. \tag{5.27}$$

By substituting Eq. (5.26) into Eq. (5.27), the first upper limit of the variation range for β_x, denoted here as β_{xs1}, is obtained as

$$\beta_{xs1} = \frac{-\varepsilon_{cu}}{h/r} \tag{5.28}$$

c) Case $\beta_x > 1$ - Fully Compressed Section

For $\beta_x > 1$, a second upper limit for β_x arises, which is determined by the ultimate compressive strain in the concrete fiber located at a distance a_{2u} from the most compressed edge. This strain, denoted as $\varepsilon_{2u} = \varepsilon_{c2}$, establishes an additional constraint to ensure that the section remains within the permissible deformation limits, as illustrated in Figure 5.5. The position of this critical fiber within the cross-section is given by

$$\beta_y = \frac{\varepsilon_{cu} - 2\varepsilon_{c2}}{2\varepsilon_{cu}}. \tag{5.29}$$

By substituting this expression into Eq. (5.19), we obtain

$$\beta_0 = 1 - \frac{\varepsilon_{c2}}{\varepsilon_{cu}}. \tag{5.30}$$

To satisfy the compressive strain condition, the expression governing the strain of a generic fiber, given by (5.20), must adhere to the inequality

Figure 5.5 – Strain distribution in a fully compressed section.

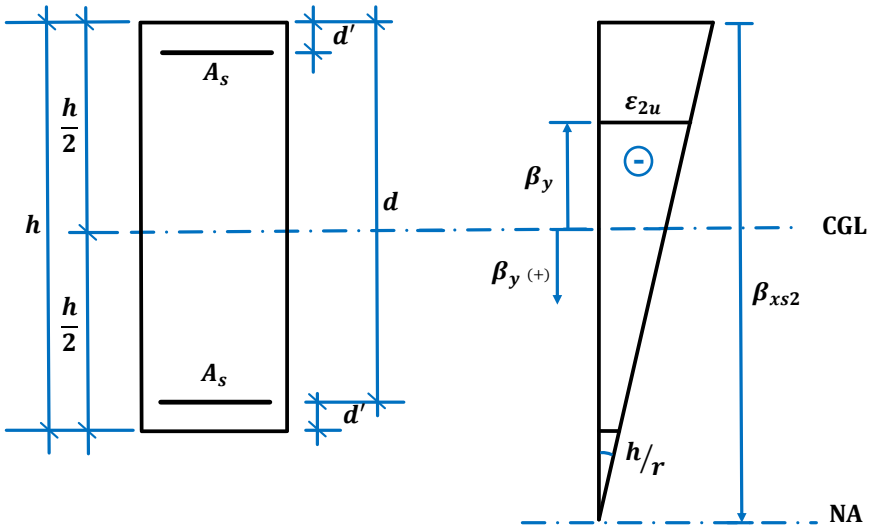

Adapted from Paula (1988).

$$\varepsilon = \frac{h}{r}(\beta_0 - \beta_x) \geq \varepsilon_{c2}. \tag{5.31}$$

By substituting Eq. (5.30) into Eq. (5.31), the second upper limit for the variation of β_x, denoted here as β_{xs2}, is given by

$$\beta_{xs2} = \frac{-\varepsilon_{c2}}{h/r} + \frac{a_{2u}}{h} = \frac{-\varepsilon_{c2}}{h/r} + 1 - \frac{\varepsilon_{c2}}{\varepsilon_{cu}}. \tag{5.32}$$

From the analysis performed, it can be concluded that the choice of Eq. (5.28) or Eq. (5.32) to determine the upper limit of the parameter β_x, denoted as β_{xs}, depends on which compressive strain limit is reached first.

5.1.4 Equilibrium Equations – Rectangular section

Assuming the validity of the plane cross-section hypothesis, assigning a value to the curvature $1/r$, and defining the neutral axis depth through the dimensionless parameter β_x within limits discussed in Subsection 5.1.3, the strain at any generic fiber within the cross-section of a reinforced concrete member can be computed using Eq. (5.20). Consequently, the distribution of resisting stress can be determined by applying the stress-strain relationships presented in Section 3.1. From the calculated stress values, the resisting internal forces of the cross-section can be determined and subsequently used in the equilibrium equations.

For a rectangular cross-section with the neutral axis perpendicular to the symmetry plane of the member, considering combined axial force and bending moment, the resisting axial force (N_R) and the resisting bending moment (M_R) can be expressed as

$$N_R = R_{cc} + \sum_{\mathrm{i}=1}^{\mathrm{n}} R_{si}, \tag{5.33}$$

$$M_R = M_{cc} + \sum_{\mathrm{i}=1}^{\mathrm{n}} R_{si} y_{si}, \tag{5.34}$$

where n is the number of reinforcement bars, and R_{cc} and M_{cc} are the resultants of the stresses in the compressed concrete section associated with the axial force and bending moment, respectively

$$R_{cc} = \int_{A_c} \sigma_c \, dA, \tag{5.35}$$

$$M_{cc} = \int_{A_c} y \sigma_c \, dA. \tag{5.36}$$

Considering the stresses in the reinforcement (σ_{si}) and the cross-sectional area of each reinforcement bar (A_{si}), the resultant of the stresses in the reinforcement can be expressed using summations

$$\sum_{\mathrm{i}=1}^{\mathrm{n}} R_{si} = \sum_{\mathrm{i}=1}^{\mathrm{n}} \sigma_{si} A_{si}, \tag{5.37}$$

$$\sum_{\mathrm{i}=1}^{\mathrm{n}} R_{si} y_{si} = \sum_{\mathrm{i}=1}^{\mathrm{n}} y_{si} \sigma_{si} A_{si}. \tag{5.38}$$

Substituting these into the equilibrium equations yields

$$N_R = R_{cc} + \sum_{\mathrm{i}=1}^{\mathrm{n}} \sigma_{si} A_{si}, \tag{5.39}$$

$$M_R = M_{cc} + \sum_{\mathrm{i}=1}^{\mathrm{n}} y_{si} \sigma_{si} A_{si}. \tag{5.40}$$

Expressing the area integrals as functions of the variable y allows rewriting the above equations as

$$N_R = \int_{-h/2}^{y_0} b_w \sigma_c \, dy + \sum_{\mathrm{i}=1}^{\mathrm{n}} \sigma_{si} A_{si}, \tag{5.41}$$

$$M_R = \int_{-h/2}^{y_0} b_w y \sigma_c \, dy + \sum_{\mathrm{i}=1}^{\mathrm{n}} y_{si} \sigma_{si} A_{si}. \tag{5.42}$$

These expressions allow for evaluating the internal resisting axial force (N_R) and bending moment (M_R) in a reinforced concrete section with defined geometry and material properties.

5.1.5 Dimensionless Equilibrium Equations

To simplify the computation of the integrals presented in Eqs. (5.41) and (5.42), they are divided into two components. In this analysis, the stress distribution in concrete is considered according to the idealized stress-strain diagram, as illustrated in Figure 3.1. These integrals are separated as follows:

- The first component, with integration limits y_1 and y_2, corresponds to the rectangular portion of the stress-strain diagram;
- The second component, with integration limits y_2 and y_3, corresponds to the curved portion of the diagram.

The integration limits are illustrated in Figure 5.6. These equilibrium equations are obtained by substituting σ_c with the corresponding expression in Eq. (3.1). Following this procedure, the resisting axial force (N_R) and resisting bending moment (M_R) are given by

$$N_R = -\int_{y_1}^{y_2} 0.85 \eta_c f_{cd} b_w dy - 0.85 \eta_c f_{cd} b_w \int_{y_2}^{y_3} \left[1 - \left(1 - \frac{\varepsilon_c}{\varepsilon_{c2}} \right)^n \right] dy + \sum_{\mathrm{i}=1}^{\mathrm{n}} \sigma_{si} A_{si}, \tag{5.43}$$

$$M_R = -\int_{y_1}^{y_2} 0.85 \eta_c f_{cd} b_w y dy - 0.85 \eta_c f_{cd} b_w \int_{y_2}^{y_3} \left[1 - \left(1 - \frac{\varepsilon_c}{\varepsilon_{c2}} \right)^n \right] y dy + \sum_{\mathrm{i}=1}^{\mathrm{n}} y_i \sigma_{si} A_{si}. \tag{5.44}$$

It is convenient to express the above equations independently of the cross-section dimensions h and b_w, and the design stress f_{cd} to facilitate the study of reinforced concrete sections. This is achieved by defining the dimensionless calculation limits, obtained using Eq. (5.17), and by introducing dimensionless resisting axial force (ν_R) and dimensionless resisting bending moment (μ_R), given by

Figure 5.6 – Stress distribution in partially compressed concrete.

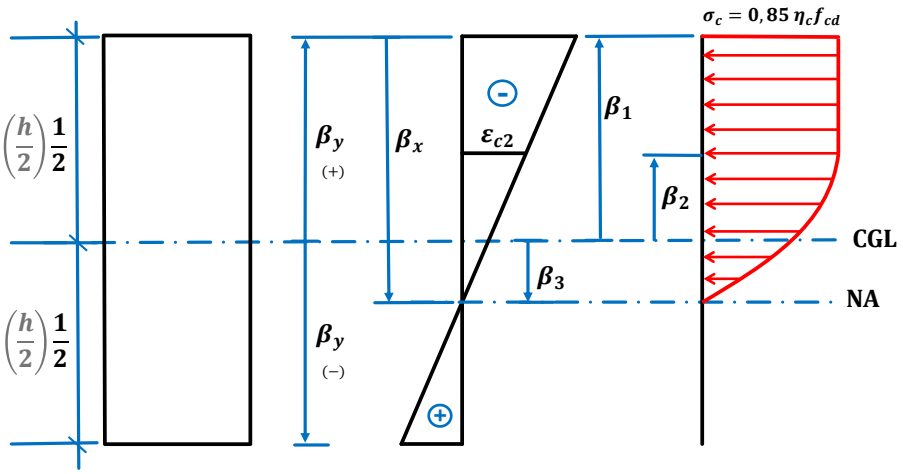

Adapted from Paula (1988).

$$\nu_R = \frac{N_R}{b_w h f_{cd}}, \tag{5.45}$$

$$\mu_R = \frac{M_R}{b_w h^2 f_{cd}}. \tag{5.46}$$

5.1.5.1 Derivation of the Dimensionless Resisting Axial Force Expression

Dividing Eq. (5.43) by $b_w h f_{cd}$ and substituting the integration limits y_1, y_2 and y_3 with their respective dimensionless counterparts β_1, β_2 and β_3, calculated using Eq. (5.17), while setting $dy/h = d\beta_y$, results in

$$\nu_R = -0.85\eta_c \int_{\beta_1}^{\beta_2} d\beta_y - 0.85\eta_c \int_{\beta_2}^{\beta_3} \left[1 - \left(1 - \frac{\varepsilon_c}{\varepsilon_{c2}}\right)^n\right] d\beta_y + \frac{1}{b_w h f_{cd}} \sum_{i=1}^{n} \sigma_{si} A_{si}. \tag{5.47}$$

By substituting ε_c using the compatibility equation (5.18), the expression takes the form

$$\nu_R = -0.85\eta_c \int_{\beta_1}^{\beta_2} d\beta_y - 0.85\eta_c \int_{\beta_2}^{\beta_3} \left[1 - \left(1 - \frac{h}{r}\frac{(\beta_y - \beta_x + 1/2)}{\varepsilon_{c2}}\right)^n\right] d\beta_y + \\ + \frac{\omega}{f_{yd}} \sum_{i=1}^{n} \sigma_{si} n_{si}. \tag{5.48}$$

where ω is the mechanical reinforcement ratio given by

$$\omega = \frac{f_{yd} A_s}{f_{cd} A_c}; \tag{5.49}$$

and n_{si} is defined as the ratio between the area of a single reinforcement bar and the total reinforcement area, given by

$$n_{si} = \frac{A_{si}}{A_s}. \tag{5.50}$$

The definite integral presented above was solved analytically by performing the arithmetic operations, integration, and limit evaluation. The analytical solution, which allows for the calculation of the resisting axial force in a reinforced concrete section in dimensionless terms for a given curvature and neutral axis depth, was directly implemented in the Java-based computational program.

5.1.5.2 Derivation of the Dimensionless Resisting Bending Moment Expression

Dividing Eq. (5.44) by $b_w h^2 f_{cd}$ and substituting the integration limits y_1, y_2 and y_3 with their respective dimensionless counterparts β_1, β_2 and β_3, calculated using Eq. (5.17), results in

$$\mu_R = -0.85\eta_c \int_{\beta_1}^{\beta_2} \beta_y d\beta_y - 0.85\eta_c \int_{\beta_2}^{\beta_3} \left[1 - \left(1 - \frac{\varepsilon_c}{\varepsilon_{c2}}\right)^n\right] \beta_y d\beta_y + \\ + \frac{1}{b_w h^2 f_{cd}} \sum_{\mathrm{i}=1}^{\mathrm{n}} y_i \sigma_{si} A_{si}. \tag{5.51}$$

By substituting ε_c using the compatibility equation (5.18), the expression takes the form

$$\mu_R = -0.85\eta_c \int_{\beta_1}^{\beta_2} \beta_y d\beta_y - 0.85\eta_c \int_{\beta_2}^{\beta_3} \left[1 - \left(1 - \frac{h}{r}\frac{(\beta_y - \beta_x + 1/2)}{\varepsilon_{c2}}\right)^n\right] \beta_y d\beta_y + \\ + \frac{\omega}{f_{yd}} \sum_{\mathrm{i}=1}^{\mathrm{n}} \sigma_{si} \beta_{si} n_{si}. \tag{5.52}$$

Similarly, the definite integral was solved analytically, performing arithmetic operations, integration, and limit evaluation. The analytical solution for computing the dimensionless resisting bending moment in a reinforced concrete section for a given curvature and neutral axis depth was directly implemented in the Java-based computational program.

5.1.5.3 Definition of Dimensionless Integration Limits

Considering the variation intervals of the parameter β_x defined in Subsection 5.1.3, the dimensionless integration limits β_1, β_2, and β_3 are now analyzed, as shown in Figure 5.6.

To determine the dimensionless values of the ordinates that define the integration limits, the starting point of the rectangular stress distribution phase in the diagram is established as

$$\beta_1 = -\frac{1}{2}. \tag{5.53}$$

Additionally, compressive stresses in concrete remain uniformly distributed until the fiber located at a distance a_{2u} from the most compressed edge reaches the strain ε_{c2}. Therefore, the maximum permissible ordinate y_2, which marks the end of the rectangular compression stress distribution in concrete, is given by

$$y_{2s} = y_1 + a_{2u}. \tag{5.54}$$

Since $y_1 = -h/2$ and $a_{2u} = \frac{\varepsilon_{cu}-\varepsilon_{c2}}{\varepsilon_{cu}}h$, it follows that

$$y_{2s} = -\frac{h}{2} + \frac{\varepsilon_{cu}-\varepsilon_{c2}}{\varepsilon_{cu}}h. \tag{5.55}$$

In dimensionless form, this expression becomes

$$\beta_{2s} = -\frac{1}{2} + \frac{\varepsilon_{cu}-\varepsilon_{c2}}{\varepsilon_{cu}}. \tag{5.56}$$

Since only the integral within the section is relevant, the minimum permissible value for the dimensionless ordinate β_2 is defined as

$$\beta_{2i} = -\frac{1}{2}. \tag{5.57}$$

Thus, the dimensionless parameter β_2 varies within the range

$$-\frac{1}{2} \leq \beta_2 \leq -\frac{1}{2} + \frac{\varepsilon_{cu}-\varepsilon_{c2}}{\varepsilon_{cu}}. \tag{5.58}$$

The value of β_2 can be computed using the expression

$$\beta_2 = \frac{\varepsilon_{c2}}{h/r} + \beta_x - \frac{1}{2}, \tag{5.59}$$

which is derived by imposing $\varepsilon = \varepsilon_{c2}$ in Eq. (5.18). It is important to emphasize that the values of β_2 obtained using this equation must respect the limits defined in Eq. (5.58).

The third integration limit, β_3, which defines the end of the stress distribution diagram, corresponds to the position of the fiber with zero strain. Therefore, to obtain a general expression for this limit, it is sufficient to impose zero strain in the compatibility equation (5.18), leading to

$$\beta_3 = \beta_x - \frac{1}{2}, \tag{5.60}$$

where the minimum allowable value is

$$\beta_{3i} = -\frac{1}{2}. \tag{5.61}$$

For $\beta_x > 1$ (fully compressed section), the dimensionless limit β_3 exceeds the section boundaries. However, since only the integral within the section is relevant, the maximum permissible variation of the integration limit is set as

$$\beta_{3s} = 1/2. \tag{5.62}$$

For $\beta_x \leq 0$ (fully tensioned section), the dimensionless integration limits must nullify the stress integral in the concrete section since the concrete tensile strength is not considered. This is easily achieved by assigning the minimum values to the integration limits β_1, β_2 and β_3. As a result, the resisting axial force is provided solely by the reinforcement in the cross-section.

5.1.6 Algorithm for Computing the Bending Moment-Axial Force-Curvature Diagram $(\mu, \nu, h/r)$

The computation of the bending moment-axial force-curvature diagram for a given reinforced concrete section subjected to a prescribed axial force requires determining, for each assigned curvature $1/r$, the neutral axis depth that generates an internal dimensionless axial force ν_R equal (or approximately equal) to the prescribed design dimensionless axial force ν_{fix}

$$\nu_{\text{fix}} = \nu_R. \tag{5.63}$$

One way to solve this problem is by applying an iterative numerical method for solving nonlinear equations, where the objective is to determine the dimensionless neutral axis depth β_x that satisfies the equilibrium condition. In this study, the *False Position Method* was chosen due to its ease of implementation, guaranteed convergence when the function is continuous within an interval $[a,b]$ satisfying $f(a)f(b) < 0$, and faster convergence compared to the Bisection Method (RUGGIERO; LOPES, 1996).

Once the neutral axis depth β_x is determined, the dimensionless internal bending moment μ_R is computed.

Given a fixed design dimensionless axial force ν_{fix}, the following steps outline the procedure for constructing the diagram:

1. Define the Curvature Increment
   For iteration i with an incremental dimensionless curvature step Δ_i, compute the dimensionless curvature of the section as

$$(h/r)_i = (h/r)_{i-1} + \Delta_i. \tag{5.64}$$

2. Establish the Neutral Axis Depth Interval
   Define the lower and upper limits for the neutral axis depth (β_x) based on the analysis in Subsection 5.1.3.
   2.1 Lower limit of β_x
   The lower limit of β_x is given by

$$\beta_{xi} = 1 - \delta - \frac{\varepsilon_{su}}{h/r} \tag{5.24}$$

   where $\delta = \frac{d'}{h}$.
   2.2 Upper limit of β_x
   The upper limit is initially given by

$$\beta_{xs1} = \frac{-\varepsilon_{cu}}{h/r}. \tag{5.28}$$

   If this expression returns a value greater than 1, the upper limit of β_x is adjusted using

$$\beta_{xs2} = \frac{-\varepsilon_{c2}}{h/r} + 1 - \frac{\varepsilon_{c2}}{\varepsilon_{cu}}. \tag{5.32}$$

3. Compute the Resisting Axial Forces ν_1 and ν_2
   Compute the dimensionless internal axial forces, ν_1 and ν_2, corresponding to the lower and upper limits of β_x using the analytical solution of Eq (5.48).
4. Verify if ν_{fix} Lies Within the Interval ($\nu_1 < \nu_{\text{fix}} < \nu_2$)
   Using the equilibrium equation

$$\nu_{\text{fix}} = \nu_R \tag{5.63}$$

   the function

$$f(\beta_x) = \nu_{\text{fix}} - \nu_R(\beta_x) \tag{5.65}$$

   was defined, which equals zero when equilibrium is reached.
   For ν_{fix} to be within the interval, the following condition must hold

$$f(\beta_{xi}) \cdot f(\beta_{xs}) < 0. \tag{5.66}$$

   If $f(\beta_{xi}) \cdot f(\beta_{xs}) > 0$, equilibrium is impossible, as the resistance limits are exceeded. In this case, equilibrium cannot be achieved for any value of β_x at this curvature, and the procedure moves to the next curvature increment (return to Step 1).
5. Apply the False Position Method
   Solve for β_x using the False Position Method to determine the neutral axis depth that satisfies equilibrium ($f(\beta_x) = 0$ in Eq. (5.65)).
6. Compute the Dimensionless Resisting Bending Moment μ_R
   Calculate μ_R using the analytical solution of Eq. (5.52).
7. Store Results and Iterate for Next Curvature Value
   Store the bending moment value for the current curvature step and return to Step 1 for the next curvature increment $(h/r)_i$.

In this study, the diagram is constructed twice. The first instance is carried out for the ultimate strength of concrete σ_{cd} set as $0.85\eta_c f_{cd}$ to determine the resisting moment M_{Rd} corresponding to the axial force N_{Rd}. This configuration represents the condition in which the strains in either the steel or concrete reach their limit values (dashed curve in Figure 3.6) (CASAGRANDE, 2016).

The second curve is constructed for the safety formulation presented by NBR 6118 (2023), with $\sigma_{cd} = 1.1 f_{cd}$ and N_{Rd}/γ_{f3}. This curve is used in the application of the General Method to obtain point B, as illustrated in Figure 3.6. From this point, the secant stiffness $(EI)_{\text{sec}}$ corresponding to the slope of line AB is determined, and its dimensionless representation κ_{sec} is computed for application in the Standard Column Method.

For the program to construct the $M,N,1/r$ diagrams, the following input data are required: the concrete strength, the steel strength, the cross-section dimensions including the areas and positions of the reinforcement layers, and the design axial force N_d for which the diagram is to be generated.

5.1.7 $M,N,1/r$ Diagrams Using the New Stress-Strain Diagram for Nonlinear Analysis introduced in NBR 6118 (2023)

EN 1992-1-1 (2004) and the new version of NBR 6118 (2023) recommend the use of the stress-strain diagram for nonlinear analysis, as described by Eq. (3.7) and illustrated in Figure 3.2, in the application of the General Method. To apply this approach, it is necessary to construct $M,N,1/r$ diagrams using this stress-strain relationship for nonlinear analysis.

The algorithm for constructing these $M,N,1/r$ diagrams follows the same steps as previously described, with the only difference being the expressions used to compute the resisting axial forces and bending moments in dimensionless form, particularly regarding the calculation of the resultant compressive force in the concrete.

To adapt the stress-strain formulation, the stress σ_c is isolated in Eq. (3.7)

$$\frac{\sigma_c}{f_{cm}} = \frac{k\eta - \eta^2}{1+(k-2)\eta} \tag{3.7}$$

where η is expressed as

$$\eta = \frac{\varepsilon_c}{\varepsilon_{c1}}. \tag{5.67}$$

Substituting Eq. (5.67) into Eq. (3.7) results in

$$\sigma_c = f_{cm}\varepsilon_c \left[\frac{(k\varepsilon_{c1} - \varepsilon_c)}{\varepsilon_c\varepsilon_{c1}k + {\varepsilon_{c1}}^2 - 2\varepsilon_c\varepsilon_{c1}}\right]. \tag{5.68}$$

The equilibrium equations, initially described in Eqs. (5.43) and (5.44), are reformulated for the new stress-strain diagram as follows

$$N_R = -b_w f_{cm}\int_{y_1}^{y_3} f_{cm}\varepsilon_c \left[\frac{(k\varepsilon_{c1} - \varepsilon_c)}{\varepsilon_c\varepsilon_{c1}k + {\varepsilon_{c1}}^2 - 2\varepsilon_c\varepsilon_{c1}}\right] dy + \sum_{\mathrm{i}=1}^{\mathrm{n}} \sigma_{si}A_{si} \tag{5.69}$$

$$M_R = -b_w f_{cm} \int_{y_1}^{y_3} f_{cm}\varepsilon_c \left[\frac{(k\varepsilon_{c1} - \varepsilon_c)}{\varepsilon_c \varepsilon_{c1} k + {\varepsilon_{c1}}^2 - 2\varepsilon_c \varepsilon_{c1}} \right] y dy + \sum_{\mathrm{i}=1}^{\mathrm{n}} y_i \sigma_{si} A_{si} \tag{5.70}$$

Expressing these equations in dimensionless form by dividing Eq. (5.69) by $b_w h f_{cd}$ and Eq. (5.70) by $b_w h^2 f_{cd}$, and substituting ε_c using the compatibility equation (5.18), results in

$$\nu_R = -\frac{fcm}{fcd} \int_{\beta_1}^{\beta_3} \frac{h}{r} \left(\beta_y - \beta_x + \frac{1}{2} \right) \left\{ \frac{\left[k\varepsilon_{c1} - \frac{h}{r} \left(\beta_y - \beta_x + \frac{1}{2} \right) \right]}{\left[\frac{h}{r} \left(\beta_y - \beta_x + \frac{1}{2} \right) \varepsilon_{c1} k + {\varepsilon_{c1}}^2 - 2\frac{h}{r} \left(\beta_y - \beta_x + \frac{1}{2} \right) \varepsilon_{c1} \right]} \right\} d\beta_y + \\ + \frac{\omega}{f_{yd}} \sum_{\mathrm{i}=1}^{\mathrm{n}} \sigma_{si} n_{si}. \tag{5.71}$$

$$\mu_R = -\frac{fcm}{fcd} \int_{\beta_1}^{\beta_3} \frac{h}{r} \left(\beta_y - \beta_x + \frac{1}{2} \right) \left\{ \frac{\left[k\varepsilon_{c1} - \frac{h}{r} \left(\beta_y - \beta_x + \frac{1}{2} \right) \right]}{\left[\frac{h}{r} \left(\beta_y - \beta_x + \frac{1}{2} \right) \varepsilon_{c1} k + {\varepsilon_{c1}}^2 - 2\frac{h}{r} \left(\beta_y - \beta_x + \frac{1}{2} \right) \varepsilon_{c1} \right]} \right\} \beta_y d\beta_y + \\ + \frac{\omega}{f_{yd}} \sum_{\mathrm{i}=1}^{\mathrm{n}} \sigma_{si} \beta_{si} n_{si}. \tag{5.72}$$

The integrals for the idealized stress-strain diagram presented in Eqs. (5.48) and (5.52) were solved analytically, and their results were implemented. However, these integrals in Eqs. (5.71) and (5.72) become particularly complex in this case, making an analytical solution impractical.

To address this, numerical integration using Simpson's Rule was employed through the Apache Commons Math Library, implemented in Java.

Thus, the procedure for constructing $M, N, 1/r$ diagrams using this nonlinear stress-strain diagram follows the same methodology described in Subsection 5.1.6, with the only modification being the substitution of the expressions used for computing the dimensionless resisting axial forces ν_R and bending moments μ_R with the numerical integration results from Eqs. (5.71) and (5.72).

5.2 METHODS FOR SECOND-ORDER ANALYSIS

This section presents the methodology implemented in the Java-based computational program for evaluating second-order effects in reinforced concrete columns. The approach is based on the theoretical concepts introduced in Section 3.3 and focuses on two numerical strategies: the *Standard Column Method* and the *General Method*, both coupled with $M, N, 1/r$ diagrams. The following subsections detail the formulation and computational procedures for each method.

5.2.1 Standard Column Method Coupled with $M,N,1/r$ Diagrams

Implementing the Standard Column Method consists primarily of directly applying the equations presented in Section 3.3.

To compute the maximum total internal moment, which includes second-order effects, the following expression is used

$$M_{d,tot} = \frac{\alpha_b M_{1d,A}}{1 - \dfrac{\lambda^2}{120\kappa/\nu}} \geq M_{1d,A}. \tag{3.36}$$

In this case, the dimensionless secant stiffness κ_{sec} is extracted from the $M,N,1/r$ diagram, as illustrated in Figure 3.6. In the computational implementation, the moment and curvature coordinates of the cross-section at Point B are stored during the construction of the diagram. Since the program is formulated in its dimensionless form, the dimensionless secant stiffness is directly obtained by the ratio

$$\kappa_{\text{sec}} = \frac{(\mu_{Rd}/\gamma_{f3})}{(h/r)_B} \tag{5.73}$$

where $(h/r)_B$ represents the dimensionless curvature value corresponding to the moment μ_{Rd}/γ_{f3}.

For consistency, since the safety formulation is applied in constructing the $M,N,1/r$ diagram to obtain the secant stiffness, the design axial force and moment values used in Eq. (3.36) should also be divided by γ_{f3}.

5.2.2 General Method Coupled with $M,N,1/r$ Diagrams

In the General Method, various strategies are found in the literature. The two most commonly adopted approaches are the *Finite Difference Method* and *Mohr's Analogy*, although the *Finite Element Method* can also be applied. In this study, the Finite Difference Method was chosen due to its simplicity of implementation.

The methodology presented here is based on the approach presented by Araújo (1993), adapted for a bi-supported column subjected to axial loading without the application of transverse loads along its height. The algorithm combines incremental and iterative processes, which enable considering nonlinear effects.

5.2.2.1 Equilibrium Equations

This section presents the equilibrium equations for the column illustrated in Figure 5.7, subjected to an axial force P and bending moments M_a and M_b at its ends. The axial force P is assumed to be constant along the column's axis.

Figure 5.7 – Deformed axis of the column.

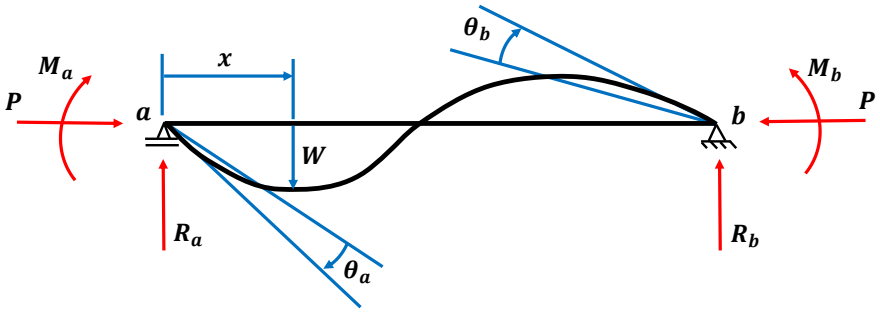

Adapted from Araújo (1993).

Upon the application of loads, the column experiences an incremental transverse displacement $W(x)$ as illustrated in Figure 5.7, where the positive directions for rotations and transverse displacements are also indicated.

Ensuring moment equilibrium with respect to end b results in

$$R_a l + M_a - M_b = 0, \tag{5.74}$$

from which the reaction force R_a is obtained as

$$R_a = \frac{(M_b - M_a)}{l}. \tag{5.75}$$

The bending moment M at a generic cross-section along the column's axis is given by

$$M = M_a + PW + R_a x. \tag{5.76}$$

Substituting the expression for R_a, we obtain

$$M = M_a \left(1 - \frac{x}{l}\right) + M_b \frac{x}{l} + PW. \tag{5.77}$$

Defining

$$M_m = M_a\left(-\frac{x}{l}\right) + M_b\left(\frac{x}{l}\right) \tag{5.78}$$

the bending moment expression simplifies to

$$M = M_m + PW \tag{5.79}$$

where M_m represents the contribution of nodal moments and PW corresponds to the geometric nonlinearity contribution.

Assuming a linear elastic behavior for the material and considering the plane section hypothesis and moderate rotations, the bending moment M at any cross-section of the column can be described as

$$M = -k\frac{d^2W}{dx^2} = -kW'' \tag{5.80}$$

where k is the flexural stiffness of the section, and W'' represents an approximate value for the curvature $1/r$ of the column's axis.

By equating Eqs. (5.79) and (5.80), we obtain

$$M_m + PW = -kW''. \tag{5.81}$$

This equation represents the differential equilibrium equation of the column's axis, considering only geometric nonlinearity, as the stiffness k is assumed to be constant.

5.2.2.2 Finite Difference Method

The solution to the equilibrium equation (5.81) is obtained using the Finite Difference Method. This method consists of discretizing the continuous system into a discrete system composed of a geometric mesh, reducing the number of variables in the problem to a finite set, as illustrated in Figure 5.8 (HOLANDA; SILVA, 2021).

According to Castro (2001), the Finite Difference Method is one of the most widely used techniques for obtaining approximate solutions to differential equation systems. In this method,

Figure 5.8 – Finite difference mesh.

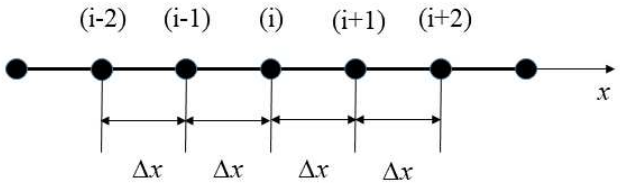

Source: Holanda and Silva (2021).

the derivatives that appear in the boundary condition definitions are approximated using finite differences, which involve the values of the unknown function at a set of equally spaced points, commonly referred to as discretization nodes.

The deformed shape of the column's axis is approximated using polynomial functions, allowing an expression for the curvature W'' to be obtained in terms of the displacements at various cross-sections.

Figure 5.9 illustrates the discretization of the column's axis into n equally spaced cross-sections from end a to end b.

Figure 5.9 – Discretization of the column's axis.

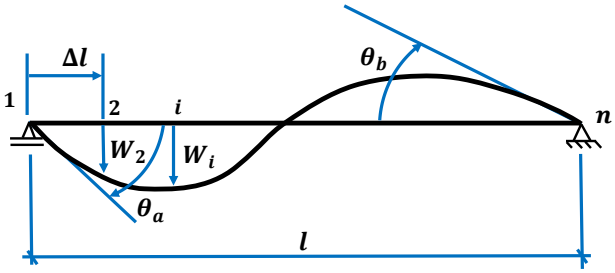

Adapted from Araújo (1993).

The distance Δl between two consecutive cross-sections is given by

$$\Delta l = \frac{l}{n-1} \tag{5.82}$$

where n is the number discretization nodes.

By fitting a quadratic polynomial to the displacements indicated in Figure 5.10, the following expressions for curvature at various cross-sections are obtained

$$W_1'' = \frac{2\left(W_2 - \theta_a \Delta l\right)}{\Delta l^2}; \tag{5.83}$$

$$W_i'' = \frac{W_{i-1} - 2W_i + W_{i+1}}{\Delta l^2}, \quad i = 2 \text{ to } n-1; \tag{5.84}$$

$$W_n'' = \frac{2\left(W_{n-1} + \theta_b \Delta l\right)}{\Delta l^2}. \tag{5.85}$$

Equations (5.83) to (5.85) are demonstrated in Appendix B.

Figure 5.10 – Coordinate system origin for each case.

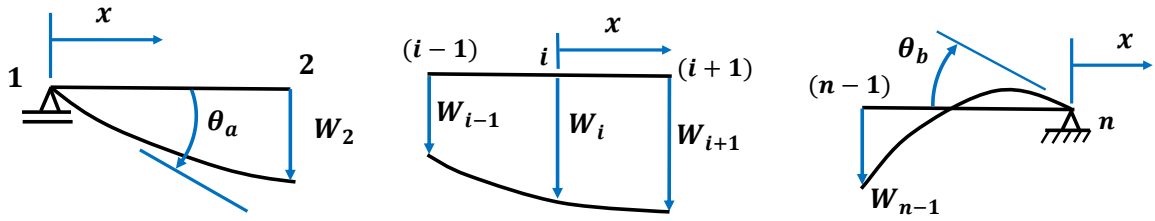

(a) Case A: support on the left. (b) Case B: intermediate nodes. (c) Case C: support on the right.

Adapted from Araújo (1993).

By applying the differential equilibrium equation (5.81) to all sections and substituting W'' with its finite difference approximations, a system of n linear algebraic equations with n unknowns is obtained in the form

$$\mathbf{M_m} + \mathbf{P_0 W} = \mathbf{K W} \tag{5.86}$$

where $\mathbf{M_m}$ is an n-element column vector, dependent on nodal moments.

Defining the auxiliary vectors

$$\psi_\mathbf{a} = \begin{bmatrix} 1 \\ 1-\xi \\ 1-2\xi \\ \vdots \\ 0 \end{bmatrix} \quad \text{and} \quad \psi_\mathbf{b} = \begin{bmatrix} 0 \\ \xi \\ 2\xi \\ \vdots \\ 1 \end{bmatrix} \tag{5.87}$$

where $\xi = \Delta l / l$, it follows that

$$\mathbf{M_m} = M_a \psi_\mathbf{a} + M_b \psi_\mathbf{b}. \tag{5.88}$$

The matrix $\mathbf{P_0}$, a square matrix $(n \times n)$ which accounts for second-order effects, is given by

$$\mathbf{P_0} = P\mathbf{I} \tag{5.89}$$

where

$$\mathbf{I}(i,j) = \begin{cases} 0, \text{if } i \neq j; \\ 1, \text{if } i = j; \\ 0, \text{if } i = j = 1; \\ 0, \text{if } i = j = n. \end{cases} \tag{5.90}$$

For consistency, since the safety formulation is applied in constructing the $M, N, 1/r$ diagram to obtain the secant stiffness, the design nodal moment values M_a and M_b, and the design axial force P_0 should also be divided by γ_{f3}.

The column vector $\mathbf{W}$, containing the unknown displacements, is given by

$$\mathbf{W} = \begin{bmatrix} \theta_a \\ W_2 \\ \vdots \\ W_i \\ \vdots \\ W_{n-1} \\ \theta_b \end{bmatrix} \tag{5.91}$$

The matrix $\mathbf{K}$, which accounts for the flexural stiffness of the beam, is square $(n \times n)$. The assembly of the stiffness matrix $\mathbf{K}$ can be derived from the moment-displacement relationships obtained from Eqs. (5.83) to (5.85), associated with Eq. (5.86):

$$M_1 = -\frac{2k}{\Delta l^2}(W_2 - \theta_a \Delta l) = -\frac{2k}{\Delta l^2} W_2 + \frac{2k}{\Delta l^2} \Delta l \, \theta_a \tag{5.92}$$

$$M_2 = -k\frac{(W_1 - 2W_2 + W_3)}{\Delta l^2} = \frac{2k}{\Delta l^2}W_2 - \frac{k}{\Delta l^2}W_3 \tag{5.93}$$

$$M_i = -k\frac{(W_{i-1} - 2W_i + W_{i+1})}{\Delta l^2} = -\frac{k}{\Delta l^2}W_{i-1} + \frac{2k}{\Delta l^2}W_i - \frac{k}{\Delta l^2}W_{i+1} \tag{5.94}$$

$$M_{n-1} = -k\frac{(W_{n-2} - 2W_{n-1} + W_n)}{\Delta l^2} = -\frac{k}{\Delta l^2}W_{n-2} + \frac{2k}{\Delta l^2}W_{n-1} \tag{5.95}$$

$$M_n = -\frac{2k}{\Delta l^2}(W_{n-1} + \theta_b \Delta l) = -\frac{2k}{\Delta l^2}W_{n-1} - \frac{2k}{\Delta l^2}\Delta l\,\theta_b \tag{5.96}$$

These equations can be written in matrix form as

$$\underbrace{\begin{bmatrix} M_1 \\ M_2 \\ \vdots \\ M_i \\ \vdots \\ M_{n-1} \\ M_n \end{bmatrix}}_{\mathbf{M}} = \underbrace{\frac{2k}{\Delta l^2}\begin{bmatrix} \Delta l & -1 & 0 & 0 & 0 & 0 & 0 \\ 0 & 1 & -1/2 & 0 & 0 & 0 & 0 \\ 0 & \ddots & \vdots & \vdots & 0 & 0 & 0 \\ 0 & \cdots & -1/2 & 1 & -1/2 & \cdots & 0 \\ \vdots & \vdots & \vdots & \vdots & \vdots & \ddots & 0 \\ 0 & 0 & 0 & 0 & -1/2 & 1 & 0 \\ 0 & 0 & 0 & 0 & 0 & -1 & -\Delta l \end{bmatrix}}_{\mathbf{K}} \underbrace{\begin{bmatrix} \theta_a \\ W_2 \\ \vdots \\ W_i \\ \vdots \\ W_{n-1} \\ \theta_b \end{bmatrix}}_{\mathbf{W}} \tag{5.97}$$

The stiffness matrix **K** is computed considering the stiffness of the reinforced concrete cross-section in the uncracked state. This stiffness is given by

$$k = E_c I_c + E_s \sum_{\mathrm{i}=1}^{\mathrm{n}} I_{si} \tag{5.98}$$

where I_c and I_{si} represent, respectively, the moment of inertia of the concrete cross-section and the moment of inertia of a generic reinforcement layer i with respect to the barycenter of the homogenized cross-section.

To homogenize the cross-section, the equivalent concrete area corresponding to the reinforcement layer is computed as

$$A_{c,eq} = n \cdot As \tag{5.99}$$

where n is the ratio between the elastic modulus of steel and the secant modulus of deformation of concrete, defined by

$$n = \frac{E_s}{E_{cs}}. \tag{5.100}$$

The elastic modulus of steel E_s can be assumed as 210 GPa, while the secant modulus of deformation of concrete E_{cs} is given by

$$E_{cs} = \alpha_i E_{ci} \tag{5.101}$$

where α_i is calculated as

$$\alpha_i = 0.8 + 0.2\frac{f_{ck}}{80} \leq 1.0 \tag{5.102}$$

with f_{ck} in MPa, and E_{ci} computed using Eq. (4.17).

An equation was developed to compute the depth x_G of the barycenter of a generalized homogenized section, based on the geometric relationships established in Figure 5.11 and the homogenization equation Eq. (5.99).

Figure 5.11 – Typical cross-section with coordinate axes for developing the section homogenization equations.

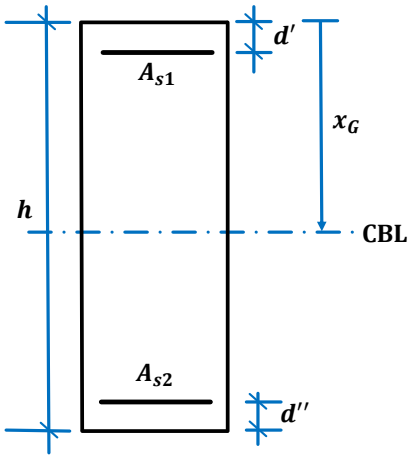

The barycenter depth x_G is given by

$$x_G = \frac{\left\{\frac{bh^2}{2} + (1-n)\left[A_{s2}(d''-h) - A_{s1}d'\right]\right\}}{\left[bh - (1-n)(A_{s1}+A_{s2})\right]}. \tag{5.103}$$

Thus, for the cross-section illustrated in Figure 5.11, the moments of inertia of the concrete section and reinforcement layers with respect to the barycenter of the homogenized section are calculated, respectively, as

$$I_c = \frac{bh^3}{12} + bh(h/2 - x_G)^2 \tag{5.104}$$

$$I_s = A_{s1}(x_G - d')^2 + A_{s2}(h - x_G - d'')^2. \tag{5.105}$$

5.2.2.3 Algorithm for the General Method

Figure 5.12 symbolically represents the moment-deflection relationship ($\mathbf{M} - \mathbf{W}$) for a slender reinforced concrete column, given a specified axial force P. It also illustrates the iterative process employed in the modified Newton-Raphson method, which determines the final bending moments in the column. The iterative procedure is outlined in the following steps:

Figure 5.12 – Iterative Scheme of the Moment-Deflection Diagram.

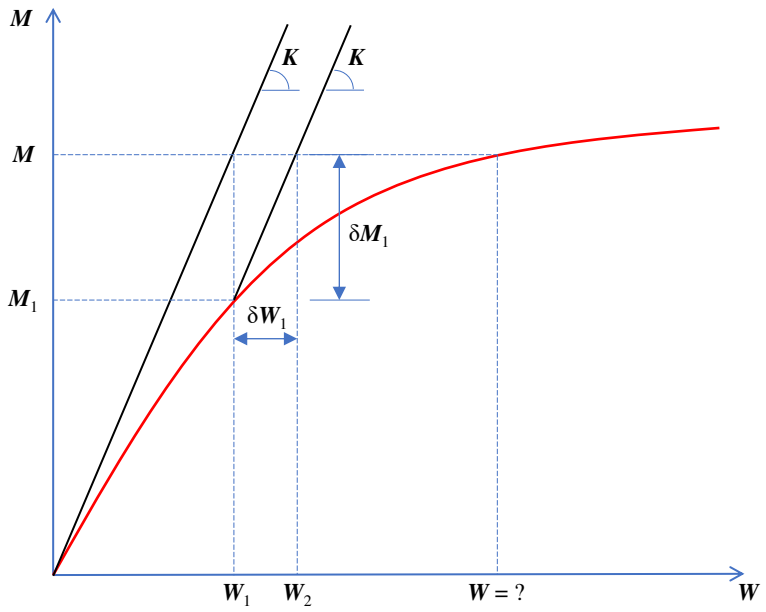

Adapted from Araújo (1993).

1. Compute the First Approximation of Displacements

The first approximation $\mathbf{W_1}$ for the displacements is obtained from the equation

$$\mathbf{M} = \mathbf{K}\mathbf{W_1}. \tag{5.106}$$

This system is solved using Crout decomposition with partial pivoting, which proved to be more efficient than Cholesky decomposition for the analyzed cases.

2. Compute the Curvatures Using Finite Differences
   Using finite difference approximations, the curvatures at the cross-sections of the column are computed based on the displacements in $\mathbf{W_1}$. These curvatures are calculated as

$$W_1'' = \frac{2\left(W_2 - \theta_a \Delta l\right)}{\Delta l^2}; \tag{5.83}$$

$$W_i'' = \frac{W_{i-1} - 2W_i + W_{i+1}}{\Delta l^2}, \quad i = 2 \text{ to } n-1; \tag{5.84}$$

$$W_n'' = \frac{2\left(W_{n-1} + \theta_b \Delta l\right)}{\Delta l^2}. \tag{5.85}$$

3. Compute Internal Moments Using the $M, N, 1/r$ Diagram
   The corresponding internal moments $\mathbf{M_1}$ are obtained for each computed curvature by referencing the $M, N, 1/r$ diagram.
4. Compute the Imbalance Vector
   The imbalance vector $\delta\mathbf{M_1}$, representing the difference between external and internal moments, is given by

$$\delta\mathbf{M_1} = (\mathbf{M} + P\mathbf{W_1}) - \mathbf{M_1}. \tag{5.107}$$

5. Compute the Displacement Correction $\delta\mathbf{W_1}$
   The required displacement correction $\delta\mathbf{W_1}$ is determined by solving the system

$$\delta\mathbf{M_1} = \mathbf{K}\delta\mathbf{W_1}. \tag{5.108}$$

This system is again solved using Crout decomposition.

6. Update the Displacements
   The updated displacements set $\mathbf{W_2}$ is obtained as

$$\mathbf{W_2} = \mathbf{W_1} + \delta\mathbf{W_1}. \tag{5.109}$$

7. Iterative Convergence Verification
   The iterative process continues until the following convergence criteria are satisfied for a generic iteration j

$$\left| \frac{\delta W_j^i}{W_j^i} \right| \leq \text{tolerance}, \quad (i = 1 \text{ to } n) \tag{5.110}$$

and simultaneously,

$$\frac{||\delta \mathbf{M_j}||}{||\mathbf{M}||} \leq \text{tolerance}. \tag{5.111}$$

A tolerance value of 0,02 was adopted. In Eq. (5.110), W_j^i represents the displacement at cross-section i computed in iteration j. In Eq. (5.110), the notation $||\quad||$ denotes the vector norm.

Unlike the Standard Column Method, which determines only the maximum moment of the column, the General Method allows for the computation of the moment distribution across all considered cross-sections.

For applying the General Method, the $M,N,1/r$ diagrams are pre-generated and may be constructed using either an idealized stress-strain diagram (diagram from Eq. 3.1 – Figure 3.1) or the stress-strain diagram for nonlinear analysis (diagram from Eq. 3.7 – Figure 3.2), with or without considering creep effects.

5.2.3 Semi-General Method Coupled with $M,N,1/r$ Diagrams

A variation of the General Method, the *Semi-General Method*, was also developed and analyzed based on Casagrande (2016). In this approach, instead of scanning the $M,N,1/r$ in Step 3 of the previously described algorithm, only the secant stiffness from the diagram, as illustrated in Figure 3.6, is used.

Thus, the moments, in dimensionless form, are given by

$$\mu = \kappa_{\text{sec}} \cdot \left(\frac{h}{r}\right). \tag{5.112}$$

This adjustment simplifies the method by eliminating the need for a full nonlinear search in the $M,N,1/r$ diagram while still incorporating physical nonlinearity through the secant stiffness. This approach reduces computational complexity and is easier to apply in practical cases; however, it provides a less precise consideration of physical nonlinearity than the complete General Method. Despite being computationally simpler, it still depends on the precomputed $M,N,1/r$ diagrams, which can be a limiting factor in its application.

5.3 METHODS FOR CONSIDERING CREEP EFFECTS

This section presents the methodology implemented in the Java-based computational program for considering creep effects in reinforced concrete columns. The approach is based on the theoretical concepts introduced in Chapter 4 and focuses on two numerical strategies: the

Extended Stress-Strain Curve and the Extended Stress-Strain Curve with φ Calculated by the Kelvin-Voigt Rheological Model. The following subsections detail the formulation and computational procedures for each approach.

5.3.1 Extended Stress-Strain Curve

The adopted strategy is directly based on the theoretical concepts of the method presented in Subsection 4.3.

In the implementation, when defining a concrete type with an idealized stress-strain diagram (diagram from Eq. 3.1 – Figure 3.1), the program incorporates creep effects by multiplying the strain values ε_{c2} and ε_{cu} by $(1+\varphi)$, as described in Eq. (4.3) and illustrated in Figure 4.1. The same approach is applied when using the stress-strain diagram for nonlinear analysis (diagram from Eq. 3.7 – Figure 3.2), where the strains ε_{c1} and ε_{cu1} are also multiplied by $(1+\varphi)$. The equations governing the stress-strain diagrams remain unchanged, but they are applied using these adjusted strain values, resulting in an extended stress-strain diagram incorporating creep effects.

As previously discussed in Subsection 4.3, Brazilian studies typically use the creep coefficient φ. In contrast, international studies and design codes commonly employ the effective creep coefficient φ_{ef}, calculated using Eq. (4.14). The effective creep coefficient φ_{ef} accounts for the proportion of long-term bending moments in a given load combination, considering that only long-term components fully influence creep behavior. This study adopted the effective creep coefficient φ_{ef} as the standard approach, providing a more comprehensive and accurate analysis.

These extended stress-strain diagrams can be directly used in the construction of $M,N,1/r$ diagrams, following the algorithm described in Subsection 5.1.6. This enables the generation of $M,N,1/r$ diagrams incorporating creep effects, allowing for a more refined second-order analysis of reinforced concrete columns.

5.3.2 Extended Stress-Strain Curve with φ Calculated by the Kelvin-Voigt Rheological Model

Several approaches were explored to incorporate creep effects by rheological models into the implemented methods, particularly in the $M,N,1/r$ diagram construction and the General Method. A straightforward approach that integrates well with the existing methods is the computation of a creep coefficient φ_{KV} using the Kelvin-Voigt Model, as described below.

1. Perform the Equilibrium Calculation Using the General Method

The standard General Method is executed first, following the conventional equilibrium formulation.

2. Compute the Immediate Strain ε_0 at the Most Compressed Fiber
   The immediate strain ε_0 at the most compressed fiber of each cross-section is determined using the compatibility equation

$$\varepsilon_0 = \frac{h}{r}\left(\beta_y + \frac{1}{2} - \beta_x\right). \tag{5.18}$$

3. Determine the Stress at the Most Compressed Fiber
   Using the stress-strain diagram, the stress at the most compressed fiber is computed based on the previously determined strain. After calculating the stress, the ratio between quasi-permanent moments and design moments is applied, as in the calculation of the effective creep coefficient φ_{ef} in Eq. (4.14).
4. Compute the Creep Strain Using the Kelvin-Voigt Model
   The creep strain at the most compressed fiber is obtained using the governing equation for creep behavior in the Kelvin-Voigt Model

$$\varepsilon_{KV} = \frac{\sigma_0}{E}\left(1 - e^{\frac{-E}{\eta}t}\right). \tag{4.26}$$

   A time period of 50 years (18250 days) was adopted for the analysis.
5. Compute the Creep Coefficient φ_{KV}
   The creep coefficient for each node of the discretization is calculated as

$$\varphi_{KV} = \frac{\varepsilon_{KV}}{\varepsilon_0}. \tag{5.113}$$

6. Modify the Stress-Strain Diagram to Incorporate Creep Effects
   The stress-strain diagram is adjusted by shifting the strain values by a factor of $(1+\varphi_{KV})$ to generate the extended stress-strain curve that accounts for creep effects by the Kelvin-Voigt Model.
7. Reprocess the General Method
   Finally, the General Method is rerun using the updated stress-strain diagram, incorporating the newly computed creep effects into the analysis. This reevaluation uses a $M, N, 1/r$ diagram specific to each cross-section instead of a single generalized diagram.

In this procedure, a more comprehensive creep coefficient is computed, which depends on the applied stress and is specific to each cross-section. As a result, this approach leads to an extended stress-strain diagram and a unique $M, N, 1/r$ diagram for each analyzed section, ensuring that the nonlinear behavior is accurately captured for each individual cross-section.

To apply Eq. (4.26), it is necessary to define the parameters E and η. These parameters were calibrated based on experimental data collected by Wassin (2002 apud OLIVEIRA, 2017, p. 95).

In that study, Oliveira (2017) reproduced the experimental data and fitted the response using the Boltzmann rheological model. Using the relationships provided in Becho (2020), which connect the parameters of the Boltzmann and Kelvin-Voigt models, the following conversion expressions were adopted

$$E_{KV} = \frac{E_1^B E_2^B}{E_1^B + E_2^B}, \tag{5.114}$$

$$\eta_{KV} = \eta_B \frac{E_{KV}}{E_2^B}. \tag{5.115}$$

Based on these expressions, the calibrated parameters for the Kelvin-Voigt model were defined as

$$\begin{aligned} E &= 4.48\,\text{GPa}, \\ \eta &= 360\,\text{GPa}\cdot\text{days}. \end{aligned} \tag{5.116}$$

6 RESULTS AND DISCUSSION

This chapter presents numerical examples of reinforced concrete columns analyzed using different computational approaches, as described in the Methodology (Chapter 5). The objective is to evaluate the effectiveness and accuracy of various creep modeling strategies in predicting second-order effects, providing a comparative assessment of the selected methods.

Four case studies are considered: the first three are based on Casagrande (2016), who conducted a similar comparative study comparing different creep simulation methods. These cases serve as a benchmark for validating the models developed in this research. By reproducing Casagrande's examples, the accuracy and consistency of the implemented models are assessed, enabling a direct comparison among the different calculation approaches.

The fourth example, adapted from Pastore (2020), examines the influence of column slenderness on creep effects. In this case, a single cross-section is analyzed while varying the column height. This allows for an evaluation of how different creep modeling strategies respond to increasing slenderness, providing further insight into the applicability and limitations of each approach.

Each example is structured with detailed analyses of the methods used, followed by a comparative discussion of the results. The findings contribute to understanding the discrepancies between calculation strategies and their impact on the structural response of reinforced concrete columns.

Before presenting the numerical examples, the calculation of the creep coefficient φ used throughout the analyses is introduced. This value is obtained using the full procedure described in Annex A of NBR 6118 (2023).

6.1 CALCULATION OF THE CREEP COEFFICIENT ACCORDING TO THE COMPLETE PROCEDURE FROM ANNEX A OF NBR 6118 (2023)

The creep coefficient φ adopted in the analyses is calculated based on the complete procedure described in Annex A of NBR 6118 (2023), as detailed in Subsection 4.1.1. This procedure involves a series of assumptions regarding material properties, environmental conditions, and loading history.

According to NBR 6118 (2023), the creep coefficient $\varphi(t,t_0)$ is defined as

$$\varphi(t,t_0) = \varphi_a + \varphi_{f\infty}[\beta_f(t) - \beta_f(t_0)] + \varphi_{d\infty}\beta_d. \tag{4.5}$$

Initially, the final age is assumed as $t = \infty$. For the calculation of the fictitious age t_0, it is assumed that the load is applied after 30 days, that normal-hardening Portland Cement (CP I or CP II) is used ($\alpha = 2$), and that the average ambient temperature during the period is 20 °C. Thus,

$$t_0 = \alpha \sum_i \frac{T_i + 10}{30} \Delta t_{\text{ef,i}} = 2 \cdot \frac{20+10}{30} 30 = 60. \tag{6.1}$$

For the instantaneous creep coefficient, it is assumed, based on NBR 6118 (2023), that after 28 days, the concrete has already reached its final strength. Therefore, $f_c(t_0) = f_c(t_\infty)$, so

$$\varphi_a = 0,8 \left[1 - \frac{f_c(t_0)}{f_c(t_\infty)} \right] = 0. \tag{6.2}$$

The final value of the irreversible delayed creep coefficient $\varphi_{f\infty}$ is computed in terms of the coefficients φ_{1c} and φ_{2c}.

φ_{1c} is a coefficient dependent on the ambient relative humidity U and the concrete consistency. For slump values between 5 and 9 cm and $U \leq 90\%$, it can be calculated as

$$\varphi_{1c} = 4.45 - 0.035U. \tag{6.3}$$

Assuming an ambient relative humidity of 70%, this coefficient is computed as

$$\varphi_{1c} = 4.45 - 0.035U = 2.0. \tag{6.4}$$

φ_{2c} is a coefficient dependent on the fictitious thickness h_{fic} of the element, given by

$$\varphi_{2c} = \frac{42+h}{20+h} \tag{6.5}$$

where h is the weighted fictitious thickness, defined as

$$h = \gamma h_{\text{fic}}, \tag{4.10}$$

expressed in centimeters.

From Table 4.2, for outdoor exposure conditions ($U = 70\%$), γ is defined as 1,5. The fictitious thickness is computed as

$$h_{\text{fic}} = \frac{2A_c}{u} = \frac{2 \cdot 20 \cdot 60}{2 \cdot (20+60)} = 15\,\text{cm}. \tag{6.6}$$

Thus, the weighted fictitious thickness is calculated as

$$h = \gamma h_{\text{fic}} = 1.5 \cdot 15 = 22.5\,\text{cm}. \tag{6.7}$$

From this, φ_{2c} is computed as

$$\varphi_{2c} = \frac{42+h}{20+h} = \frac{42+22.5}{20+22.5} = 1.52. \tag{6.8}$$

Therefore, the final value of the irreversible delayed creep coefficient is given by

$$\varphi_{f\infty} = \varphi_{1c}\varphi_{2c} = 2.0 \cdot 1.52 = 3.04. \tag{6.9}$$

For $t = \infty$, it is assumed that $\beta_f(t) = 1$. Meanwhile, $\beta_f(t_0)$ is computed as

$$\beta_f(t) = \frac{t^2 + At + B}{t^2 + Ct + D} = 0.48, \tag{6.10}$$

where the terms A, B, C and D are calculated using Eqs. (4.12), based on the weighted fictitious thickness in meters.

The final value of the reversible delayed creep coefficient $\varphi_{d\infty}$ is considered equal to 0.4.

Finally, the coefficient $\beta_d(t)$, associated with reversible delayed strain, is computed as a function of the elapsed time $(t - t_0)$ after loading

$$\beta_d(t) = \frac{t - t_0 + 20}{t - t_0 + 70} \tag{4.13}$$

which assumes a value of 1.0 when $t = \infty$.

Thus, the creep coefficient is calculated as

$$\varphi(t,t_0) = \varphi_a + \varphi_{f\infty}[\beta_f(t) - \beta_f(t_0)] + \varphi_{d\infty}\beta_d = 0 + 3.04[1 - 0.48] + 0.4 \cdot 1.0 = 1.98. \quad (6.11)$$

The adopted value for the creep coefficient is $\varphi = 2.0$.

6.2 EXAMPLE 1 - COLUMN UNDER AXIAL COMPRESSION

The first example in this study reproduces Example 1 from Casagrande (2016). In this case, all the methods proposed by the author are implemented, considering models both *without* and *with* creep effects. The analyzed methods include:

- The Standard Column Method with Approximate Stiffness κ,
- The Standard Column Method coupled with $M,N,1/r$ diagrams,
- The Semi-General Method coupled with $M,N,1/r$ diagrams, and
- The General Method coupled with $M,N,1/r$ diagrams.

In the Standard Column Method with Approximate Stiffness κ, creep effects are considered through the additional eccentricity e_{cc}. For the remaining methods, which utilize $M,N,1/r$ diagrams, creep effects - when included - are accounted for through the extended stress-strain curve approach.

An additional analysis is conducted for this example, not included in Casagrande (2016), where the General Method coupled with $M,N,1/r$ diagrams is applied while incorporating creep effects through the Kelvin-Voigt rheological model.

This first example considers a simply supported rectangular column with an equivalent length of $\ell_e = 3.0\,\text{m}$, subjected to a design axial force of $N_{Sd} = 2100\,\text{kN}$, as illustrated in Figure 6.1. The material properties are defined as follows:

- Concrete: $f_{ck} = 30\,\text{MPa}$;
- Steel: $f_{yk} = 500\,\text{MPa}$ and an elastic modulus of $E = 210\,\text{GPa}$;
- Creep coefficient: $\varphi = 2.0$.

No initial bending moments are considered in this example. Only the minimum moments prescribed by NBR 6118 (2023) are taken into account.

Casagrande (2016) considered combined bending and axial loading only in the least favorable direction, corresponding to the higher slenderness ratio. The slenderness ratios for the rectan-

Figure 6.1 – Initial data for Example 1.

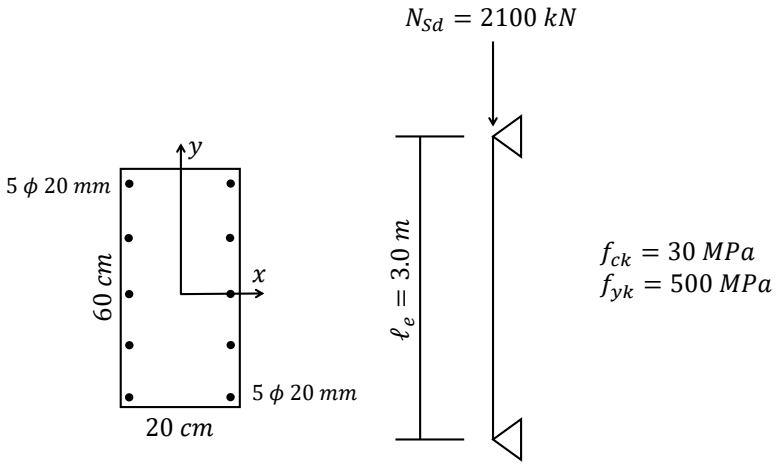

Adapted from Casagrande (2016).

gular cross-section are calculated as

$$\lambda_x = \sqrt{12} \cdot \frac{\ell_e}{h} = \sqrt{12} \cdot \frac{300}{20} = 52, \tag{6.12}$$

$$\lambda_y = \sqrt{12} \cdot \frac{\ell_e}{h} = \sqrt{12} \cdot \frac{300}{60} = 17. \tag{6.13}$$

Thus, bending moments are assumed to act along the x-direction with cross-section dimensions:

- Height $h = 20\,\text{cm}$,
- Width $b_w = 60\,\text{cm}$, and
- Slenderness ratio $\lambda = 52$.

The minimum moment is determined as

$$M_{1d,min} = N_{Sd}(0.015 + 0.03h) = 2100(0.015 + 0.03 \cdot 0.2) = 44.1\,\text{kN m}$$
$$\therefore M_{1d,min} = 4410\,\text{kN cm}. \tag{6.14}$$

To verify whether second-order effects must be considered, the parameters α_b and λ_1 are evaluated. For this case, the value of α_b is assumed to be 1.0, as the column is subjected to moments lower than the minimum required.

The λ_1 parameter is then calculated as

$$\lambda_1 = \frac{25 + 12.5(e_1/h)}{\alpha_b} = \frac{25 + 12.5\left(\frac{0/2100}{20}\right)}{1.0} = 25 < 35 \therefore \lambda_1 = 35 \tag{6.15}$$

Since $\lambda_1 < \lambda < 90$, the column is classified as moderately slender, meaning that second-order local effects can be evaluated using approximate methods based on the Standard Column approach. Furthermore, creep effects are not mandatory for this case, according to NBR 6118 (2023).

6.2.1 Standard Column Method with Approximate Stiffness κ

The total bending moment, $M_{d,tot}$, in the standard column method with approximate stiffness κ is determined directly using the parameters a, b and c, as described in Subsection 3.3.1.2. These parameters are computed as

$$\begin{cases} a = 5h = 5 \cdot 20 = 100, \\ b = h^2 N_d - \dfrac{N_d l_e^2}{320} - 5h\alpha_b M_{1d,A} = 20^2 \cdot 2100 - \frac{2100 \cdot 300^2}{320} - 5 \cdot 20 \cdot 1 \cdot 4410 = -191625, \\ c = -N_d h^2 \alpha_b M_{1d,A} = -2100 \cdot 20^2 \cdot 1 \cdot 4410 = -3704.4 \times 10^6. \end{cases} \tag{6.16}$$

Thus, the total bending moment can be computed using Eq. (3.40)

$$M_{d,tot} = \frac{-b + \sqrt{b^2 - 4ac}}{2a} = 7119\,\text{kN}\,\text{cm}. \tag{6.17}$$

Since this is a straightforward application of formulas, this result is identical to that obtained by Casagrande (2016).

6.2.2 Standard Column Method with Approximate Stiffness κ and Additional Eccentricity e_{cc}

The additional creep-induced eccentricity is determined according to NBR 6118 (2023), using Eq. (4.15)

$$e_{cc} = \left(\frac{M_{sg}}{N_{sg}} + e_a\right)\left(2.718^{\frac{\varphi N_{sg}}{N_e - N_{sg}}} - 1\right). \tag{4.15}$$

The term M_{Sg}/N_{Sg} represents the eccentricity resulting from the applied structural loads in the quasi-permanent combination. Under typical design conditions, these internal forces would be

obtained from a global structural analysis considering this loading condition. However, due to the lack of detailed information regarding the acting loads, Casagrande (2016) assumed that 25% of the total load corresponds to short-term effects.

$$N_{Sgk} = 0.75 \cdot \frac{N_d}{1.4} = 0.75 \cdot \frac{2100}{1.4} = 1125\,\text{kN}, \tag{6.18}$$

$$N_{Sqk} = 0.25 \cdot \frac{N_d}{1.4} = 0.25 \cdot \frac{2100}{1.4} = 375\,\text{kN}. \tag{6.19}$$

For the quasi-permanent load combination, the applied axial force is determined as

$$N_{Sg} = N_{Sgk} + \psi_2 \cdot N_{Sqk} = 1125 + 0.3 \cdot 375 = 1237.5\,\text{kN}. \tag{6.20}$$

A residential building was assumed, and therefore the combination factor $\psi_2 = 0.3$ was adopted.

Next, the accidental eccentricity is computed as

$$\theta_1 = \frac{1}{100\sqrt{\ell_e}} = \frac{1}{100\sqrt{3.0}} = \frac{1}{173.2} > \theta_{1max} = \frac{1}{200} \quad \therefore \quad \theta_1 = \theta_{1max} = \frac{1}{200} \tag{6.21}$$

$$e_a = \theta \cdot \frac{\ell_e}{2} = \frac{1}{200}\frac{300}{2} = 0.75\,\text{cm}. \tag{6.22}$$

The initial tangent modulus of elasticity of concrete, E_{ci}, is calculated assuming $\alpha_E = 1.0$ (granite or gneiss aggregate)

$$E_{ci} = \alpha_E \cdot 5600\sqrt{f_{ck}} = 1.0 \cdot 5600\sqrt{30} = 30\,672\,\text{MPa} = 3067.2\,\text{kN/cm}^2. \tag{6.23}$$

The cross-section moment of inertia is obtained as

$$I_c = \frac{0.6 \cdot 0.2^3}{12} = 4 \times 10^{-4}\,\text{m}^4 = 40 \times 10^3\,\text{cm}^4. \tag{6.24}$$

Thus, the Euler critical load N_e is computed using Eq. (4.16)

$$N_e = \frac{10 E_{ci} I_c}{{\ell_e}^2} = \frac{10 \cdot 3067.2 \cdot 40 \times 10^3}{300^2} = 13\,632\,\text{kN}. \tag{6.25}$$

Finally, the additional creep-induced eccentricity e_{cc} is determined as

$$e_{cc} = \left(\frac{0}{1237.5} + 0.75\right)\left(2.718^{\frac{2\cdot 1237.5}{13632-1237.5}} - 1\right) = 0.166\,\text{cm}. \tag{6.26}$$

The additional bending moment M_{cc} is given by

$$M_{cc} = N_{Sd} \cdot e_{cc} = 2100 \cdot 0.166 = 349\,\text{kN cm}. \tag{6.27}$$

Thus, the total bending moment considering creep effects is obtained as

$$M_d = 7119 + 349 = 7468\,\text{kN cm}. \tag{6.28}$$

Casagrande (2016) obtained a total moment of 7530 kN cm. The slight discrepancy between the results arises from the author using the secant modulus of elasticity E_{cs} instead of the initial tangent modulus E_{ci}.

Based on this bending moment value, Casagrande (2016) carried out the reinforcement design for the cross-section. To compare the results, the same reinforcement configuration was adopted, consisting of two layers of 5 bars with a diameter of 20.00 mm, as illustrated in Figure 6.1.

6.2.3 Standard Column Method Coupled with $M, N, 1/r$ Diagrams (Without Creep)

This method is implemented directly in the developed computational program, starting with constructing the $M, N, 1/r$ diagrams. The diagrams presented in Figure 6.2 depict the moment-curvature relationships obtained for both design values and the safety formulation, comparing them with the curves from Casagrande (2016).

The curves obtained from the computational program and those from Casagrande (2016) for design values are completely superimposed, indicating a strong agreement between the results. However, a discrepancy is observed in the curves corresponding to the safety formulation, where a separation occurs.

The dimensionless secant stiffness κ calculated by the program was 66.506, while Casagrande (2016) obtained 71.093. Finally, the program computed a final bending moment at the critical section of $M_{d,tot} = 5889\,\text{kN cm}$, whereas Casagrande (2016) obtained $M_{d,tot} = 5947\,\text{kN cm}$. This difference was anticipated due to the divergence between the diagrams in the safety formulation.

Figure 6.2 – $M,N,1/r$ diagrams for Example 1, without creep effects.

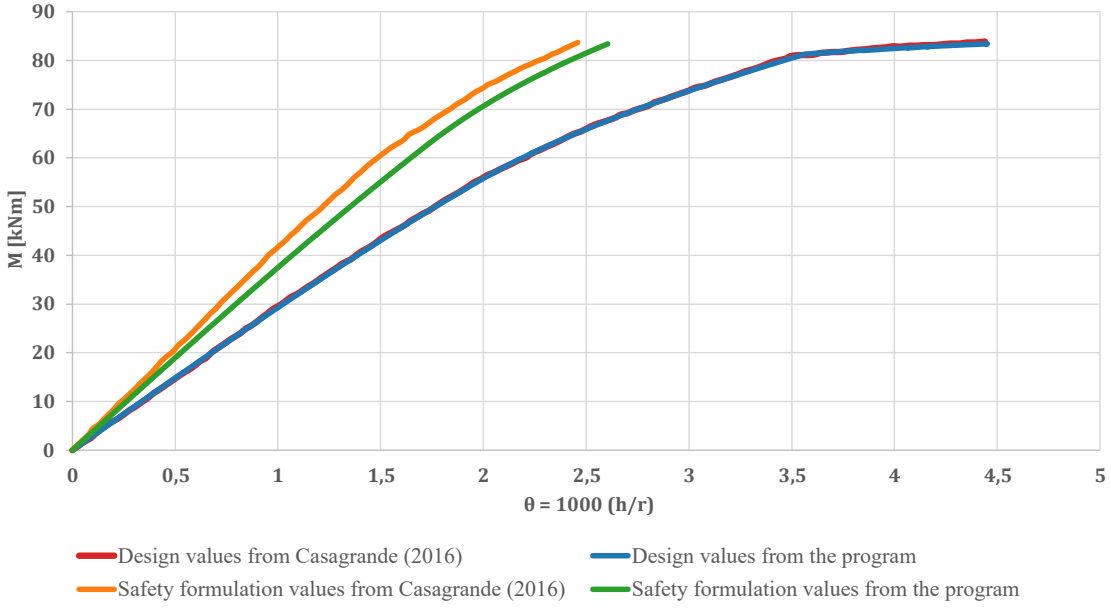

6.2.4 Standard Column Method Coupled with $M,N,1/r$ Diagrams Considering Creep Effects Through the Extended Stress-Strain Curve

In this case, before constructing the $M,N,1/r$ diagram, the stress-strain curve is shifted by the value of the creep coefficient. As previously discussed, and following the approach adopted by Casagrande (2016), this study employs the effective creep coefficient φ_{ef}, calculated as

$$\varphi_{ef} = \varphi \frac{M_{Sg}}{M_d} \tag{4.14}$$

where

$$M_{Sg} = N_{Sg} \cdot e_{1d,min} = 1237.5 \cdot 0.021 = 25.99\,\text{kN m} = 2599\,\text{kN cm} \tag{6.29}$$

and

$$M_d = M_{1d,min} = 4410\,\text{kN cm}. \tag{6.30}$$

Thus, the effective creep coefficient is given by

$$\varphi_{ef} = \varphi \frac{M_{Sg}}{M_d} = 2.0 \cdot \frac{2599}{4410} = 1.18. \tag{6.31}$$

With the computed value of φ_{ef}, the construction of the $M,N,1/r$ diagrams proceeds, as illustrated in Figure 6.3.

Figure 6.3 – $M,N,1/r$ diagrams for Example 1, with creep effects.

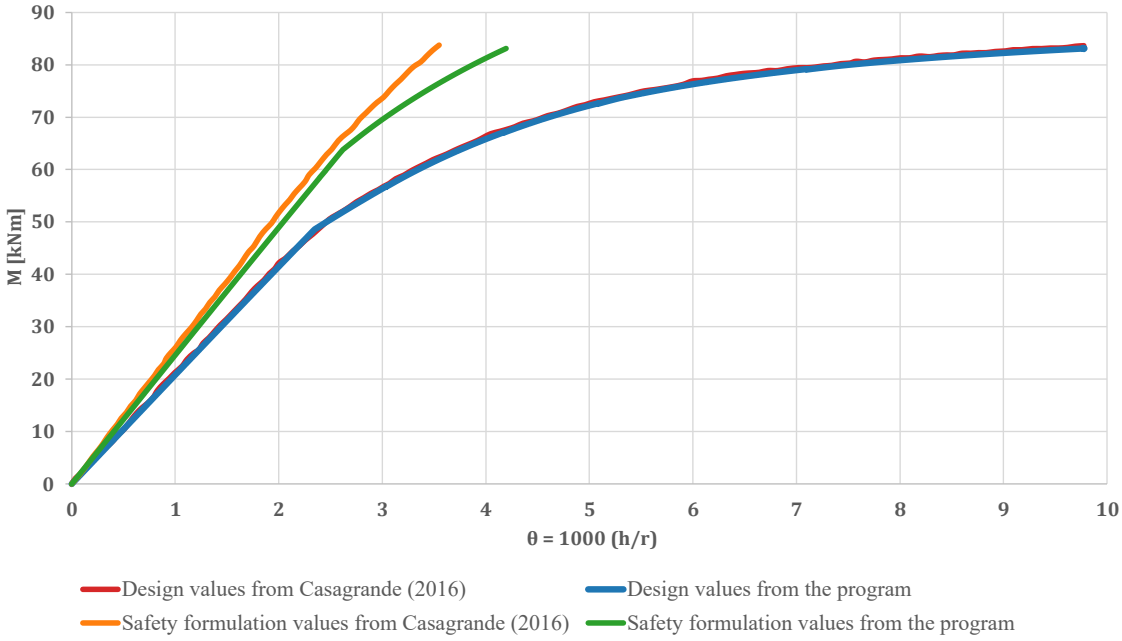

Similar to the analysis without creep effects, the curves obtained by the computational program and those from Casagrande (2016), are perfectly aligned for the design values, while a discrepancy is observed for the safety formulation. In this case, the difference appears only in the final phase of the curves, where a separation occurs.

The dimensionless secant stiffness κ calculated by the program was 42.367, while Casagrande (2016) obtained 47.431. Finally, the program computed a final bending moment at the critical section of $M_{d,tot} = 7281\,\text{kN}\,\text{cm}$, whereas Casagrande (2016) obtained $M_{d,tot} = 7199\,\text{kN}\,\text{cm}$. Once again, this difference was expected, resulting from the divergence between the diagrams in the safety formulation.

6.2.5 Semi-General Method Coupled with $M,N,1/r$ Diagrams (Without Creep)

Following the methodology previously outlined, the Semi-General Method is applied without considering creep effects in the construction of the $M,N,1/r$ diagrams.

This method allows for determining bending moments at each node considered in the analysis. Consequently, the entire moment distribution curve along the height of the column can be compared, as illustrated in Figure 6.4. Despite the differences in the moment-curvature relationships discussed earlier, and the distinct methodological approaches – since Casagrande

(2016) employs the Mohr Analogy, whereas this study adopts the finite difference method – the results converged consistently along the entire column length.

6.2.6 Semi-General Method Coupled with $M, N, 1/r$ Diagrams Considering Creep Effects Through the Extended Stress-Strain Curve

The Semi-General Method is applied with the $M, N, 1/r$ diagrams, incorporating creep effects through the extended stress-strain curve in its formulation. The complete moment distribution curve along the height of the column is shown in Figure 6.5.

This curve exhibits noticeable differences in the results, with larger deviations occurring in regions where second-order effects are more pronounced. This discrepancy can be attributed to greater divergence in the moment-curvature relationship when creep is incorporated, especially in the final portion of the diagram, which may affect the secant stiffness. Additionally, as previously mentioned, Casagrande (2016) adopts a different methodology, based on Mohr's analogy.

Figure 6.4 – Moment distribution diagram for Example 1, analyzed using the Semi-General Method without creep effects.

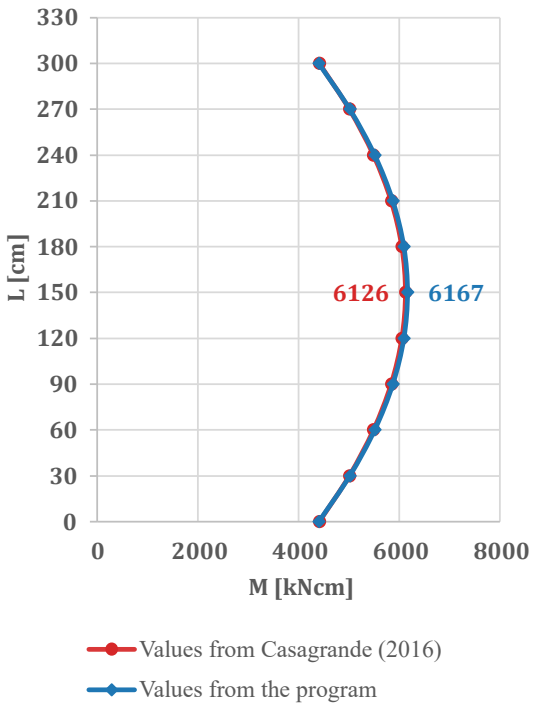

Figure 6.5 – Moment distribution diagram for Example 1, analyzed using the Semi-General Method with creep effects.

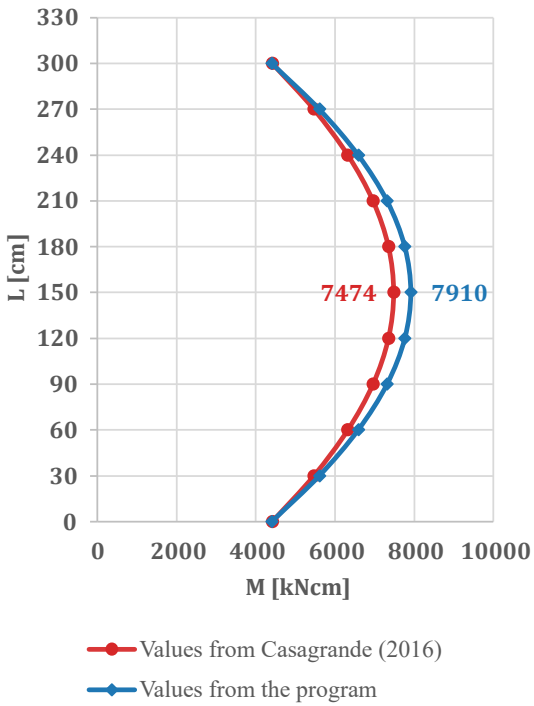

6.2.7 General Method Coupled with $M, N, 1/r$ Diagrams (Without Creep)

Following the methodology previously outlined, the General Method – expected to be a more comprehensive and accurate approach – is applied without considering creep effects in the

construction of the $M, N, 1/r$ diagrams.

This method also enables determining bending moments at each node considered in the analysis. As a result, the entire moment distribution curve along the height of the column can be compared, as illustrated in Figure 6.6.

Despite the differences in the moment-curvature relationships discussed earlier, and the distinct methodological approaches, the results consistently converged along the entire column length.

6.2.8 General Method Coupled with $M, N, 1/r$ Diagrams Considering Creep Effects Through the Extended Stress-Strain Curve

The General Method is applied with the $M, N, 1/r$ diagrams, incorporating creep effects through the extended stress-strain curve in its formulation.

The complete moment distribution curve along the height of the column is presented in Figure 6.7. As observed in the General Method without creep effects, the results showed consistent agreement with those reported by Casagrande (2016) along the entire column length.

Figure 6.6 – Moment distribution diagram for Example 1, analyzed using the General Method without creep effects.

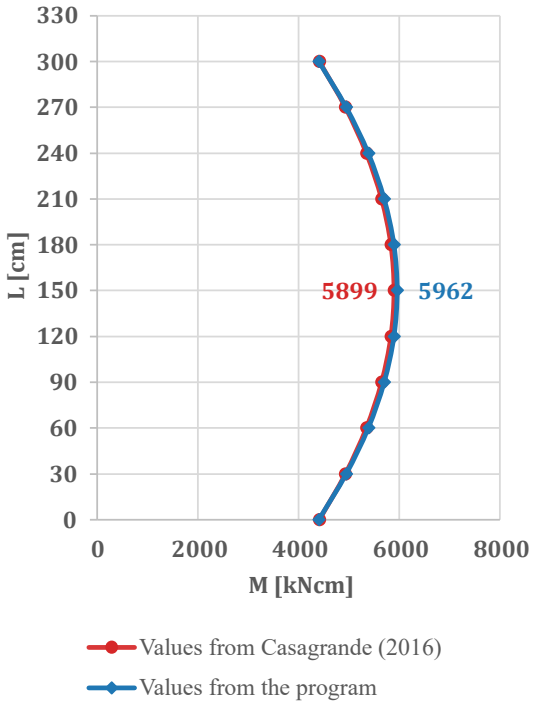

Figure 6.7 – Moment distribution diagram for Example 1, analyzed using the General Method with creep effects.

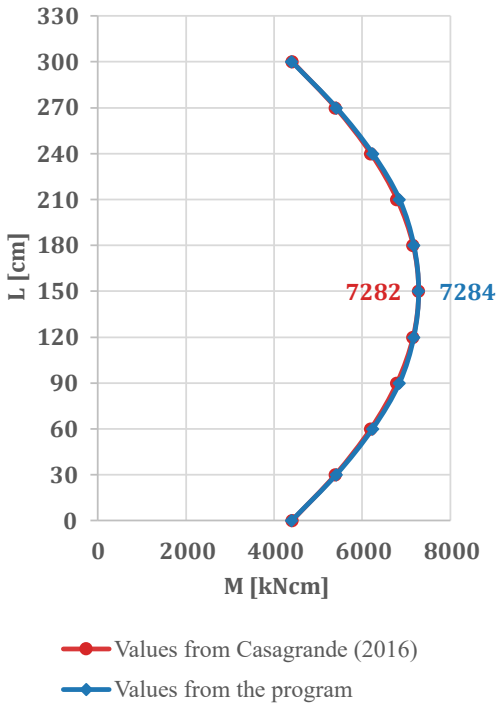

6.2.9 General Method Coupled with $M,N,1/r$ Diagrams Considering Creep Effects Through the Kelvin-Voigt Rheological Model

Finally, the application of an additional method, not presented by Casagrande (2016), is performed. This approach consists of the General Method coupled with $M,N,1/r$, but with creep effects computed using the Kelvin-Voigt rheological model.

By applying the method, the creep coefficient φ_{KV} obtained from the Kelvin-Voigt formulation at each analysis node, can be determined. The distribution of these coefficients is depicted in Figure 6.8.

Figure 6.8 – Distribution of creep coefficients according to the Kelvin-Voigt Rheological Model for Example 1.

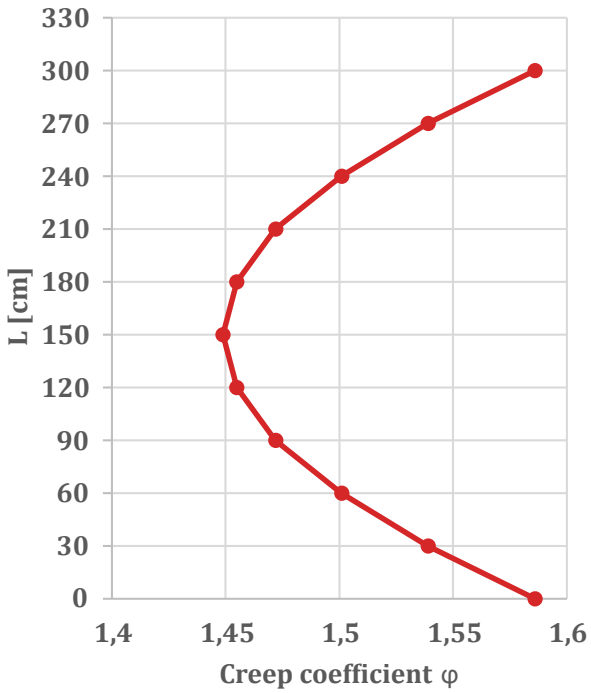

From Figure 6.8, it can be observed that the creep coefficients decrease as second-order effects become more significant. Furthermore, the magnitude of the obtained creep coefficients is significantly higher than the effective creep coefficient $\varphi_{ef} = 1.18$ used in the previous analyses.

The complete moment distribution curve along the height of the column is presented in Figure 6.9. Due to the higher creep coefficients obtained in this approach, the bending moments calculated here are considerably greater than those obtained in the previous General Method analysis.

Figure 6.9 – Moment distribution diagram for Example 1, analyzed using the General Method with creep effects evaluated by the Kelvin-Voigt Rheological Model.

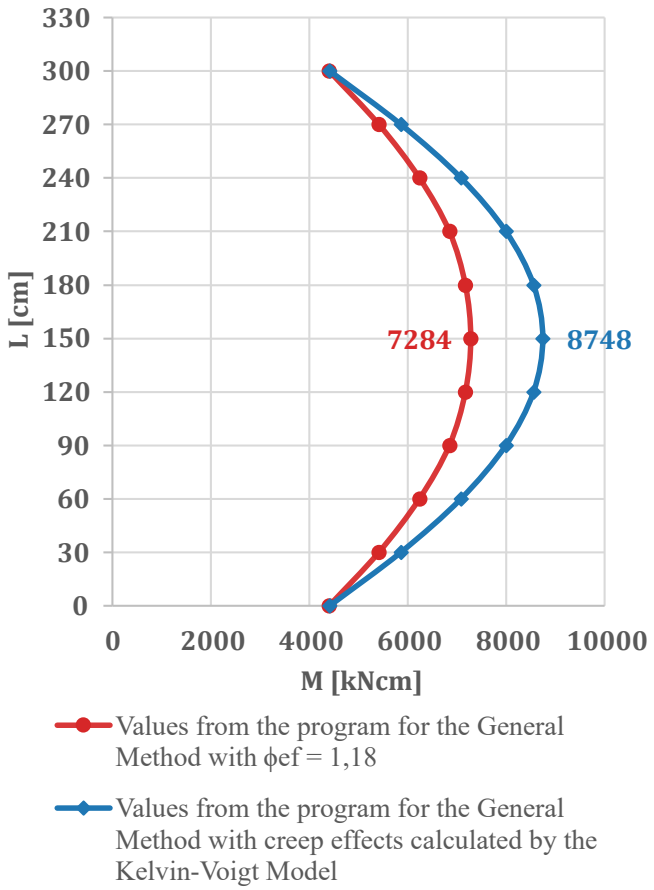

6.2.10 Comparison of Results

Table 6.1 compares the results obtained using the developed computational program and those from Casagrande (2016). The table shows that the results are very close, which validates the implementations developed in this study.

Analyzing the results in Table 6.1, it is observed that simplified methods tend to produce higher bending moment values, leading to a conservative approach in terms of safety. The Standard Column Method with approximate stiffness κ proved to be the most conservative among them. On the other hand, the Standard Column Method coupled with $M,N,1/r$ diagrams yielded results very close to those of the General Method. In contrast, the Semi-General Method showed less accuracy, producing results further from the General Method, mainly when creep effects were considered.

Table 6.2 presents a comparison between the results of the methods without creep effects and those including creep effects, allowing for an evaluation of the increase in bending moments due to the inclusion of this phenomenon.

Table 6.1 – Comparison between the results obtained by Casagrande (2016) and the developed program for Example 1.

Method	$M_{d,tot}$ **calculated by Casagrande (2016) [kNcm]**	$M_{d,tot}$ **calculated by the program [kNcm]**	**Percentage difference**
Methods without creep			
Standard Column with κ approximated	7119	7119	+ 0.00%
Standard Column coupled with $M,N,1/r$ diagrams	5947	5889	- 0.98%
Semi-General Method coupled with $M,N,1/r$ diagrams	6126	6167	+ 0.67%
General Method coupled with $M,N,1/r$ diagrams	5899	5962	+ 1.07%
Methods with creep			
Standard Column with κ approximated and additional eccentricity	7530	7468	- 0.82%
Standard Column coupled with $M,N,1/r$ diagrams with creep incorporated	7199	7281	+ 1.14%
Semi-General Method coupled with $M,N,1/r$ diagrams with creep incorporated	7474	7910	+ 5.83%
General Method coupled with $M,N,1/r$ diagrams with creep incorporated	7282	7284	+ 0.03%

Table 6.2 – Comparison between the results for Example 1 obtained by the program without and with creep effects.

Method	$M_{d,tot}$ **without creep [kNcm]**	$M_{d,tot}$ **with creep [kNcm]**	**Percentage difference**
Standard Column with κ approximated	7119	7468	+ 4.90%
Standard Column coupled with $M,N,1/r$ diagrams	5889	7281	+ 23.64%
Semi-General Method coupled with $M,N,1/r$ diagrams	6167	7910	+ 28.26%
General Method coupled with $M,N,1/r$ diagrams	5962	7284	+ 22.17%

From the results presented in the table, an increase of over 20% in bending moments is observed

due to the inclusion of creep effects. Given that the column has a slenderness ratio of $\lambda = 52$ in the analyzed direction, and considering that NBR 6118 (2023) mandates the consideration of creep effects only for columns with $\lambda > 90$, these results suggest that the current regulatory recommendation may be inadequate. In this specific case, creep effects should be considered according to EN 1992-1-1 (2004), since among the three conditions established by the Eurocode under which creep may be disregarded (as described in Chapter 4), the criterion related to first-order eccentricity is not satisfied.

Finally, Figure 6.10 presents a graphical comparison of the results obtained from the analyzed methods, considering creep effects. This includes the General Method coupled with $M, N, 1/r$ diagrams, with creep effects computed using the Kelvin-Voigt rheological model.

Figure 6.10 – Comparison of the maximum moment values obtained from the methods considering creep effects.

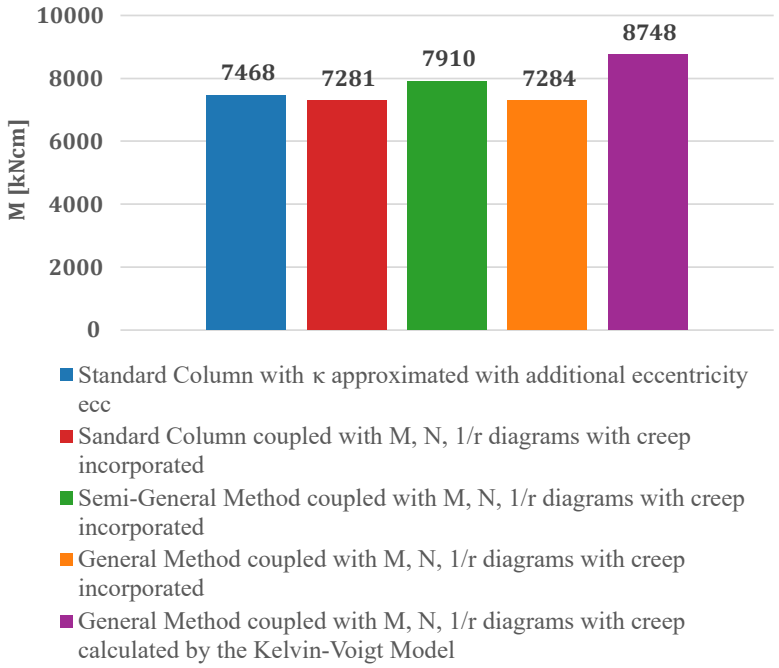

Analyzing the results in the figure, it is observed that the maximum bending moment obtained using creep effects computed via the Kelvin-Voigt model is significantly higher than that of the other methods, even exceeding the Semi-General Method by a considerable margin. It is approximately 20% greater than the General Method with $\varphi_{ef} = 1.18$. This result was expected due to the higher creep coefficients obtained, as illustrated in Figure 6.8.

6.3 EXAMPLE 2 - COLUMN SUBJECTED TO COMBINED BENDING WITH OPPOSITE FACE TENSION AT THE ENDS

The second example in this study reproduces Example 2 from Casagrande (2016). In this case, greater emphasis is placed on methods that account for creep effects, as this is a key focus of the present study. Among the methods that do not consider creep effects, only the General Method is analyzed in this example. Furthermore, the Semi-General Method is no longer considered, as it was deemed inefficient.

For the methods also analyzed by Casagrande (2016), a comparison of results is performed. In addition to the methods proposed by the author, the General Method with creep effects computed using the Kelvin-Voigt rheological model is also conducted. The analyzed methods are:

- The Standard Column Method with Approximate Stiffness κ considering creep effects through the additional eccentricity e_{cc} ,
- The Standard Column Method coupled with $M, N, 1/r$ diagrams considering creep effects through the extended stress-strain curve,
- The General Method coupled with $M, N, 1/r$ diagrams (without creep),
- The General Method coupled with $M, N, 1/r$ diagrams, considering creep effects through the extended stress-strain curve,
- The General Method coupled with $M, N, 1/r$ diagrams, considering creep effects through the extended stress-strain curve based on the Kelvin-Voigt rheological model.

The column in this example is based on the column from Example 1, but with its height modified to $\ell_e = 4.0\,\text{m}$. It is subjected to first-order bending moment diagrams, as illustrated in Figure 6.11b, in addition to a design axial force of $N_{Sd} = 2100\,\text{kN}$, as shown in Figure 6.11a.

The material properties are defined as follows:

- Concrete: $f_{ck} = 30\,\text{MPa}$;
- Steel: $f_{yk} = 500\,\text{MPa}$ and an elastic modulus of $E = 210\,\text{GPa}$;
- Creep coefficient: $\varphi = 2.0$.

With this modification in height, the slenderness ratio is given by

$$\lambda = \sqrt{12} \cdot \frac{\ell_e}{h} = \sqrt{12} \cdot \frac{400}{20} = 69. \tag{6.32}$$

To determine whether second-order effects should be considered, the parameters α_b, e_1 and λ_1 are evaluated. For this case, α_b is calculated as

Figure 6.11 – Initial data for Example 2.

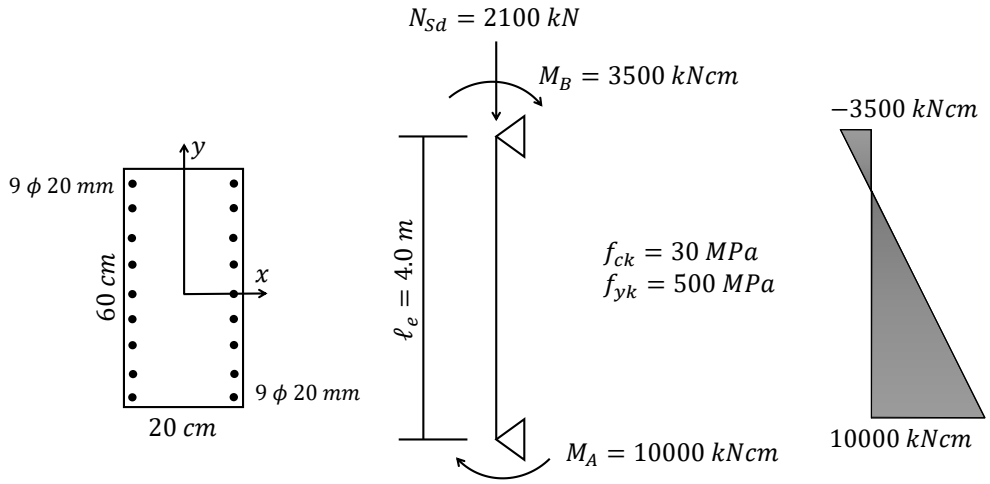

(a) Schematic drawing. (b) First-order bending moment diagram.

Adapted from Casagrande (2016).

$$\alpha_b = 0.6 + 0.4\frac{M_B}{M_A} = 0.6 + 0.4\frac{-3500}{10000} = 0.46 > 0.4. \tag{6.33}$$

The first-order eccentricity is obtained as

$$e_1 = \frac{10000}{2100} = 4.76\,\text{cm}. \tag{6.34}$$

The λ_1 parameter is then computed as

$$\lambda_1 = \frac{25 + 12.5(e_1/h)}{\alpha_b} = \frac{25 + 12.5\left(\frac{4.76}{20}\right)}{0.46} = 60.82 > 35 \therefore \lambda_1 = 60.82 \tag{6.35}$$

Since $\lambda_1 < \lambda < 90$, the column is moderately slender, meaning that second-order local effects can be evaluated using approximate methods based on the Standard Column approach. Furthermore, creep effects are not mandatory for this case, according to NBR 6118 (2023).

6.3.1 Standard Column Method with Approximate Stiffness κ and Additional Eccentricity e_{cc}

The total bending moment, $M_{d,tot}$, in the standard column method with approximate stiffness κ is determined directly using the parameters a, b and c, as described in Subsection 3.3.1.2. These parameters are computed as

$$\begin{cases} a = 5h = 5 \cdot 20 = 100, \\ b = h^2 N_d - \dfrac{N_d l_e^2}{320} - 5h\alpha_b M_{1d,A} = 20^2 \cdot 2100 - \frac{2100 \cdot 400^2}{320} - 5 \cdot 20 \cdot 0,46 \cdot 10000 = -670000, \\ c = -N_d h^2 \alpha_b M_{1d,A} = -2100 \cdot 20^2 \cdot 0,46 \cdot 10000 = -3.864 \times 10^9. \end{cases} \tag{6.36}$$

Thus, the total bending moment is computed using Eq. (3.40)

$$M_{d,tot} = \frac{-b + \sqrt{b^2 - 4ac}}{2a} = 10411\,\text{kN cm}. \tag{6.37}$$

Since this calculation directly applies formulas, the result is identical to that obtained by Casagrande (2016).

The additional creep-induced eccentricity is determined according to NBR 6118 (2023), using Eq. (4.15)

$$e_{cc} = \left(\frac{M_{sg}}{N_{sg}} + e_a\right)\left(2.718^{\frac{\varphi N_{sg}}{N_e - N_{sg}}} - 1\right). \tag{4.15}$$

As in the previous example, assuming that 25% of the total load corresponds to short-term effects, the sustained axial force is given by

$$N_{Sg} = 1237.5\,\text{kN}. \tag{6.38}$$

Next, the accidental eccentricity is computed as

$$\theta_1 = \frac{1}{100\sqrt{\ell_e}} = \frac{1}{100\sqrt{4.0}} = \frac{1}{200} = \theta_{1max} \tag{6.39}$$

$$e_a = \theta \cdot \frac{\ell_e}{2} = \frac{1}{200}\frac{400}{2} = 1.0\,\text{cm}. \tag{6.40}$$

The initial tangent modulus of elasticity of concrete, E_{ci}, is calculated as

$$E_{ci} = \alpha_E \cdot 5600\sqrt{f_{ck}} = 1,0 \cdot 5600\sqrt{30} = 30672\,\text{MPa} = 3067.2\,\text{kN/cm}^2. \tag{6.41}$$

The cross-section moment of inertia is obtained as

$$I_c = \frac{0.6 \cdot 0.2^3}{12} = 4 \times 10^{-4}\,\mathrm{m}^4 = 40 \times 10^3\,\mathrm{cm}^4. \tag{6.42}$$

Thus, the Euler critical load N_e is computed using Eq. (4.16)

$$N_e = \frac{10 E_{ci} I_c}{{\ell_e}^2} = \frac{10 \cdot 3067.2 \cdot 40 \times 10^3}{400^2} = 7668\,\mathrm{kN}. \tag{6.43}$$

Finally, the additional creep-induced eccentricity e_{cc} is determined as

$$e_{cc} = \left(\frac{2709.6}{1237.5} + 1.0\right)\left(2.718^{\frac{2 \cdot 1237.5}{7668 - 1237.5}} - 1\right) = 1.50\,\mathrm{cm}. \tag{6.44}$$

The additional bending moment M_{cc} is given by

$$M_{cc} = N_{Sd} \cdot e_{cc} = 2100 \cdot 1,50 = 3150\,\mathrm{kN\,cm}. \tag{6.45}$$

Thus, the total bending moment considering creep effects is obtained as

$$M_d = 10411 + 3150 = 13\,561\,\mathrm{kN\,cm}. \tag{6.46}$$

Casagrande (2016) obtained a total moment of 14 243 kN cm. Again, the discrepancy between the results arises from the author using the secant modulus of elasticity E_{cs} instead of the initial tangent modulus E_{ci}.

Based on this bending moment value, Casagrande (2016) carried out the reinforcement design for the cross-section. To compare the results, the same reinforcement configuration was adopted, consisting of two layers of 9 bars with a diameter of 20.00 mm, as illustrated in Figure 6.11a.

6.3.2 Standard Column Method Coupled with $M, N, 1/r$ Diagrams Considering Creep Effects Through the Extended Stress-Strain Curve

In this case, before constructing the $M, N, 1/r$ diagram, the stress-strain curve is shifted by the value of the creep coefficient. Following the approach adopted by Casagrande (2016), this study employs the same effective creep coefficient, $\varphi_{ef} = 1.18$, as determined in the previous example.

With the effective creep coefficient defined, the construction of the $M, N, 1/r$ diagrams proceeds, as illustrated in Figure 6.12.

Figure 6.12 – $M, N, 1/r$ diagrams for Example 2, with creep effects.

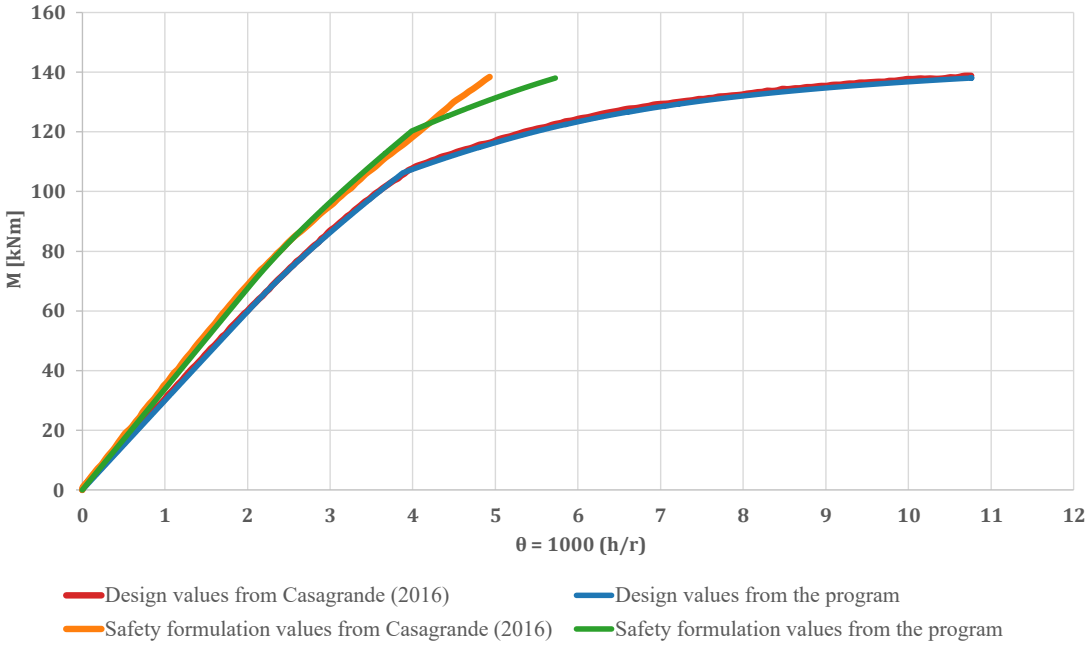

Similar to the previous example, the curves obtained by the computational program and those from Casagrande (2016), are perfectly aligned for the design values. However, a discrepancy is observed in the safety formulation, where a separation occurs in the final phase of the curves.

The dimensionless secant stiffness κ calculated by the program was 54.944, while Casagrande (2016) obtained 56.514. Finally, the program computed a final bending moment at the critical section of $M_{d,tot} = 10011\,\text{kN cm}$, whereas Casagrande (2016) obtained $M_{d,tot} = 10901\,\text{kN cm}$. Once again, this difference was anticipated, as it results from the divergence between the diagrams in the safety formulation.

6.3.3 General Method Coupled with $M, N, 1/r$ Diagrams (Without Creep)

In this case, the General Method is applied without considering creep effects in constructing the $M, N, 1/r$ diagrams. The $M, N, 1/r$ diagrams obtained are shown in Figure 6.13. For both formulations, the curves are almost perfectly aligned.

This method allows for determining bending moments at each node considered in the analysis. The entire moment distribution curve along the column height is illustrated in Figure 6.14. In this case, the results consistently converged along the entire column length.

Figure 6.13 – $M, N, 1/r$ diagrams for Example 2, without creep effects.

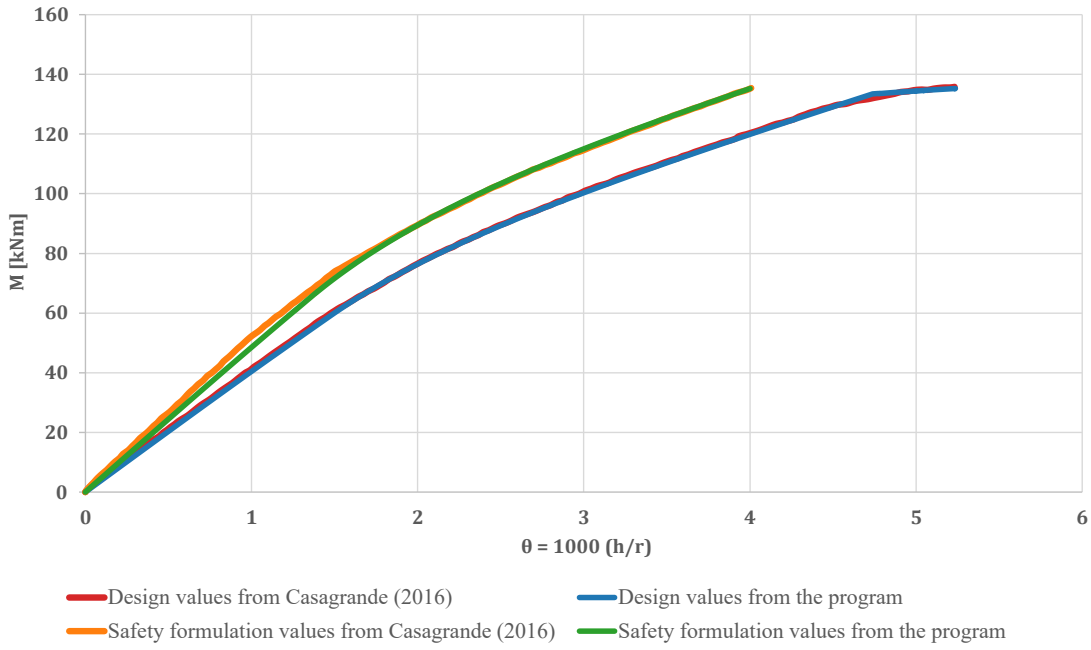

Figure 6.14 – Moment distribution diagram for Example 2, analyzed using the General Method without creep effects.

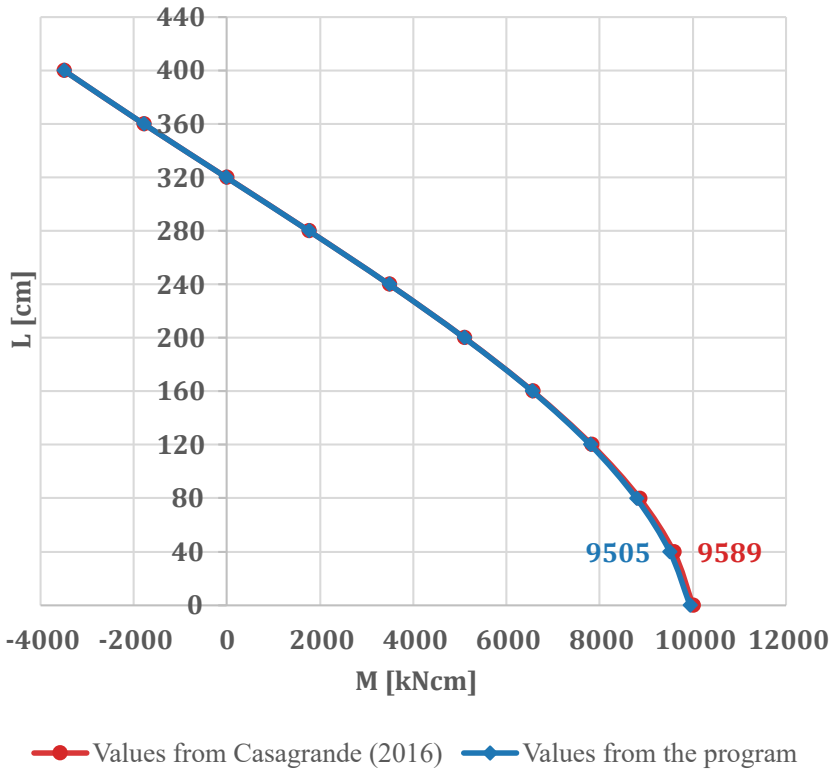

6.3.4 General Method Coupled with $M,N,1/r$ Diagrams Considering Creep Effects Through the Extended Stress-Strain Curve

The General Method is then applied with the $M,N,1/r$ diagrams, incorporating creep effects through the extended stress-strain curve in its formulation.

The complete moment distribution curve along the column height is presented in Figure 6.15. In this case, only minor discrepancies were observed in the results.

Figure 6.15 – Moment distribution diagram for Example 2, analyzed using the General Method with creep effects.

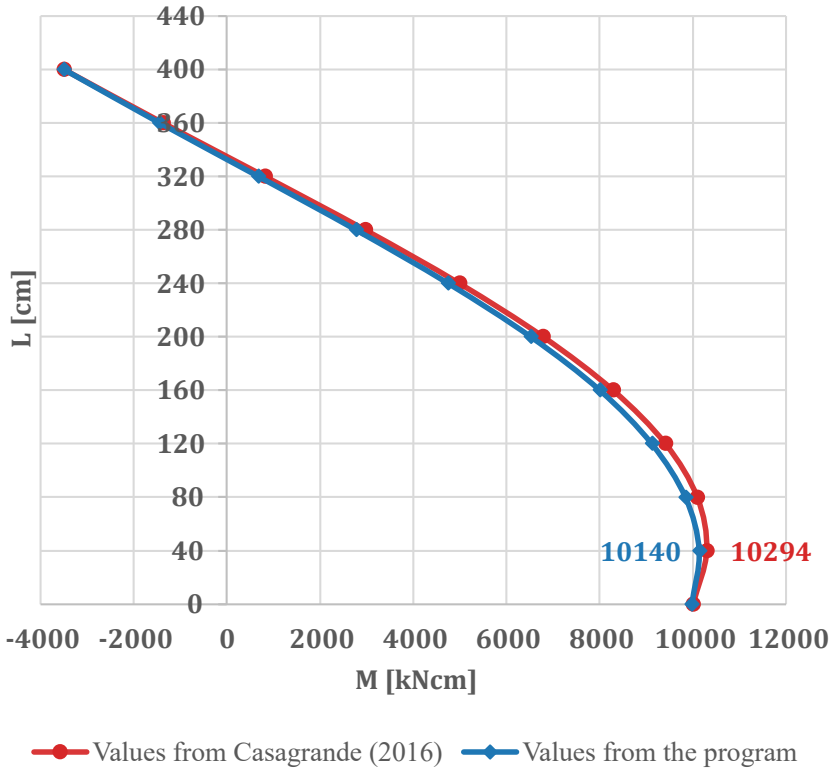

6.3.5 General Method Coupled with $M,N,1/r$ Diagrams Considering Creep Effects Through the Kelvin-Voigt Rheological Model

Finally, the General Method coupled with $M,N,1/r$ diagrams, but with creep effects computed using the Kelvin-Voigt rheological model is evaluated.

Applying this method, the creep coefficient φ_{KV}, obtained from the Kelvin-Voigt formulation at each node, can be determined. The distribution of these coefficients is shown in Figure 6.16.

The complete moment distribution curve along the column height is presented in Figure 6.17.

Figure 6.16 – Distribution of creep coefficients according to the Kelvin-Voigt Rheological Model for Example 2.

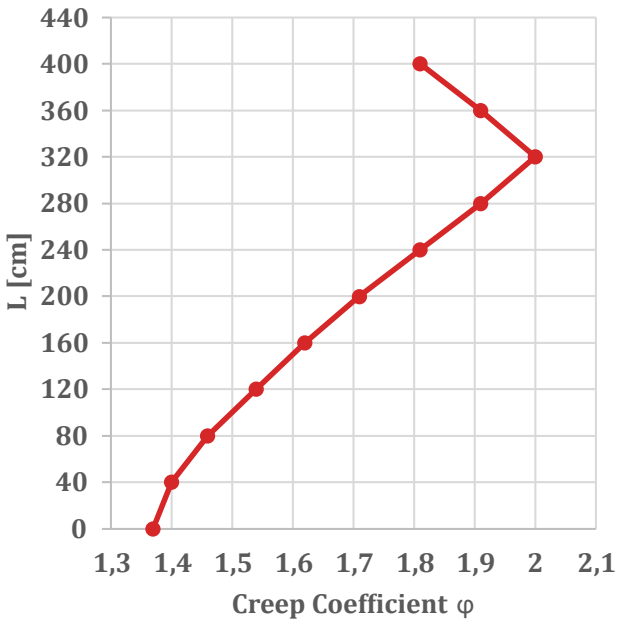

Figure 6.17 – Moment distribution diagram for Example 2, analyzed using the General Method with creep effects evaluated by the Kelvin-Voigt Rheological Model.

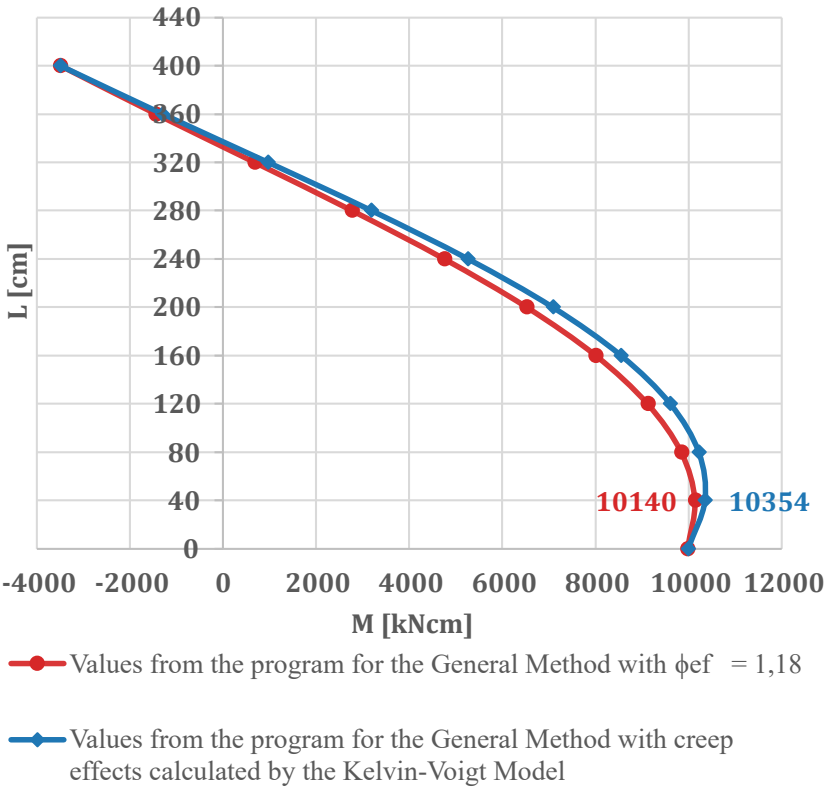

From Figure 6.16, it can be observed that the computed creep coefficients decrease as the bending moments in the nodes increase. Moreover, the magnitude of the obtained values is again significantly higher than the effective creep coefficient $\varphi_{ef} = 1.18$, used in the previous analyses.

Due to the higher creep coefficients obtained in this approach, the bending moments computed here are greater than those obtained in the previous General Method analysis. However, the difference is smaller than that observed in Example 1.

6.3.6 Comparison of Results

All results obtained were close to those reported by Casagrande (2016); therefore, this comparison will not be the primary focus of this analysis.

The evaluation of the General Method coupled with $M,N,1/r$ diagrams, both without and with creep consideration, revealed an increase in bending moments from $M_{d,tot} = 9508\,\text{kN cm}$ to $M_{d,tot} = 10\,140\,\text{kN cm}$. This represents a 6.65% increase, less significant than the increase observed in Example 1.

Table 6.3 presents a comparative analysis of the results obtained using different methods considering creep effects, showing the percentage difference relative to the General Method coupled with $M,N,1/r$ diagrams.

Table 6.3 – Comparison between different methods considering creep effects for Example 2.

Method	$M_{d,tot}$ **[kNcm]**	**Percentage difference**
Standard Column with κ approximated and additional eccentricity	13561	+ 33.74%
Standard Column coupled with $M,N,1/r$ diagrams with creep incorporated	10011	- 1.27%
General Method coupled with $M,N,1/r$ diagrams with creep incorporated	10140	–
General Method coupled with $M,N,1/r$ diagrams with creep calculated by the Kelvin-Voigt Model	10354	+ 2.11%

Analyzing the results in Table 6.3, it is observed that the Standard Column Method with approximate stiffness κ proved to be the most conservative method, as it resulted in significantly higher bending moments compared to the General Method. On the other hand, the Standard Column Method coupled with $M,N,1/r$ diagrams produced results very close to those of the General Method, even yielding slightly lower values.

Finally, the General Method with creep calculated using the Kelvin-Voigt model resulted in a bending moment closer to that obtained with the General Method using $\varphi_{ef} = 1.18$ than in the

previous example. Still, it remained more conservative than the reference method.

6.4 EXAMPLE 3 - COLUMN SUBJECTED TO COMBINED BENDING WITH SAME FACE TENSION AT THE ENDS

The third example in this study reproduces Example 3 from Casagrande (2016). As in the previous example, greater emphasis is given to methods considering creep effects. Among the methods that do not consider creep effects, only the General Method is analyzed in this case. Furthermore, the Standard Column Method with approximate stiffness κ and the Semi-General Method were no longer considered, as they were deemed, respectively, highly conservative and inefficient.

For the methods also analyzed by Casagrande (2016), a comparison of results is performed. In addition to the methods proposed by the author, the General Method coupled with $M,N,1/r$ diagrams with creep effects computed using the Kelvin-Voigt rheological model and the General Method coupled with $M,N,1/r$, using the new stress-strain diagram for nonlinear analysis introduced in NBR 6118 (2023), are also conducted. The analyzed methods are:

- The Standard Column Method coupled with $M,N,1/r$ diagrams considering creep effects through the extended stress-strain curve,
- The General Method coupled with $M,N,1/r$ diagrams (without creep),
- The General Method coupled with $M,N,1/r$ diagrams, considering creep effects through the extended stress-strain curve,
- The General method coupled with $M,N,1/r$ diagrams, considering creep effects through the extended stress-strain curve based on the Kelvin-Voigt rheological model,
- The General Method coupled with $M,N,1/r$ diagrams, using the stress-strain diagram for nonlinear analysis, considering creep effects through the extended stress-strain curve.

The column in this example is based on the column from the Example 1, with an equivalent length of $\ell_e = 3,0m$, but subjected to a first-order bending moment diagram, as illustrated in Figure 6.18b, in addition to a design axial force of $N_{Sd} = 2100\,\text{kN}$, as shown in Figure 6.18a.

The material properties are defined as follows:

- Concrete: $f_{ck} = 30\,\text{MPa}$;
- Steel: $f_{yk} = 500\,\text{MPa}$ and an elastic modulus of $E = 210\,\text{GPa}$;
- Creep coefficient: $\varphi = 2.0$.

The slenderness ratio is the same as in Example 1

Figure 6.18 – Initial data for Example 3.

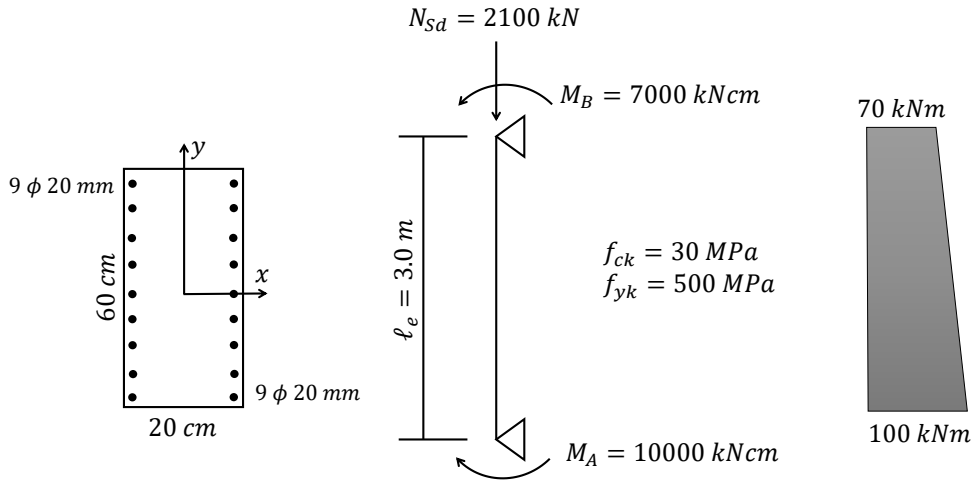

(a) Schematic drawing. (b) First-order bending moment diagram.

Adapted from Casagrande (2016).

$$\lambda = \sqrt{12} \cdot \frac{\ell_e}{h} = \sqrt{12} \cdot \frac{300}{20} = 52. \tag{6.47}$$

To determine whether second-order effects should be considered, the parameters α_b, e_1 and λ_1 are evaluated. For this case, α_b is calculated as

$$\alpha_b = 0.6 + 0.4\frac{M_B}{M_A} = 0.6 + 0.4\frac{7000}{10000} = 0.88 > 0.4. \tag{6.48}$$

The first-order eccentricity is obtained as

$$e_1 = \frac{10000}{2100} = 4.76\,\text{cm}. \tag{6.49}$$

The λ_1 parameter is then computed as

$$\lambda_1 = \frac{25 + 12.5(e_1/h)}{\alpha_b} = \frac{25 + 12.5\left(\frac{4.76}{20}\right)}{0.88} = 31.79 < 35 \therefore \lambda_1 = 35. \tag{6.50}$$

Since $\lambda_1 < \lambda < 90$, the column is moderately slender, meaning that second-order local effects can be evaluated using approximate methods based on the standard column approach. However, in this example, only more refined methods are considered. Furthermore, creep effects are not mandatory for this case, according to NBR 6118 (2023).

6.4.1 Standard Column Method Coupled with $M,N,1/r$ Diagrams Considering Creep Effects Through the Extended Stress-Strain Curve

In this case, before constructing the $M,N,1/r$ diagram, the stress-strain curve is shifted by the value of the creep coefficient. Following the approach adopted by Casagrande (2016), this study employs the same effective creep coefficient, $\varphi_{ef} = 1.18$, as determined in the first example.

With the effective creep coefficient defined, the construction of the $M,N,1/r$ diagrams proceeds. Since the cross-section and axial force remain unchanged, the diagrams obtained are identical to those from Example 2 (see Figure 6.12).

The dimensionless secant stiffness κ calculated by the program was also 54.944, while Casagrande (2016) obtained 56.514. Finally, for this example, the program computed a final bending moment at the most critical section of $M_{d,tot} = 12644\,\text{kN}\,\text{cm}$, whereas Casagrande (2016) obtained $M_{d,tot} = 13040\,\text{kN}\,\text{cm}$. Once again, this difference was expected, resulting from the discrepancies between the diagrams in the safety formulation.

6.4.2 General Method Coupled with $M,N,1/r$ Diagrams (Without Creep)

In this case, the General Method is applied without considering creep effects in constructing the $M,N,1/r$ diagrams. The $M,N,1/r$ diagrams obtained are identical to those from Example 2 (see Figure 6.13).

This method allows for determining bending moments at each node considered in the analysis. The entire moment distribution curve along the column height is illustrated in Figure 6.19.

Due to the differences in the moment-curvature relationships discussed earlier, the results exhibited slight variations. Furthermore, as observed in Figure 6.19, the critical nodes in each analysis are not the same. However, it can be noted that the bending moments at heights of 90 cm and 120 cm are very close in both curves.

6.4.3 General Method Coupled with $M,N,1/r$ Diagrams Considering Creep Effects Through the Extended Stress-Strain Curve

The General Method is then applied with the $M,N,1/r$ diagrams, incorporating creep effects through the extended stress-strain curve in its formulation.

The complete moment distribution curve along the column height is presented in Figure 6.20. Once more, due to the differences in the moment-curvature relationships, the results showed slight variations.

Figure 6.19 – Moment distribution diagram for Example 3, analyzed using the General Method without creep effects.

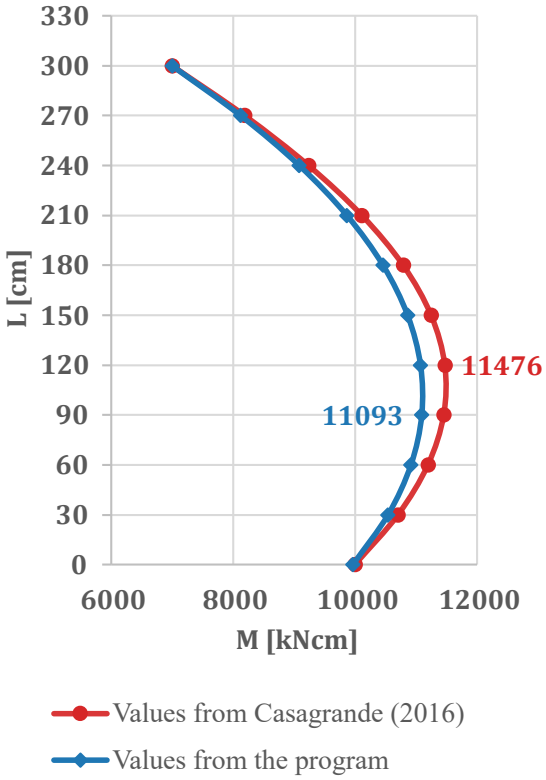

Figure 6.20 – Moment distribution diagram for Example 3, analyzed using the General Method with creep effects.

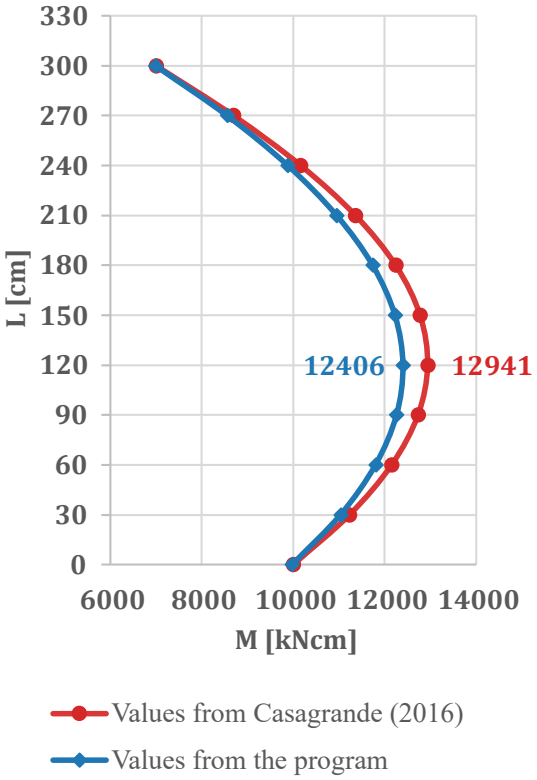

6.4.4 General Method Coupled with $M,N,1/r$ Diagrams Considering Creep Effects Through the Kelvin-Voigt Rheological Model

The General Method coupled with $M,N,1/r$ diagrams, but with creep effects computed using the Kelvin-Voigt rheological model is evaluated.

Applying this method, the creep coefficient φ_{KV}, obtained from the Kelvin-Voigt formulation at each analysis node, can be determined. The distribution of these coefficients is shown in Figure 6.21.

Again, from Figure 6.21, it can be observed that the computed creep coefficients decrease as the bending moments in the nodes increase. Moreover, the magnitude of the obtained values remains significantly higher than the effective creep coefficient $\varphi_{ef} = 1.18$, used in the previous analyses.

The complete moment distribution curve along the column height is presented in Figure 6.22. Despite the higher creep coefficients obtained in this approach, the bending moments computed here are close those obtained in the previous General Method analysis. This result indicates

better convergence between this method and the General Method across all analyzed examples.

Figure 6.21 – Distribution of creep coefficients according to the Kelvin-Voigt Rheological Model for Example 3.

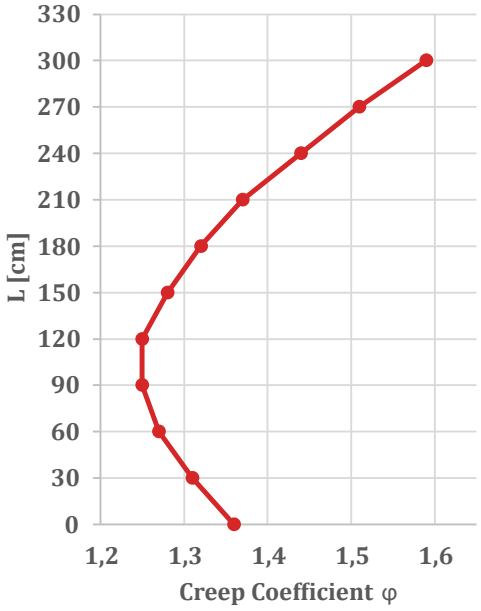

Figure 6.22 – Moment distribution diagram for Example 3, analyzed using the General Method with creep effects evaluated by the Kelvin-Voigt Rheological Model.

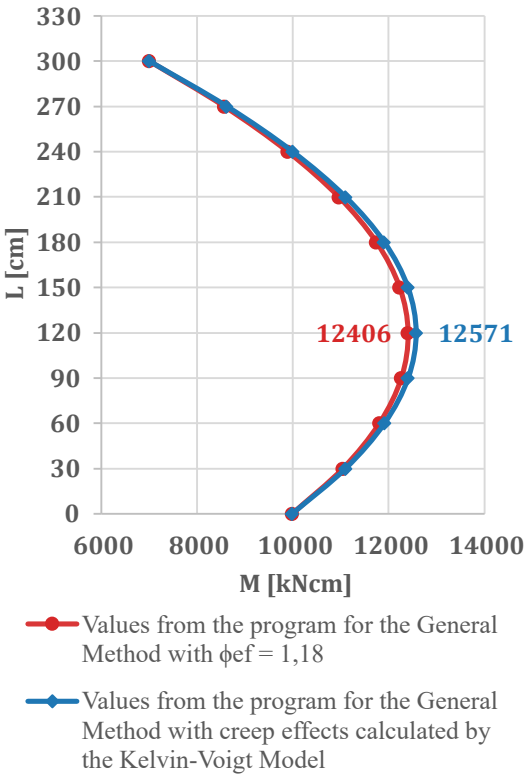

6.4.5 General Method Coupled with $M,N,1/r$ Diagrams Using the Stress-Strain Diagram for Nonlinear Analysis and Considering Creep Effects Through the Extended Stress-Strain Curve

Finally, the General Method was tested using the stress-strain diagram for nonlinear analysis (diagram from Eq. 3.7 – Figure 3.2) in constructing $M,N,1/r$ diagrams.

In this case, for simplicity, only the diagram for safety formulation was constructed, as illustrated in Figure 6.23, where the obtained curve can be compared with those derived from the idealized curve-rectangle stress-strain diagram (diagram from Eq. 3.1 – Figure 3.1), obtained both by the program and by Casagrande (2016). Analyzing the figure, it can be observed that the newly obtained curve is considerably stiffer than those obtained previously.

Applying the General Method, the moment distribution along the column height is obtained, as shown in Figure 6.24.

Figure 6.23 – $M,N,1/r$ diagrams for safety formulation for Example 3, with creep effects.

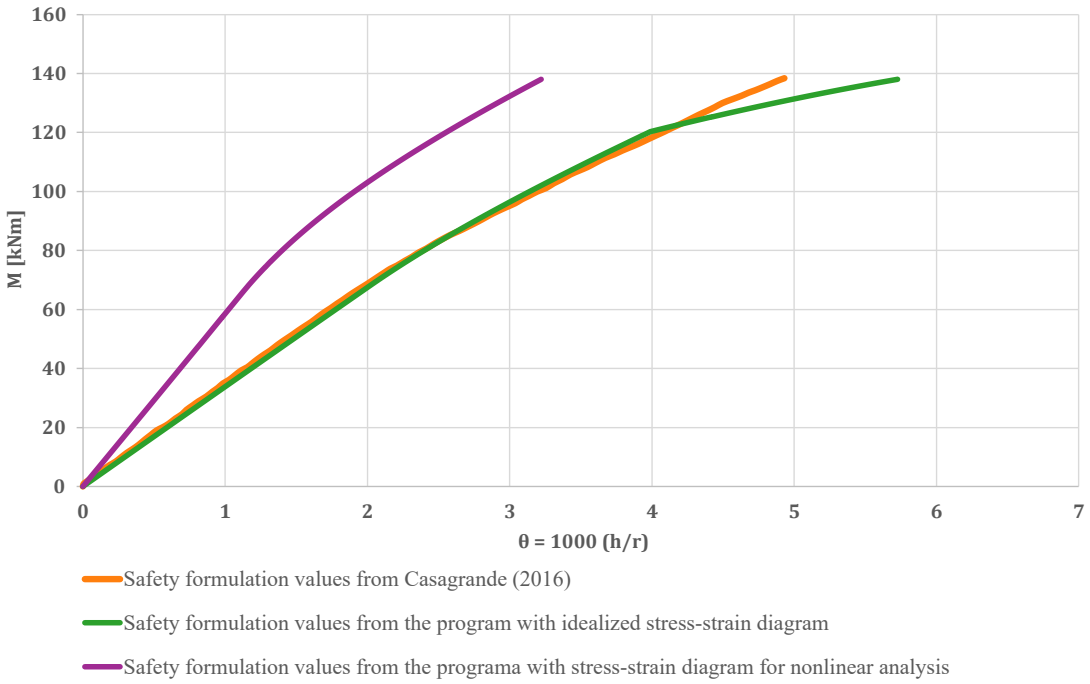

Figure 6.24 – Moment distribution diagram for Example 3, analyzed using the General Method coupled with $M,N,1/r$ using the stress-strain for nonlinear analysis with creep effects.

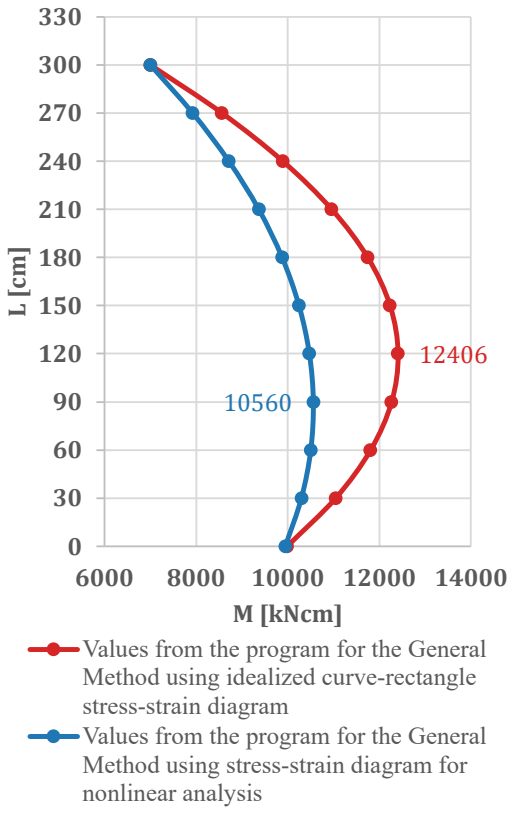

Comparing the curves, it becomes evident that the bending moments obtained are significantly lower than those computed using the General Method coupled with $M,N,1/r$ diagrams which employed the idealized curve-rectangle stress-strain diagram.

6.4.6 Comparison of Results

All results obtained for the same methods applied by Casagrande (2016) were closely aligned with those reported by the author.

The evaluation of the General Method coupled with $M,N,1/r$ diagrams, both without and with creep consideration, revealed an increase in bending moments from $M_{d,tot} = 11093\,\text{kN cm}$ to $M_{d,tot} = 12406\,\text{kN cm}$. This represents a 11.8% increase, which is considered significant. However, NBR 6118 (2023) does not mandate the consideration of creep effects for columns with this slenderness ratio.

Table 6.4 presents a comparative analysis of the results obtained using different methods that account for creep effects, showing the percentage difference relative to the General Method coupled with $M,N,1/r$ diagrams.

Table 6.4 – Comparison between different methods considering creep effects for Example 3.

Method	$M_{d,tot}$ **[kNcm]**	**Percentage difference**
Standard Column coupled with $M,N,1/r$ diagrams with creep incorporated	12644	+ 1.92%
General Method coupled with $M,N,1/r$ diagrams with creep incorporated	12406	–
General Method coupled with $M,N,1/r$ diagrams with creep calculated by the Kelvin-Voigt Model	12571	+ 1.33%
General Method coupled with $M,N,1/r$ diagrams using stress-strain for nonlinear analysis with creep incorporated	10560	- 14.88%

Analyzing the results in Table 6.4, it is observed that the Standard Column Method coupled with $M,N,1/r$ diagrams produced results very close to those of the General Method. Similarly, the General Method with creep calculated using the Kelvin-Voigt model also resulted in a moment value very close to that of the General Method with $\varphi_{ef} = 1.18$.

The most significant discrepancy, as previously noted, was observed in the General Method coupled with $M,N,1/r$ constructed using the stress-strain diagram for nonlinear analysis (diagram from Eq. 3.7 – Figure 3.2), which resulted in substantially lower bending moment values compared to other methods. This may indicate that this stress-strain diagram for nonlinear analysis is unsuitable for this application, or that using the idealized curve-rectangle stress-strain

diagram leads to overly conservative results. Determining which model is the most accurate still requires experimental validation.

6.5 EXAMPLE 4 - COLUMN SUBJECTED TO COMBINED BENDING WITH OPPOSITE FACE TENSION AT THE ENDS AND VARYING SLENDERNESS RATIO

The final example was initially based on the study by Pastore (2020); however, several modifications were made. In her research, the author conducted a comparative analysis of 9.720 simulations, varying multiple parameters such as cross-section dimensions, slenderness ratio, reinforcement ratio, axial force, bending moments, the angle of moment application (as the author studied biaxial bending), and the consideration or omission of creep effects.

A simplified version of this approach is adopted for the present example, where variations in calculation methods and slenderness values (by altering the column length) are introduced while maintaining the same cross-section, axial force and initial moments. The methods analyzed in this case are:

- The Standard Column Method coupled with $M, N, 1/r$ diagrams considering creep effects through the extended stress-strain curve,
- The General Method coupled with $M, N, 1/r$ diagrams (without creep),
- The General Method coupled with $M, N, 1/r$ diagrams, considering creep effects through the extended stress-strain curve.

The cross-section considered is the same as in the previous examples $(20 \times 60)\text{cm}^2$, while the column height is varied for each case analyzed. The reinforcement ratio was set at $\rho = 4\%$, resulting in a reinforcement area of $A_s = 24\,\text{cm}^2$ on each face, as illustrated in Figure 6.25a. The number of reinforcement bars was not specified to correspond to standard commercial diameters; instead, the exact calculated reinforcement area was used in the implementation.

The columns were subjected to an axial force of $N_{Sd} = 900\,\text{kN}$ and bending moments, where the minimum moment was applied at one end, while a moment twice as large was applied at the other end, creating tension on the opposite face, as illustrated in Figure 6.25b. The minimum moment is calculated as

$$M_{1d,min} = N_{Sd}(0.015 + 0.03h) = 900(0.015 + 0.03 \cdot 0.2) = 18.9\,\text{kN m}$$
$$\therefore M_{1d,min} = 1890\,\text{kN cm}. \quad (6.51)$$

Figure 6.25 – Initial data for Example 4.

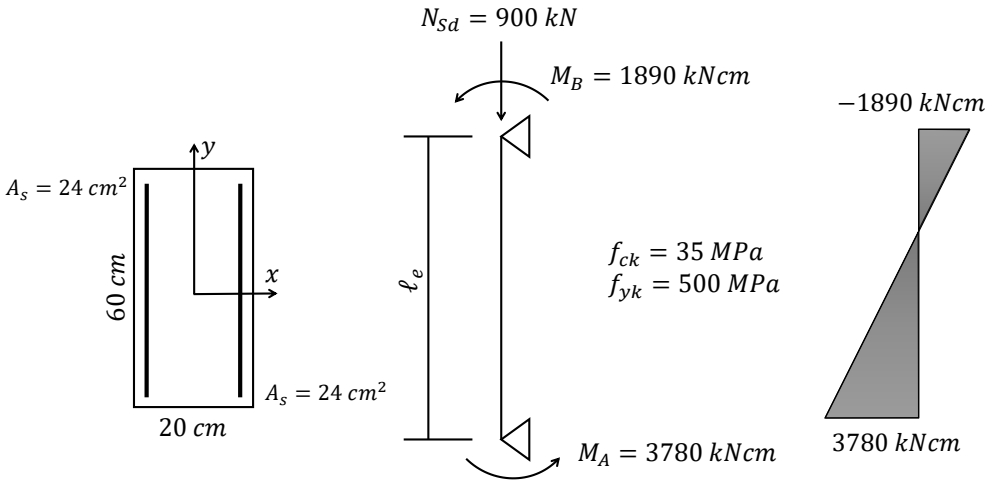

(a) Schematic drawing. (b) First-order bending moment diagram.

The material properties are defined as follows:

- Concrete: $f_{ck} = 35\,\text{MPa}$;
- Steel: $f_{yk} = 500\,\text{MPa}$ and an elastic modulus of $E = 210\,\text{GPa}$;
- Creep coefficient: $\varphi = 2.0$.

To determine whether second-order effects should be considered, the parameters α_b, e_1 and λ_1 are evaluated. For this case, α_b is calculated as

$$\alpha_b = 0.6 + 0.4\frac{M_B}{M_A} = 0.6 + 0.4\frac{-1890}{3780} = 0.4. \tag{6.52}$$

The first-order eccentricity is computed as

$$e_1 = \frac{3780}{900} = 4.2\,\text{cm}. \tag{6.53}$$

The λ_1 parameter is then determined as

$$\lambda_1 = \frac{25 + 12.5(e_1/h)}{\alpha_b} = \frac{25 + 12.5\left(\frac{4.2}{20}\right)}{0.4} = 69 > 35 \therefore \lambda_1 = 69. \tag{6.54}$$

The slenderness ratios analyzed were defined based on Pastore (2020) and the column classification presented in Subsection 3.2.3, approximating the values to multiples of 40 to ensure the same discretization for all cases:

- $\ell_e = 400\,\text{cm}$: $\lambda = \lambda_1 = 69$
- $\ell_e = 520\,\text{cm}$: $\lambda = 90$
- $\ell_e = 680\,\text{cm}$: $\lambda = 118$
- $\ell_e = 840\,\text{cm}$: $\lambda = 145$

Pastore (2020) considered the characteristic value of the creep coefficient φ in her study. However, as previously discussed, the effective creep coefficient $\varphi_{ef} = 1.18$ is used in this analysis.

6.5.1 Case 1: $\lambda = \lambda_1 = 69$

In this case, the column has a length of 400 cm and a slenderness ratio of $\lambda = \lambda_1 = 69$, which represents the threshold between short and moderately slender columns. According to NBR 6118 (2023), for short columns, local second-order effects can be neglected, whereas for moderately slender columns, these effects can be evaluated using approximate methods based on the Standard Column approach.

For this example, these approximate methods based on the Standard Column approach, such as the Standard Column with approximate stiffness κ, are not considered. Instead, the Standard Column coupled with $M, N, 1/r$ diagrams with creep incorporated is applied directly.

6.5.1.1 Standard Column Method Coupled with $M, N, 1/r$ Diagrams Considering Creep Effects Through the Extended Stress-Strain Curve

As previously described, the application of this method begins with the construction of $M, N, 1/r$ diagrams. The diagram constructed for this column is shown in Figure 6.26.

Figure 6.26 – $M, N, 1/r$ diagrams obtained by the program for Example 4 with creep effects.

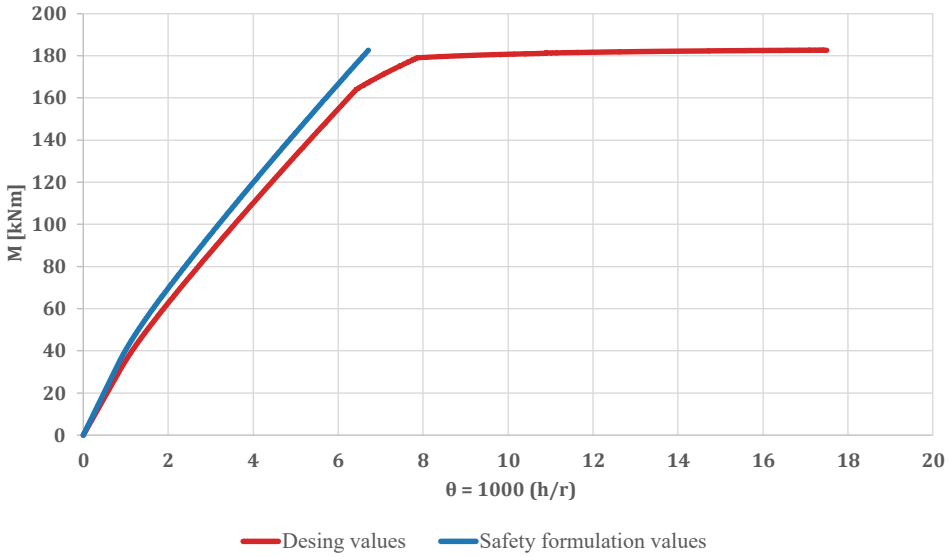

It is important to highlight that this diagram applies to all cases analyzed with creep for this example and, for all cases, the same stiffness value of $\kappa = 46.30$ can be used.

For this first case, the program computed a final bending moment at the critical section of $M_{d,tot} = 1978\,\text{kN}\,\text{cm}$.

6.5.1.2 General Method Coupled with $M,N,1/r$ Diagrams (Without Creep)

The application of this method also begins with the construction of $M,N,1/r$ diagrams. The diagram constructed for this column, without creep effects, is shown in Figure 6.27.

Figure 6.27 – $M,N,1/r$ diagrams obtained by the program for Example 4 without creep effects.

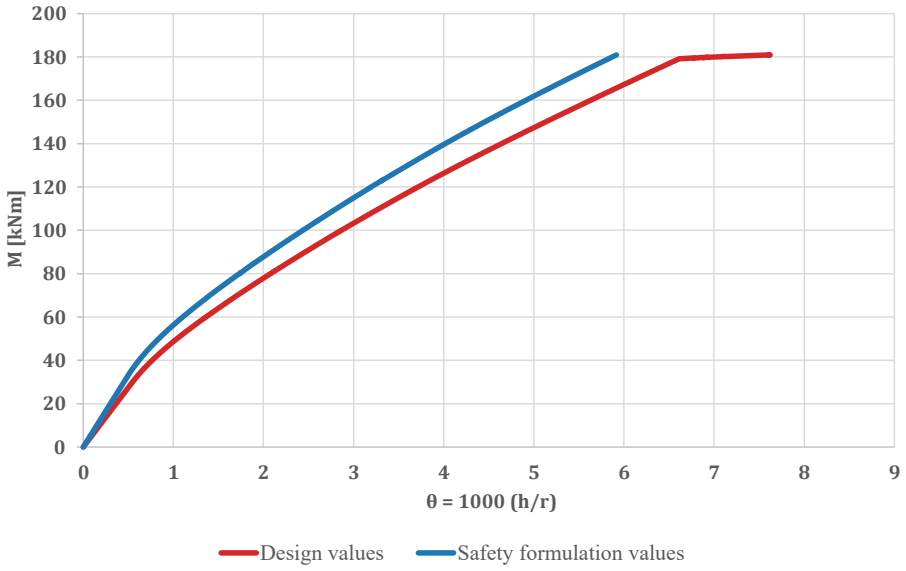

It is important to note that this diagram applies to all cases analyzed without creep for this example.

The moment distribution curve along the column height is shown in Figure 6.28.

6.5.1.3 General Method Coupled with $M,N,1/r$ Diagrams Considering Creep Effects Through the Extended Stress-Strain Curve

Finally, this method also begins with constructing the $M,N,1/r$ diagrams, obtaining the same diagram presented in Figure 6.26. The complete moment distribution along the column height is shown in Figure 6.28

Figure 6.28 – Moment distribution diagrams for the Case 1 of Example 4, analyzed using different methods.

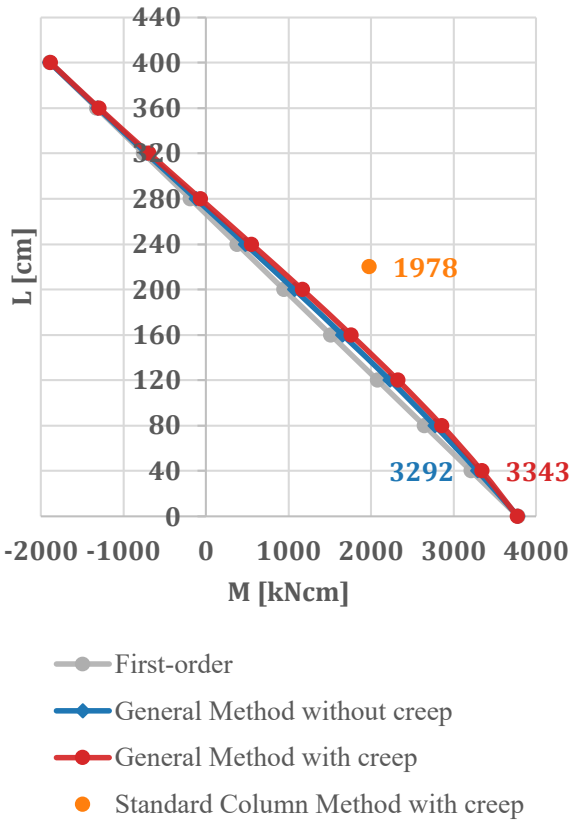

6.5.2 Case 2: $\lambda = 90$

In this case, the column has a length of 520 cm and a slenderness ratio of $\lambda = 90$, representing the threshold between moderately slender columns and slender columns. For this slenderness ratio, the calculation of local second-order effects is mandatory. Additionally, from this value onward, it becomes compulsory that the analysis be conducted at least using the Standard Column Method coupled with $M, N, 1/r$ diagrams and that creep effects must be considered.

6.5.2.1 Standard Column Method Coupled with $M, N, 1/r$ Diagrams Considering Creep Effects Through the Extended Stress-Strain Curve

As previously described, the application of this method begins with the construction of $M, N, 1/r$ diagrams. The diagram constructed for this column is identical to the one from the previous case, presented in Figure 6.26.

For this second case, the program computed a final bending moment at the critical section of $M_{d,tot} = 2513\,\text{kN cm}$.

6.5.2.2 General Method Coupled with $M, N, 1/r$ Diagrams (Without Creep)

The $M, N, 1/r$ diagram constructed for this column, without creep effects, is shown in Figure 6.27. The moment distribution curve along the column height is shown in Figure 6.29.

6.5.2.3 General Method Coupled with $M, N, 1/r$ Diagrams Considering Creep Effects Through the Extended Stress-Strain Curve

For this case, the same $M, N, 1/r$ diagram with creep effects is obtained (see Figure 6.26). The complete moment distribution along the column height is shown in Figure 6.29.

Figure 6.29 – Moment distribution diagrams for the Case 2 of Example 4, analyzed using different methods.

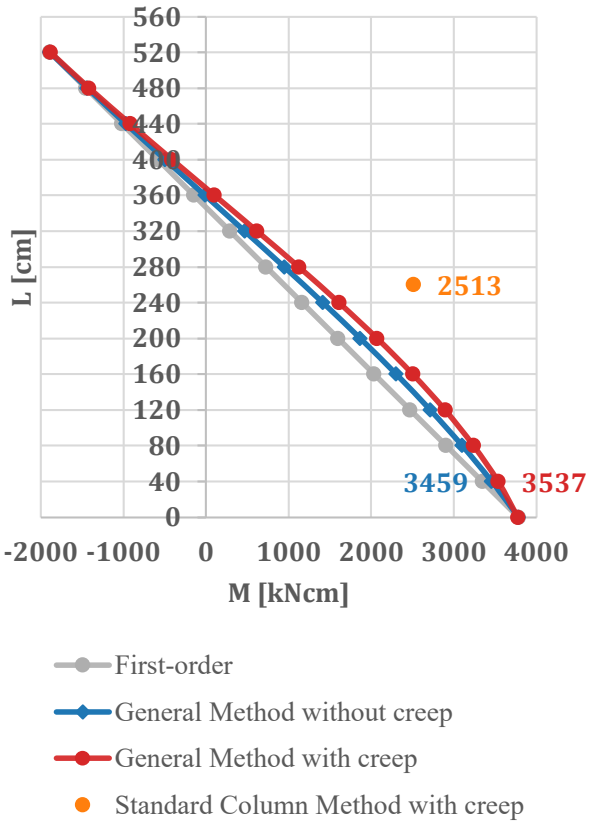

6.5.3 Case 3: $\lambda = 118$

In this case, the column has a length of 680 cm and a slenderness ratio of $\lambda = 118$, representing an intermediate value within the range for columns classified as slender. For this slenderness ratio, the calculation of second-order effects is mandatory and, as in the previous case, it is required that the analysis be conducted at least using the Standard Column Method coupled with $M, N, 1/r$ diagrams while also considering creep effects.

6.5.3.1 Standard Column Method Coupled with $M,N,1/r$ Diagrams Considering Creep Effects Through the Extended Stress-Strain Curve

The $M,N,1/r$ diagram constructed for this column is identical to the one from the previous cases, presented in Figure 6.26. For this case, the program computed a final bending moment at the critical section of $M_{d,tot} = 4740\,\text{kN}\,\text{cm}$.

6.5.3.2 General Method Coupled with $M,N,1/r$ Diagrams (Without Creep)

The $M,N,1/r$ diagram constructed for this column, without creep effects, is shown in Figure 6.27. The moment distribution curve along the column height is shown in Figure 6.30.

6.5.3.3 General Method Coupled with $M,N,1/r$ Diagrams Considering Creep Effects Through the Extended Stress-Strain Curve

For this case, the same $M,N,1/r$ diagram with creep effects is obtained (see Figure 6.26). The complete moment distribution along the column height is shown in Figure 6.30

Figure 6.30 – Moment distribution diagrams for the Case 3 of Example 4, analyzed using different methods.

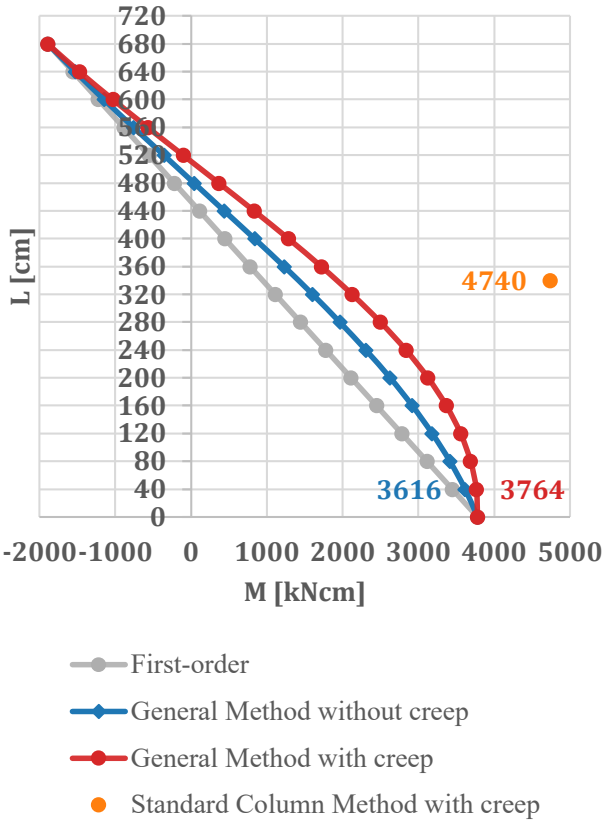

6.5.4 Case 4: $\lambda = 145$

In this case, the column has a length of 840 cm, more than twice the length of the first analyzed case, and a slenderness ratio of $\lambda = 145$. This slenderness ratio value is slightly above the lower limit of the range for very slender columns. For this case, the calculation of second-order effects is mandatory, and the analysis must be conducted using the General Method while also considering creep effects.

6.5.4.1 Standard Column Method Coupled with $M,N,1/r$ Diagrams Considering Creep Effects Through the Extended Stress-Strain Curve

The $M,N,1/r$ diagram constructed for this column is identical to the one from the previous cases and is presented in Figure 6.26.

According to NBR 6118 (2023), this method is not applicable to the analysis of this column, as the slenderness exceeds the limit of $\lambda > 140$. For this case, the program computed a final bending moment at the critical section of $M_{d,tot} = -38\,615\,\text{kN cm}$, clearly demonstrating the complete inadequacy of this method for columns with such high slenderness.

6.5.4.2 General Method Coupled with $M,N,1/r$ Diagrams (Without Creep)

The $M,N,1/r$ diagram constructed for this column, without creep effects, is shown in Figure 6.27. The moment distribution curve along the column height is shown in Figure 6.31.

6.5.4.3 General Method Coupled with $M,N,1/r$ Diagrams Considering Creep Effects Through the Extended Stress-Strain Curve

For this case, the same $M,N,1/r$ diagram with creep effects is obtained (see Figure 6.26). The complete moment distribution along the column height is shown in Figure 6.31

The increase in bending moments due to second-order effects, particularly when considering creep, is significantly greater than in the other cases, resulting in higher intermediate moments than those at the ends.

Figure 6.31 – Moment distribution diagrams for the Case 4 of Example 4, analyzed using different methods.

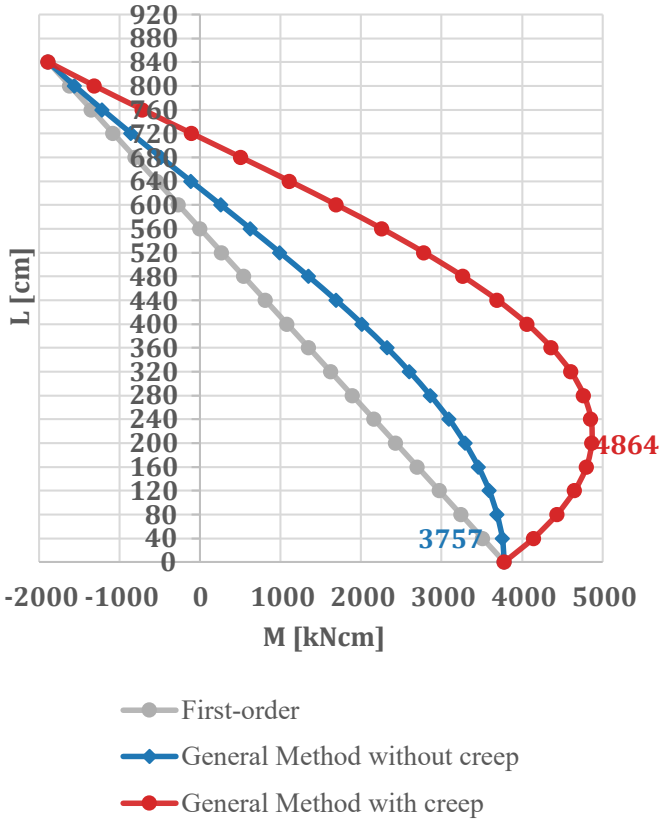

6.5.5 Comparison of Results

Initially, the results for each case are compared in Table 6.5, which presents the percentage difference of the Standard Column Method relative to the General Method, both considering creep effects in the construction of the $M, N, 1/r$ diagrams.

Analyzing the results presented in Table 6.5, it is evident that the Standard Column Method coupled with $M, N, 1/r$ diagrams yielded poor results, even for lower slenderness values. In the first two cases, it produced significantly lower results than the General Method, which could represent a potential risk in structural design. These results may indicate that certain inherent simplifications in the Standard Column Method are unsuitable for this example. Furthermore, in Case 3, the Standard Column Method became highly conservative. Finally, in Case 4, where NBR 6118 (2023) does not permit the use of this method, it produced completely unrealistic results, confirming that it is inapplicable for very slender columns.

Table 6.6 presents the percentage increase in bending moments due to creep effects, comparing the largest internal moment values in each application of the General Method coupled with $M, N, 1/r$.

Table 6.5 – Comparison between different methods considering creep effects – maximum internal bending moments for Example 4.

Cases	**Methods**	$M_{d,tot}$ **[kNcm]**	**Percentage Difference**
Case 1	**Standard Column Method**	1978	- 40.83%
$\lambda = 69$	**General Method**	3343	-
Case 2	**Standard Column Method**	2513	- 28.95%
$\lambda = 90$	**General Method**	3537	-
Case 3	**Standard Column Method**	4740	+ 25.93%
$\lambda = 118$	**General Method**	3764	-
Case 4	**Standard Column Method**	-38615	- 893.89%
$\lambda = 145$	**General Method**	4864	-

Table 6.6 – Comparison of maximum internal bending moments for the General Method with and without creep effects – Example 4.

Cases	$M_{d,tot}$ **without creep [kNcm]**	$M_{d,tot}$ **with creep [kNcm]**	**Percentage Difference**
Case 1 $\lambda = 69$	3292	3343	+ 1.55%
Case 2 $\lambda = 90$	3459	3537	+ 2.25%
Case 3 $\lambda = 118$	3616	3764	+ 4.09%
Case 4 $\lambda = 145$	3757	4864	+ 29.46%

The analysis of Table 6.6 aligns with expectations and observations from the moment distribution diagrams: the greater the slenderness ratio, the more significant the impact of creep effects.

In this example, considering creep effects in the analysis becomes indispensable, especially for very slender columns. However, the other examples produced in this study, showed that for different loading conditions, creep effects can become essential even for lower slenderness ratios, particularly in cases where bending moments at both ends tension the same face.

7 CONCLUSIONS

The present study aimed to conduct a comparative analysis of different strategies for creep simulation in calculating second-order effects in reinforced concrete columns. Given the significant influence of time-dependent deformations on the structural behavior of slender elements, accurately modeling creep effects is essential to ensure the safety and serviceability of concrete structures.

Various methods were evaluated throughout this research, highlighting their advantages and limitations in predicting long-term displacements and internal force redistribution. The results contribute to the ongoing discussion regarding the reliability of different creep models and emphasize the importance of considering these effects in nonlinear structural analysis.

The analysis of different columns with varying slenderness ratios confirmed the expected trends, demonstrating that the higher the slenderness, the more pronounced the creep effects, making their consideration crucial in structural analysis. Additionally, it was observed that creep effects are more significant when the applied moments induce tension on the same face, leading to more pronounced second-order moments. This occurs because, when the column is subjected to moments that cause tension on opposite faces, the displacements and the moment values in the intermediate cross-sections are reduced due to the reversal of effects. However, when the moments act tensioning the same face, the entire length of the column is subjected to high displacement and moment values. Consequently, it was found that considering creep effects can be essential even for columns with slenderness ratios lower than 90, especially in these cases where moments act on the same face. This result aligns with findings from previous studies, such as those by Casagrande (2016) and Pastore (2020), both of whom recommend considering creep effects even for lower slenderness ratios. Casagrande (2016), in particular, highlights the imprudence of the Brazilian standard regarding creep, as it only provides the most simplified approach – the Approximate Method of Additional Eccentricity (e_{cc}) – and employs a simplified and non-conservative criterion for creep consideration when compared to EN 1992-1-1 (2004) provisions.

The comparison between different methods confirmed that, as expected, simplified approaches tend to be more conservative; however this is not a general rule and may vary depending on the specific case and modeling assumptions. The *Standard Column Method with approximate stiffness κ and additional eccentricity (e_{cc})* proved to be applicable and valuable for quick manual calculations but may yield overly conservative results.

The *Standard Column Method coupled with $M,N,1/r$ diagrams* emerged as an intermediate

approach that is generally efficient. However, it performed poorly in Example 4, requiring further scrutiny. This method considers geometric nonlinearity approximately and accounts for physical nonlinearity through stiffness values obtained from constructed $M, N, 1/r$ diagrams. Due to the complexity of generating these diagrams, the method is not trivial to apply, making it feasible for practical use but demanding careful assessment in specific cases.

Conversely, the *Semi-General Method coupled with $M, N, 1/r$ diagrams* proved inefficient and unsuitable for practical design applications. Despite its complexity, given the need to construct $M, N, 1/r$ diagrams, it still resulted in overly conservative predictions.

The *General Method coupled with $M, N, 1/r$ diagrams*, on the other hand, demonstrated robust performance, though it requires computational implementation, adding a certain degree of complexity. However, once implemented, it provides results that fully account for physical and geometric nonlinearity within seconds when analyzing isolated columns. Nevertheless, its complete validation should be performed through comparisons with experimental results, which were not undertaken in this study.

A method proposed in this study consists of the *General Method coupled with $M, N, 1/r$ diagrams and creep effects modeled using the Kelvin-Voigt rheological model*. This method appears promising, as it yielded comparatively poor results for the first example but provided satisfactory outcomes for Examples 2 and 3. However, the model parameters may not have been well-calibrated in this application. Further research is needed to refine this approach, mainly through experimental data to define the model parameters. An interesting feature of this method is that it allows calculating a specific creep coefficient value for each discretization node, based on its specific current stress.

Finally, the *General Method coupled with $M, N, 1/r$ diagrams based on the new stress-strain diagram for nonlinear analysis introduced in NBR 6118 (2023)* produced moment values significantly lower than the other methods. In this preliminary analysis, it was observed that NBR 6118 (2023) does not explicitly address the use of this diagram for constructing $M, N, 1/r$ diagrams, nor for considering creep effects. The standard only specifies its application in nonlinear analysis. On the other hand, EN 1992-1-1 (2004) explicitly incorporates this diagram for shifting the stress-strain curve to account for creep effects. Additionally, the formulation used to compute the creep coefficient in the Eurocode differs from that adopted in NBR 6118 (2023), which may contribute to discrepancies in the estimated creep effects. Further in-depth studies on this subject are recommended.

Examining how creep effects were incorporated in these methodologies, it was observed that all methods coupled with $M, N, 1/r$ diagrams accounted for creep by shifting the stress-strain diagram. This approach appears to yield reliable results and is widely adopted internationally,

despite not being explicitly included in the Brazilian standard. However, multiple variations of this method exist, depending on the choice of stress-strain diagrams, the formulation used to compute the creep coefficient, and whether the characteristic or effective creep coefficient is considered. Regarding this last aspect, using the effective creep coefficient seems more appropriate and is widely recognized in the literature, as permanent loads should induce creep effects.

Regarding creep coefficients, a comparison between values obtained from the Kelvin-Voigt rheological model and those calculated according to NBR 6118 (2023) revealed significant discrepancies. As previously discussed, the Kelvin-Voigt model used in this study requires better validation through comparisons with experimental results. Additionally, the formulation for creep coefficient calculation in NBR 6118 (2023) is based on the CEB-FIP (1978) approach. However, as noted by Mola and Pellegrini (2012), this international code has undergone at least two updates regarding creep coefficient computation, indicating that the Brazilian standard should revise this topic and possibly update its formulation.

7.1 SUGGESTIONS FOR FUTURE RESEARCH

Several research directions can be explored based on this study to further advance scientific knowledge in this field. Initially, it is suggested that future studies investigate these methods under a broader range of model characteristics, such as varying cross-section geometries, reinforcement configurations, and multi-story column systems. Additionally, columns with $f_{ck} > 50\,\text{MPa}$ should be analyzed, as high-strength concrete requires specific considerations, particularly in its nonlinear stress-strain behavior. Furthermore, a global structural analysis that considers creep effects holistically across the structure is recommended.

Refined methodologies should also be implemented. One promising approach is the development of methods that incorporate time-dependent behavior in more detail, considering the timing of incremental load applications. Alternative rheological models should be further investigated, particularly Boltzmann's and Kelvin-Voigt's models, which are the most used ones for concrete in the literature. Additionally, exploring new creep models and incorporating shrinkage effects could provide a more comprehensive analysis, as shrinkage effects evolve over time and influence long-term deformations. A model that integrates both creep and shrinkage could enhance the accuracy of structural predictions.

Another recommended study is a comparative analysis that applies a single method – such as the General Method coupled with $M, N, 1/r$ diagrams incorporating creep effects via the extended stress-strain curve – using different creep coefficient formulation from European, American, and Brazilian standards, as well as other formulations found in the literature (see Almeida (2006)).

Finally, it is crucial to emphasize the need for experimental research on creep, particularly in reinforced concrete columns. This study has identified a significant gap in the literature regarding experimental validation, which, if addressed, could lead to considerable advancements in the field. However, this remains challenging, as experimental creep testing is inherently complex and time-consuming.

Bibliography

ALMEIDA, L. C. de. *Identificação de parâmetros estruturais com emprego de análise inversa*. Doctoral Thesis — Universidade Estadual de Campinas, Campinas, SP, Brasil, 2006.

ARAúJO, J. M. d. *Pilares esbeltos de concreto armado*: Algoritmos para análise e dimensionamento. Rio Grande: Editora da furg, 1993.

ARGYRIS, J.; DOLTSINIS, I. S.; SILVA, V. D. da. Constitutive modeling and computation of non-linear viscoelastic solids. part i: Rheological models and numerical integration techniques. *Computer Methods in Applied Mechanics and Engineering*, v. 88, n. 2, p. 135–163, 1991.

ASSOCIAÇÃO BRASILEIRA DE NORMAS TÉCNICAS. *NBR 6118*: Projeto de estruturas de concreto. Rio de Janeiro, 2023. 242 p.

BALLIM, Y.; FANOURAKIS, G. C. Predicting creep deformation of concrete: A comparison of results from different investigations. Proceedings, 11th FIG Symposium on Deformation Measurements. Santorini, Greece, 2003.

BECHO, J. dos S. *Método dos Elementos Finitos Posicional em análise viscoelástica: Elementos de pórtico com cinemática de Reissner*. Doctoral Thesis — Universidade Federal de Minas Gerais, Belo Horizonte, MG, Brasil, 2020.

BORGES, A. C. L. *Análise de pilares esbeltos de concreto armado solicitados a flexo-compressão oblíqua*. Master's Thesis — Escola de Engenharia de São Carlos - Universidade de São Paulo, São Paulo, SP, Brasil, 1999.

CARREIRA, J. D.; BURG, R. G. Testing for concrete creep and shrinkage. *The Adam Neville Symposium: Creep and Shrinkage of Concrete - structural design effects*, Farmington Hills, Michigan, USA, p. 381–420, 2000. Apud Oliveira (2011).

CARVALHO, R. C.; PINHEIRO, L. M. *Cálculo e detalhamento de estruturas usuais de concreto armado*. São Paulo: Pini, 2009. v. 2. ISBN 978-85-7266-188-1.

CASAGRANDE, A. F. *Consideração da fluência no cálculo dos efeitos de segunda ordem em pilares de concreto armado*. Master's Thesis — Universidade Federal de Santa Catarina, Florianópolis, SC, Brasil, 2016.

CASTRO, L. M. S. *Análise de vigas em fundação elástica*. Lisboa: [s.n.], 2001.

Comité Européen du Béton - Fédération Internationale de la Précontrainte. *CEB-FIP Model Code for Concrete Structures*. Paris, 1978. Apud Mola and Pellegrini (2012).

EUROPEAN COMMITTEE FOR STANDARDIZATION. *Eurocode 2*: Design of concrete structures - part 1-1: General rules and rules for buildings. [S.l.], 2004. 225 p.

Fédération Internationale du Béton (fib). *fib Model Code for Concrete Structures 2010*. Lausanne, 2012. (fib Bulletin 66). Apud Mola and Pellegrini (2012).

FUSCO, P. B. *Estruturas de concreto - Solicitações normais*. [S.l.]: Guanabara Dois S.A., 1981.

HANSEN, T. C. Creep of concrete. *Bulletin No. 33*, Swedish Cement and Concrete Research Institute: Stockholm, 1958. Apud Neville, Dilger and Brooks (1983).

HANSEN, T. C.; MATTOCK, A. H. The influence of size and shape of member on the shrinkage and creep of concrete. *Journal of the American Concrete Institute*, p. 267–90, 1966. Apud Neville (2016).

HOLANDA, R. M.; SILVA, S. F. da. Método das diferenças finitas aplicado à flambagem de colunas. *Revista de Engenharia e Tecnologia*, v. 13, n. 4, 2021. ISSN 2176-7270.

Instituto Nacional de Meteorologia (INMET). *Banco de Dados Meteoroógicos do INMET*. 2025. Acessed on: 20 de fevereiro de 2024. Disponível em: <https://bdmep.inmet.gov.br/#>.

KALINTZIS, C. A. A. *Estudo da fluência do concreto de elevado desempenho*. Master's Thesis — Escola Politécnica, Universidade de São Paulo, São Paulo, SP, Brasil, 2000. Apud Kataoka (2010).

KATAOKA, L. T. *Análise da deformabilidade por fluência e retração e sua utilização na monitoração de pilares de concreto*. Doctoral Thesis — Universidade de São Paulo, São Paulo, SP, Brasil, 2010.

KIMURA, A. *Informática aplicada a estruturas de concreto armado*. 2. ed. São Paulo: Oficina de Textos, 2018. ISBN 978-85-7975-310-7.

L'HERMITE, R. Volume changes of concrete. *Proceedings of 4th International Symposium on the Chemistry of Cement*, Washington DC, USA, p. 659–94, 1960. Apud Neville (2016).

MARTHA, L. F. *Análise de estruturas*: Conceitos e métodos básicos. 2. ed. Rio de Janeiro: Elsevier, 2017. ISBN 978-85-532-8625-0.

MEHTA, P. K.; MONTEIRO, P. J. M. *Concreto*: Microestrutura, propriedades e materiais. 3. ed. São Paulo: IBRACON, 2008. ISBN 978-85-98576-12-1.

MOLA, F.; PELLEGRINI, L. M. The new model for creep of concrete in fip model code 2010. *37th Conference on OUR WORLD IN CONCRETE & STRUCTURES*, Singapore, 2012.

NEVILLE, A. M. Non-elastic deformations in concrete structures. *New Zealand Engineering*, Gainesville, Florida, USA, v. 12, p. 114–20, 1957. Apud Neville (2016).

NEVILLE, A. M. The influence of cement on creep of concrete in mortar. *Journal of the Prestressed Concrete Institute*, Gainesville, Florida, USA, p. 12–18, 1958. Apud Neville (2016).

NEVILLE, A. M. Role of cement in the creep of mortar. *Journal of the American Concrete Institute*, v. 55, p. 963–84, 1959. Apud Neville (2016).

NEVILLE, A. M. Tests on the influence of the properties of cement on the creep of the mortar. *RILEM Bull*, n. 4, p. 5–17, 1959. Apud Neville (2016).

NEVILLE, A. M. The relation between creep of concrete and the stress-strength ratio. *Applied Scientific Research*, The Hague, v. 9, p. 285–92, 1960. Apud Neville (2016).

NEVILLE, A. M. Creep of concrete as a function of its cement paste content. *Magazine of Concrete Research*, v. 16, n. 46, p. 21–30, 1964. Apud Neville (2016).

NEVILLE, A. M. *Creep of Concrete: plain, and prestressed*: plain, and prestressed. Amsterdam: North-Holland, 1970. Apud Neville (2016).

NEVILLE, A. M. *Properties of Concrete*. 5. ed. England: Pearson, 2011. ISBN 978-0-273-75580-7.

NEVILLE, A. M. *Propriedades do Concreto*. 5. ed. Porto Alegre: Bookman, 2016. ISBN 978-85-8260-366-6.

NEVILLE, A. M.; DILGER, W. H.; BROOKS, J. J. *Creep of plain and structural concrete*. New York: Construction Press, 1983. ISBN 0-86095-834-5.

NEVILLE, A. M.; KENINGTON, H. W. Creep of aluminous cement concrete. *Proceedings of the 4th International Symposium on the Chemistry of Cement*, p. 703–8, 1960. Apud Neville (2016).

NEVILLE, A. M.; STAUNTON, M. M.; BONN, M. A study of the relation between creep and the gain of strength of concrete. *Symposium on Structure of Portland Cement Paste and Concrete*, Washington DC, USA, n. 90, p. 186–203, 1966. Apud Neville (2016).

OLIVEIRA, H. L. *Modelos numéricos aplicados à análise viscoelástica linear e à otimização topológica probabilística de estruturas bidimensionais*. Doctoral Thesis — Universidade de São Paulo, São Carlos, SP, Brasil, 2017.

OLIVEIRA, R. *Análise teórica e experimental de estruturas planas de concreto armado com a consideração da fluência*. Doctoral Thesis — Universidade de São Paulo, São Paulo, SP, Brasil, 2011.

PASTORE, M. F. *Análise de pilares esbeltos de concreto armado de seção retangular submetidos à flexão coposta oblíqua*. Master's Thesis — Universidade de São Paulo, São Carlos, SP, Brasil, 2020.

PAULA, J. A. de. *Algoritmos para o estudo de pilares esbeltos de concreto armado solicitados a flexão normal composta*. Master's Thesis — Universidade de São Paulo, São Carlos, SP, Brasil, 1988.

QUAST, U. Verfahrensgerechte berücksichtigung des kriechens bei programmgesteuerter berechnung schlanker stahlbetonstützen. *Der Bauingenieur*, v. 53, n. 2, p. 41–42, 1978. Apud Casagrande (2016).

RIBEIRO, K. *Diagramas para verificação de pilares retangulares em concreto armado submetidos à flexão composta normal*. Master's Thesis — Universidade Federal de Santa Catarina, Florianópolis, SC, Brasil, 2011.

RUGGIERO, M. A. G.; LOPES, V. L. d. R. *Cálculo Numérico*: Aspectos teóricos e computacionais. 2. ed. São Paulo: Pearson, 1996. ISBN 978-85-346-0204-4.

RÜSCH, H. *Concreto armado e protendido*: propriedades dos materiais e dimensionamento. Rio de Janeiro, RJ, Brasil: Campus, 1981. Apud Kataoka (2010).

RÜSCH, H.; KORDINA, K.; HILSDORF, H. Der einfluss des mineralogischen charakters der zuschläge auf das kriechen von beton. *Deustscher Ausschuss für Stahlbeton*, Berlin, n. 146, p. 19–113, 1963. Apud Neville (2016).

RUSSELL, H. G. Performance of shrinkage-compensating concrete in slabs. *Research and Development Bulletin*, 1978. Apud Neville (2016).

Sá, M. F. *Comportamento mecânico e estrutural de FRP*: Elementos pultudidos de gfrp. Master's Thesis — Universidade Técnica de Lisboa, Lisboa, Portugal, 2007. Apud Becho (2020).

SCADELAI, M. A. *Dimensionamento de pilares de acordo com a NBR6118:2003*. Master's Thesis — Escola de Engenharia de São Carlos - Universidade de São Paulo, São Paulo, SP, Brasil, 2004.

SOUZA, L. A. F. de. Modelagem numérica computacional de viga de concreto armado com acoplamento de teorias. *Vetor*, Rio Grande, v. 22, n. 2, p. 43–58, 2012.

THURSTON, R. H. *Materials of construction*. New York: John Wiley, 1895. Apud Becho (2020).

TROXELL, G. E.; RAPHAEL, J. M.; DAVIS, R. E. Long-time creep and shrinkage tests of plain and reinforced concrete. *Proceedings, American Society for Testing and Materials*, v. 58, p. 1101–20, 1958. Apud Neville (2011).

WASSIN, R. *Étude fiabiliste du fluage des structures en béton armé et précontraint*. Doctoral Thesis — Ecole Centrale de Paris, Paris, 2002.

WESTERBERG, B. *Time-dependent effects in the analysis and design of slender concrete compression members*. Doctoral Thesis — Instituto Real de Tecnologia, Estocolmo, 2008.

YUE, L. L.; TAERWE, L. Creep recovery of plain concrete and its mathematical modeling. *Magazine of Concrete Research*, v. 44, n. 161, p. 281–90, 1992. Apud Neville (2011).

APPENDIX A – EVALUATION OF THE CREEP COEFFICIENT φ: COMPARISON BETWEEN TABULATED DATA IN NBR 6118 (2023) AND THE DETAILED CALCULATION PROCEDURE

This appendix presents a comparative study between the creep coefficient values shown in Table A.1, which were extracted from the table provided in NBR 6118 (2023), and those obtained using the detailed calculation procedure outlined in the same standard.

As highlighted in Subsection 4.1.1, for elements subjected to stresses below 0,5 f_c and when high precision is not required, $\varphi(t_\infty, t_0)$ can be approximately obtained through linear interpolation using Table A.1. This table, presents creep coefficient values as a function of the average ambient humidity and the fictitious thickness of the element h_{fic}, calculated using Eq. 2.2. The values apply to concrete temperatures ranging from 10 °C to 20 °C; however the standard allows their use for temperatures between 0 °C and 40 °C. These values are intended for concrete produced with ordinary Portland cement.

Table A.1 – Upper characteristic values of the creep coefficient $\varphi(t_\infty, t_0)$. Same as Table 4.1.

Average Ambient Humidity (%)			40		55		75		90	
Fictitious Thickness (cm) $2A_c/u$			20	60	20	60	20	60	20	60
$\varphi(t_\infty, t_0)$ Concrete Classes C20 to C45	t_0 **days**	5	4.6	3.8	3.9	3.3	2.8	2.4	2.0	1.9
		30	3.4	3.0	2.9	2.6	2.2	2.0	1.6	1.5
		60	2.9	2.7	2.5	2.3	1.9	1.8	1.4	1.4
$\varphi(t_\infty, t_0)$ Concrete Classes C50 to C90		5	2.7	2.4	2.4	2.1	1.9	1.8	1.6	1.5
		30	2.0	1.8	1.7	1.6	1.4	1.3	1.1	1.1
		60	1.7	1.6	1.5	1.4	1.2	1.2	1.0	1.0

Adapted from NBR 6118 (2023).

However, NBR 6118 (2023) does not explicitly state the origin of these values. Therefore, this comparative study was conducted by recalculating the values in this table according to the detailed calculation procedure also outlined in Subsection 4.1.1.

A.1 VERIFICATION OF TABULATED VALUES THROUGH DETAILED CALCULATION

To reproduce the table values, the detailed calculation procedure was implemented in *SMath Solver*, a free computer algebra system (CAS) designed for symbolic and numerical computations, with a user-friendly interface similar to engineering notebooks.

The average ambient humidity (U), fictitious thickness (h_{fic}), and initial loading time (t_0) were varied for specific temperature values (T). The formulation considered ordinary Portland cement ($\alpha = 2$, as defined in Subsection 4.1.1) and a slump range of 5 to 9 cm to allow the use of the equation provided in the notes of Table 4.2 for calculating φ_{1c}. This study was limited to concretes with compressive strength $f_{ck} < 50\,\text{MPa}$.

The Brazilian standard states that the table was developed for temperature values between 10 °C and 20 °C. However, the formulation requires a specific temperature value. Simulations were performed for temperatures of 10 °C, 15 °C, and 20 °C. Only minor variations were observed between the results at these different temperatures, but the values obtained for $T = 10\,°\text{C}$ were closest to those in Table A.1. These computed values are presented in Table A.2.

Table A.2 – Creep coefficient $\varphi(t_\infty, t_0)$ values obtained using the detailed calculation procedure for $T = 10\,°\text{C}$.

Average Ambient Humidity (%)			40		55		75		90	
Fictitious Thickness (cm) $2A_c/u$			20	60	20	60	20	60	20	60
$\varphi(t_\infty, t_0)$ Concrete Classes C20 to C45	t_0 **days**	5	4.4	3.8	3.8	3.2	2.7	2.4	1.9	1.8
		30	3.1	2.9	2.6	2.5	2.0	1.9	1.5	3.5
		60	2.6	2.6	2.3	2.3	1.7	1.8	1.4	2.7

The percentage difference between the values in Table A.2 and those in Table A.1 is shown in Table A.3.

Table A.3 – Percentage difference between the values in Table A.2 and those in Table A.1.

Average Ambient Humidity (%)		40		55		75		90	
Fictitious Thickness (cm)		20	60	20	60	20	60	20	60
t_0 **days**	5	-3.4%	+0.3%	-3.8%	-2.0%	-2.9%	-0.0%	-3.9%	-4.4%
	30	-8.4%	-2.9%	-9.1%	-4.9%	-10.9%	-6.0%	-8.9%	+135.6%
	60	-8.8%	-1.9%	-9.7%	-1.6%	-8.5%	-1.4%	-2.2%	+95.1%

In general, the values converged well for a fictitious thickness of 60 cm, particularly for an initial loading time of $t_0 = 5$ days. However, significant discrepancies were found for an ambient humidity of 90%, a fictitious thickness of 60 cm, and initial loading time of $t_0 = 30$ and 60 days. Overall, the computed values were lower, aligning with the standard's statement that the table values represent upper characteristic values, ensuring a conservative approach. However, in the cases with high discrepancies at 90% humidity, the computed values were higher, potentially leading to underestimated structural designs.

It is not possible to precisely determine the causes of these discrepancies, as the methodology used by the standard to define the values in Table A.1 is not explicitly provided. Nevertheless, caution is recommended when using these values, particularly for an ambient humidity of 90%. For other conditions, the variations in results were minor, making the table values generally conservative.

A.2 EVALUATION OF THE TABLE FOR BRAZILIAN ENVIRONMENTAL CONDITIONS

According to INMET (2025), the average temperature in Belo Horizonte in 2024 was approximately 23 °C, with some Brazilain cities experiencing even higher temperatures.

Table A.1 is specified in NBR 6118 (2023) as being applicable to temperatures between 10 °C and 20 °C, though the standard allows its use for temperatures ranging from 0 °C and 40 °C. However, results obtained using the formulation at 25 °C, presented in Table A.4, indicate grater discrepancies. The percentage differences, shown in Table A.5, reveal deviation of up to 20% even for humidity levels below or equal to 75%.

Table A.4 – Creep coefficient $\varphi(t_\infty, t_0)$ values obtained using the detailed calculation procedure for $T = 25\,°C$.

Average Ambient Humidity (%)			40		55		75		90	
Fictitious Thickness (cm) $2A_c/u$			20	60	20	60	20	60	20	60
$\varphi(t_\infty, t_0)$ Concrete Classes C20 to C45	t_0 **days**	5	4.2	3.6	3.5	3.1	2.6	2.3	1.9	1.7
		30	2.7	2.7	2.3	2.3	1.8	1.8	1.4	2.7
		60	2.3	2.4	2.0	2.1	1.6	1.7	1.3	3.2

Thus, it is evident that more precise calculation methods are essential when determining creep coefficients, particularly for higher ambient temperatures, as commonly found in Brazil. The table values must be used with extreme caution for humidities of 90%, as significant discrepancies were observed.

Table A.5 – Percentage difference between the values in Table A.4 and those in Table A.1.

U (%)		40		55		75		90	
$h_{\mathbf{fic}}$ **(cm)**		20	60	20	60	20	60	20	60
t_0 **days**	5	-9.7%	-4.6%	-9.8%	-6.5%	-7.9%	-3.7%	-7.4%	-9.6%
	30	-19.6%	-10.1%	-19.7%	-11.4%	-19.0%	-10.2%	-13.3%	+81.2%
	60	-21.8%	-10.1%	-21.9%	-9.1%	-18.0%	-6.6%	-7.5%	+127.3%

For other conditions, the variations were less pronounced, making the tabulated values generally conservative. However, more refined calculation procedures should be preferred whenever greater accuracy is required.

APPENDIX B – DERIVATION OF CURVATURE EXPRESSIONS USING THE FINITE DIFFERENCE METHOD

This appendix presents the mathematical derivation of the curvature expressions used in the Finite Difference Method, specifically Eqs. (5.83) to (5.85). The derivation follows the displacement assumptions and the coordinate system definition established in Figure B.1.

Figure B.1 – Coordinate system origin for each case. Same as Figure 5.10.

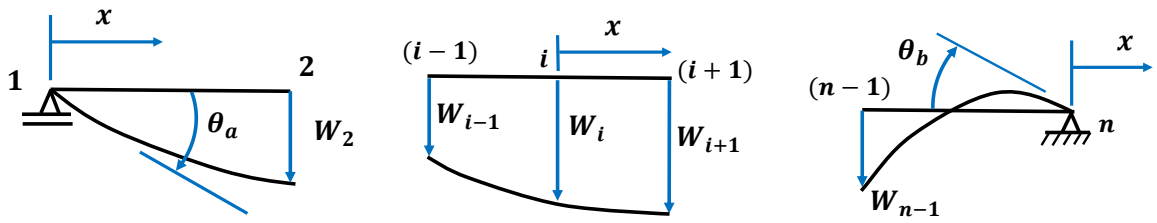

(a) Case A: support on the left. (b) Case B: intermediate nodes. (c) Case C: support on the right.

Adapted from Araújo (1993).

To provide a comprehensive approach, the expressions are derived using two different methodologies:

1. Quadratic Polynomial Approximation: a second-degree polynomial function is fitted to the displacement field, allowing for an explicit expression for curvature in terms of nodal displacements;
2. Taylor Series Expansion: the function is expanded using a Taylor series, which provides an alternative finite difference approximation for the second derivative (curvature).

Both approaches lead to the same final expressions, reinforcing the validity of the adopted formulation.

B.1 QUADRATIC POLYNOMIAL APPROXIMATION

The derivation begins with the definition of a second-degree polynomial to describe the elastic line equation (deflection equation):

$$W(x) = a_0 + a_1 x + a_2 x^2. \tag{B.1}$$

From this expression, its derivatives are obtained, which correspond, respectively, to the rotation equation (W') and the curvature equation (W'')

$$W'(x) = a_1 + 2a_2x, \tag{B.2}$$

$$W''(x) = 2a_2. \tag{B.3}$$

Using these expressions, each case's boundary conditions are evaluated, as illustrated in Figure B.1.

a) Case A: Support on the Left
As illustrated in Figure B.1a, the deflection at the support is zero, thus

$$W(0) = 0 \quad \therefore \quad a_0 = 0. \tag{B.4}$$

The rotation at the support is equal to θ_a

$$W'(0) = \theta_a \quad \therefore \quad a_1 = \theta_a. \tag{B.5}$$

The deflection at node 2 ($x = \Delta l$) is defined as W_2, which allows solving for a_2

$$W(\Delta l) = W_2 \quad \rightarrow \quad \theta_a\Delta_l + a_2\Delta l^2 = W_2 \quad \therefore \quad a_2 = \frac{W_2 - \theta_a\Delta l}{\Delta l^2}. \tag{B.6}$$

Finally, after defining the parameters, the curvature expression for node 1 Eq. (5.83) is obtained

$$W_1'' = W''(0) = 2a_2 \quad \therefore \quad W_1'' = \frac{2\,(W_2 - \theta_a\Delta l)}{\Delta l^2}. \tag{B.7}$$

b) Case B: Intermediate Nodes
Based on Figure B.1b, three expressions for the deflection at different positions are defined

$$W(-\Delta l) = W_{i-i} = a_0 - a_1\Delta l + a_2\Delta l^2 \tag{B.8}$$

$$W(0) = a_0 = W_i \tag{B.9}$$

$$W(\Delta l) = W_{i-i} = a_0 + a_1\Delta l + a_2\Delta l^2 \tag{B.10}$$

Substituting (B.9) into Eqs. (B.8) and (B.10), we obtain the system:

$$\begin{cases} W_i - a_1\Delta l + a_2\Delta l^2 = W(-\Delta l) \\ W_i + a_1\Delta l + a_2\Delta l^2 = W(\Delta l) \end{cases} \tag{B.11}$$

Solving for a_2, we obtain

$$a_2 = \frac{W_{i-1} - 2W_i + W_{i+1}}{2\Delta l^2}. \tag{B.12}$$

Finally, after defining a_2, the curvature expression for an intermediate node i Eq. (5.84) is derived

$$W_i'' = W''(0) = 2a_2 \quad \therefore \quad W_i'' = \frac{W_{i-1} - 2W_i + W_{i+1}}{\Delta l^2} \tag{B.13}$$

c) Case C: Support on the Right
As illustrated in Figure B.1c, the deflection at the support is zero, thus

$$W(0) = 0 \quad \therefore \quad a_0 = 0. \tag{B.14}$$

The rotation at the support is equal to θ_b

$$W'(0) = \theta_b \quad \therefore \quad a_1 = \theta_b. \tag{B.15}$$

The deflection at node $n-1$ ($x = -\Delta l$) is defined as W_{n-1}, which allows solving for a_2

$$W(-\Delta l) = W_{n-1} \quad \rightarrow \quad -\theta_b \Delta_l + a_2 \Delta l^2 = W_{n-1} \quad \therefore \quad a_2 = \frac{W_{n-1} + \theta_b \Delta l}{\Delta l^2}. \tag{B.16}$$

Finally, after defining the parameters, the curvature expression for node n Eq. (5.85) is obtained

$$W_n'' = W''(0) = 2a_2 \quad \therefore \quad W_n'' = \frac{2\left(W_{n-1} + \theta_b \Delta l\right)}{\Delta l^2}; \tag{B.17}$$

B.2 TAYLOR SERIES EXPANSION

The curvature equations can also be derived using Taylor series approximations, following the methodology presented in Holanda and Silva (2021).

A function can be expanded into a Taylor series to approximate its behavior around a given point using its derivatives. The Taylor series expansion expresses a function as an infinite sum of polynomial terms, where each term is derived from the function's derivatives evaluated at a specific reference point.

Mathematically, if a function $f(x)$ is sufficiently smooth and differentiable at $x = a$, it can be written as

$$f(x) = f(a) + f'(a)(x-a) + \frac{f''(a)(x-a)^2}{2!} + \cdots + \frac{f^{(n-1)}(a)(x-a)^{n-1}}{(n-1)!} + R_n. \tag{B.18}$$

From this equation, the function can be expressed at incremental positions as follows

$$f(x+\Delta x) = f(x) + f'(x)\Delta x + f''(x)\frac{\Delta x^2}{2} + \ldots; \tag{B.19}$$

$$f(x-\Delta x) = f(x) - f'(x)\Delta x + f''(x)\frac{\Delta x^2}{2} - \ldots. \tag{B.20}$$

Based on Eqs. (B.19) and (B.20), the expressions for the deflections at the previous and subsequent cross-sections can be written as

$$W(x+\Delta x) = W(x) + W'(x)\Delta x + W''(x)\frac{\Delta x^2}{2}; \tag{B.21}$$

$$W(x-\Delta x) = W(x) - W'(x)\Delta x + W''(x)\frac{\Delta x^2}{2}. \tag{B.22}$$

Using these equations, the boundary conditions are evaluated for each case:

a) Case A: Support on the Left
Setting $x = 0$ with boundary conditions $W(0) = 0$, $W'(0) = \theta_a$, and $W(\Delta x) = W_2$ in Eq. (B.21), we obtain

$$W_2 = \theta_a \Delta x + W''(0)\frac{\Delta x^2}{2}. \tag{B.23}$$

Defining $W''(0) = W_1''$ and rearranging the terms, the expression for curvature at node 1 Eq. (5.83) is obtained

$$W_1'' = \frac{2\,(W_2 - \theta_a \Delta l)}{\Delta l^2}. \tag{5.83}$$

b) Case B: Intermediate Nodes
Setting $x = 0$ with boundary conditions $W(0) = W_i$, and $W(\Delta x) = W_{i+1}$ in Eq. (B.21), we obtain

$$W_{i+1} = W_i + W'(0)\Delta x + W''(0)\frac{\Delta x^2}{2}. \tag{B.24}$$

Similarly, setting $x = 0$ with boundary conditions $W(0) = W_i$, and $W(-\Delta x) = W_{i-1}$ in Eq. (B.22), we obtain

$$W_{i-1} = W_i - W'(0)\Delta x + W''(0)\frac{\Delta x^2}{2}. \tag{B.25}$$

Solving the system formed by Eqs. (B.24) and (B.25), and defining $W''(0) = W_i''$, we obtain the curvature expression for an intermediate node i

$$W_i'' = \frac{W_{i-1} - 2W_i + W_{i+1}}{\Delta l^2}. \tag{5.84}$$

c) Case C: Support on the Right
Setting $x = 0$, with boundary conditions $W(0) = 0$, $W'(0) = \theta_b$, and $W(-\Delta x) = W_{n-1}$ in Eq. (B.22), we obtain

$$W_{n-1} = -\theta_b \Delta x + W''(0)\frac{\Delta x^2}{2}. \tag{B.26}$$

Defining $W''(0) = W_n''$ and rearranging the terms, the expression for curvature at node n (5.85) is obtained

$$W_n'' = \frac{2\left(W_{n-1} + \theta_b \Delta l\right)}{\Delta l^2}. \tag{5.85}$$